SEDIMENTATION AND DIFFUSION IN AN EXPERIMENTAL HARD-SPHERE-PLUS-DIPOLAR COLLOIDAL SYSTEM

HUGH NEWMAN

Sedimentation and Diffusion in an Experimental Hard-Sphere-plus-Dipolar Colloidal System

by

© Hugh Newman III, B.Sc.

A thesis submitted to the

Department of Physics and Physical Oceanography

in partial fulfilment of the

requirements for the degree of

Master of Science

Department of Physics and Physical Oceanography

Memorial University of Newfoundland

August 2013

St. John's Newfoundland

Abstract

Laser scanning confocal microscopy was used to image a thin sediment of a Brownian colloidal suspension of PMMA spheres in a decalin/TCE solvent. The sediment is imaged in its entirety in 3-dimensions, as well as with 2-dimensional time-series captured incrementally throughout the sediment. The structure and dynamics are analysed and compared to a hard-sphere system. AC electric fields are applied parallel to gravity to attempt to induce a dipolar interaction in the colloidal spheres. If the system is confirmed to be hard-sphere like, then this allows comparison of the system with applied fields to a hard-sphere-plus-dipolar system.

Acknowledgements

I would first and foremost like to thank my supervisor Anand Yethiraj for his patience and guidance throughout this project, and my entire time working with him on his research team. He has been key in getting me on track and helping me meet my goals. I'd like to thank my wife Alanna Wicks for her support. During hard times she has been a shoulder to lean on, as well as an encouraging voice to help me get back in the saddle. I'd like to thank my family for their emotional support throughout my education. I'd like to thank some of my other professors, notably Todd Andrews, Len Zedel, John Whitehead, and Ivan Saika-Voivod for their various acts of kindness, support, and wisdom throughout my program. I'd also like to thank Dr. Eli Sloutskin from Bar-Ilan University for a sneak peek at his research before publication, as well as the suggestion to use a decalin and tetrachloroethylene mixture with PMMA for a hard sphere system. And lastly I would like to thank my many friends and lab mates in the department of Physics and Physical Oceanography at Memorial.

Contents

Abstract ii

Acknowledgements iii

List of Tables vii

List of Figures viii

1 Introduction 1

1.1 Colloids 1

1.2 Motivation for Study 4

2 Background and Theory 8

2.1 Colloidal Interactions 8

2.1.1 The Hard Sphere Interaction 8

2.1.2 Brownian Motion and Diffusion 10

2.1.3 Electrostatic Interactions 11

2.2 Colloidal Structure 13

2.2.1 Colloids as Hard Spheres 13

2.2.2 Dipolar Interactions 15
2.3 Laser Scanning Confocal Microscopy 17
2.3.1 General Principles of Fluorescence Theory 18
2.3.2 Principles of Confocal Microscopy 20

3 Experimental Procedure **23**

3.1 Sample Preparation 23
3.1.1 Particle Synthesis 23
3.1.2 Index Matching of Particles and Solvent 24
3.1.3 Tuning the Extent of the Sedimentation Profile 25
3.1.4 Dielectric properties of the experimental system 26
3.2 Electric Field Cell Construction 27
3.2.1 Electric Field Apparatus 27
3.2.2 Constructing the Linear Z-Field Cell 27
3.3 Imaging using the Confocal Microscope 29
3.3.1 Imaging the Colloidal Sediment 33
3.3.2 Imaging 2D Diffusion 34
3.4 Image Processing using IDL 34
3.4.1 Extracting Particle Locations in the Colloidal Sediment 35
3.4.2 Extracting a Sedimentation Profile and Equation of State . . . 38
3.4.3 Calculating the Diffusion Coefficient 39

4 Results and Discussion **42**

4.1 Sedimentation profiles of hard-sphere colloids in an external field . . . 42
4.1.1 $1\mu m$ PMMA in 60:40 decalin/TCE mixture 43

4.1.2 $0.8\mu m$ PMMA in 70:30 decalin/TCE mixture 50
4.1.3 Comparison of the zero-field profiles for both monodisperse experiments 54
4.2 Diffusion of Colloidal Clusters 55
4.2.1 Zero-field diffusion in a density matched dilute system 57
4.2.2 Diffusion in a thin sediment for $1\mu m$ diameter PMMA in 60:40 decalin/TCE 59
4.2.3 Diffusion in a thin sediment for $0.8\mu m$ diameter PMMA in 70:30 decalin/TCE 72
4.2.4 Comparison of the diffusion coefficients and cluster analysis for both monodisperse experiments 83
4.3 Sedimentation equilibrium and dynamics in a bidisperse colloidal suspension 88

5 Conclusions **102**

5.1 Summary of Results 102

Bibliography **105**

List of Tables

4.1 Density, index of refraction, and dielectric constants for the PMMA particles and three solvent mixtures composed of 50:50, 60:40, and 70:30 (by volume) ratios of decalin and TCE. In addition, the calculated gravitational lengths used in the corresponding experiments are listed. 43

4.2 Lambda parameter for each experiment calculated from the corresponding electric field strength. In order to calculate Λ, we use dielectric constants from Table 4.1, and equation 2.13. 89

List of Figures

2.1 An example of a Jablonski diagram showing the principle of fluorescence 19

2.2 A basic diagram of a confocal microscope 21

3.1 Equipment used for electric field generation and amplification 28

3.2 Electric field cell for linear fields parallel to gravity 30

3.3 Laser Scanning Confocal Microscope apparatus 31

3.4 Before and after a spatial bandpass filter 36

3.5 Radius of Gyration vs. Brightness Plots 37

3.6 MSD as a function of time for $1\mu m$ PMMA colloids in 60:40 decalin/TCE 40

4.1 Sedimentation Profiles for a range of sinusoidal peak-to-peak field strengths from $E = 0V/mm$ to $E = 1207.7V/mm$ obtained from counting particles using feature finding program for $1\mu m$ diameter PMMA colloids in 60:40 decalin/TCE 44

4.2 Zoomed in sedimentation profiles for a range of field strengths from $E = 0V/mm$ to $E = 1207.7V/mm$ obtained from counting particles using feature finding program for $1\mu m$ diameter PMMA colloids in 60:40 decalin/TCE 44

4.3 Zero-field sedimentation profiles obtained from particle counting and summed intensity for $1\mu m$ diameter PMMA colloids in 60:40 decalin/TCE compared 45

4.4 Intensity sedimentation profiles for a range of field strengths from $E = 0V/mm$ to $E = 1207.7V/mm$ for $1\mu m$ diameter PMMA colloids in 60:40 decalin/TCE 46

4.5 Intensity sedimentation profiles for $1\mu m$ diameter PMMA colloids in 60:40 decalin/TCE at select field strengths 46

4.6 XZ transposed images of the sediment of $1\mu m$ PMMA colloidal sediments in 60:40 decalin/TCE at selected field strengths. 47

4.7 Equations of state for a range of field strengths from $E = 0V/mm$ to $E = 1207.7V/mm$ for $1\mu m$ diameter PMMA colloids in 60:40 decalin/TCE, calculated from the intensity sedimentation profiles 48

4.8 Selected field strengths with the regions A, B, and C highlighted at their corresponding ϕ values. Equations of state for $1\mu m$ diameter PMMA colloids in 60:40 decalin/TCE, calculated from the intensity sedimentation profiles 49

4.9 Intensity sedimentation profiles for a range of field strengths from $E = 0V/mm$ to $E = 1666.7V/mm$ for $0.8\mu m$ diameter PMMA colloids in 70:30 decalin/TCE 51

4.10 Intensity sedimentation profiles for $0.8\mu m$ diameter PMMA colloids in 70:30 decalin/TCE at select field strengths 51

4.11 XZ transposed images of the sediment of $0.8\mu m$ PMMA colloidal sediments in 70:30 decalin/TCE at selected field strengths. 52

4.12 Equations of state for $0.8\mu m$ particles, calculated from the intensity sedimentation profile 53
4.13 Equations of state for $0.8\mu m$ particles, calculated from the intensity sedimentation profile at select field strengths 54
4.14 Zero-field dimensionless sedimentation profiles (ϕ vs. z/l_g) for $2a = 1\mu m$ PMMA colloids in 60:40 decalin/TCE and $2a = 0.8$ PMMA colloids in 70:30 decalin/TCE. 55
4.15 MSD as a function of time for $1\mu m$ diameter PMMA colloids in 60:40 decalin/TCE with linear fits 56
4.16 MSD as a function of time for $1\mu m$ diameter PMMA colloids in 60:40 decalin/TCE with error shown for duration of experiment 56
4.17 Diffusion coefficient as a function of height of $2a = 1\mu m$ diameter PMMA colloids in a density matched suspension of 50:50 decalin/TCE with $\Phi = 1\%$. 58
4.18 Diffusion as a function of z for a range of field strengths from $E = 0V/mm$ to $E = 1203.7V/mm$ of $2a = 1\mu m$ PMMA colloids in 60:40 decalin/TCE. 60
4.19 Diffusion coefficient as a function of volume fraction, ϕ, for a range of field strengths from $E = 0V/mm$ to $E = 1203.7V/mm$ of $2a = 1\mu m$ PMMA colloids in 60:40 decalin/TCE. 61
4.20 Diffusion as a function of z for $1\mu m$ diameter PMMA colloids in 60:40 decalin/TCE at select field strengths 63
4.21 Diffusion as a function of electric field strength for regions A, B, and C for $2a = 1\mu m$ PMMA colloids in 60:40 decalin/TCE 64

4.22 Images of $2a = 1\mu m$ PMMA colloids in 60:40 decalin/TCE at region A ($z = 7\mu m$) into the sample for four specific z-field strengths. 65

4.23 Normalized cluster analysis of $2a = 1\mu m$ PMMA colloids in 60:40 decalin/TCE at region A ($z = 7\mu m$). 66

4.24 Images of $2a = 1\mu m$ PMMA colloids in 60:40 decalin/TCE at region B ($z = 20\mu m$) into the sample for four specific z-field strengths. . . . 68

4.25 Normalized cluster analysis of $2a = 1\mu m$ PMMA colloids in 60:40 decalin/TCE at region A ($z = 7\mu m$). 69

4.26 Images of $2a = 1\mu m$ PMMA colloids in 60:40 decalin/TCE at region C ($z = 55\mu m$) into the sample for four specific z-field strengths. . . . 70

4.27 Normalized cluster analysis of $2a = 1\mu m$ PMMA colloids in 60:40 decalin/TCE at $z = 40\mu m$ ($15\mu m$ below region C). 71

4.28 Diffusion as a function of z for a range of field strengths from $E = 0V/mm$ to $E = 1666.7V/mm$ of $0.8\mu m$ diameter PMMA colloids in 70:30 decalin/TCE. 73

4.29 Diffusion coefficient as a function of z for seven specific field strengths $0.8\mu m$ diameter PMMA colloids in 70:30 decalin/TCE 73

4.30 Diffusion as a function of of field strength for regions A, B, and C for $0.8\mu m$ diameter PMMA colloids in 70:30 decalin/TCE 74

4.31 Images of $0.8\mu m$ diameter PMMA colloids in 70:30 decalin/TCE at $z = 7\mu m$ into the sample for seven specific z-field strengths. 76

4.32 Normalized cluster analysis of $0.8\mu m$ diameter PMMA colloids in 70:30 decalin/TCE at $z = 7\mu m$ 77

4.33 Images of $0.8\mu m$ diameter PMMA colloids in 70:30 decalin/TCE at $z = 35\mu m$ into the sample for seven specific z-field strengths. 78

4.34 Normalized cluster analysis of $0.8\mu m$ diameter PMMA colloids in 70:30 decalin/TCE at $z = 30\mu m$ 79

4.35 Normalized cluster analysis of $0.8\mu m$ diameter PMMA colloids in 70:30 decalin/TCE at $z = 40\mu m$ 79

4.36 Images of $0.8\mu m$ diameter PMMA colloids in 70:30 decalin/TCE at $z = 63\mu m$ into the sample for seven specific z-field strengths. 81

4.37 Images of $0.8\mu m$ diameter PMMA colloids in 70:30 decalin/TCE at $z = 79\mu m$ into the sample for seven specific z-field strengths. 82

4.38 A scaled diffusion coefficients for both monodisperse experiments ($2a = 1\mu m$ PMMA in 60:40 decalin/TCE and $2a = 0.8\mu m$ PMMA in 70:30 decalin/TCE) plotted against the dimensionless z/l_g at similar Λ values 83

4.39 Diffusion coefficients as a function of local volume fraction, ϕ, for both monodisperse experiments ($2a = 1\mu m$ PMMA in 60:40 decalin/TCE and $2a = 0.8\mu m$ PMMA in 70:30 decalin/TCE) for zero-field 84

4.40 Cluster analysis at three positions in the sediment for $2a = 1\mu m$ PMMA colloids in 60:40 decalin/TCE and $2a = 0.8\mu m$ PMMA colloids in 70:30 decalin/TCE at similar dipolar strengths, Λ 87

4.41 Bidisperse suspension. Intensity sedimentation profiles for a range of field strengths from $E = 240V/mm$ to $E = 1440V/mm$ for $0.8\mu m$ PMMA colloids in 70:30 decalin/TCE 90

4.42 Bidisperse suspension. Intensity sedimentation profiles for four selected field strengths for $0.8\mu m$ diameter PMMA colloids in 70:30 decalin/TCE 90

4.43 Apparent equations of state for a range of field strengths from $E = 0V/mm$ to $E = 1207.7V/mm$ for $1\mu m$ diameter PMMA colloids in 60:40 decalin/TCE, calculated from the intensity sedimentation profiles 92

4.44 XZ transposed images of the sediment of $0.8\mu m$ PMMA colloidal sediments in 70:30 decalin/TCE at selected field strengths for a bidisperse system. 93

4.45 Bidisperse suspension. Diffusion coefficient as a function of z for a range of field strengths from $E = 240V/mm$ to $E = 1440V/mm$ of $0.8\mu m$ diameter PMMA colloids in 70:30 decalin/TCE. 94

4.46 Bidisperse suspension. Diffusion coefficient as a function of z for four field strengths of $0.8\mu m$ diameter PMMA colloids in 70:30 decalin/TCE. 95

4.47 Diffusion as a function of electric field strength for selected regions . . 96

4.48 Image of 0.8μm PMMA in a binary suspension at $4\mu_m$, $18\mu m$, and $40\mu m$ into the sample for four specific z-field strengths. 97

4.49 Cluster analysis of $0.8\mu m$ particles at $7\mu m$, $20\mu m$, and $40\mu m$ (near regions A, B, and C)into the sample for a bidisperse system 99

Chapter 1

Introduction

1.1 Colloids

Colloids are quite common in nature as well as items we use in everyday life. Milk, fog, and dust as well as cement, paint, and aerosols are all examples of colloidal systems. The attributes these all share is that they are made up of small particles, suspended within a continuous medium; water in air for fog, proteins in water for milk, etc. However, particles in a medium is not the only defining factor for a colloidal system. The International Union of Pure and Applied Chemistry defines a colloid as having a lower size limit of 1nm and an upper size limit of 1μm. The lower limit ensures that they are large enough to be distinguishable from a pure solution, while the large limit ensures they undergo Brownian motion in a fluid while not being too large so that they sediment quickly under in the presence of gravity.

More precise characterizations of the colloidal regime can be obtained by cal-

culating the gravitational length and the Peclet number. The Peclet number is a dimensionless parameter relating the Brownian motion of the particles to the shear rate of the solution, γ. This is done by defining a characteristic diffusion time,

$$\tau_D = \frac{a^2}{D} = \frac{6\pi\eta_\circ a^3}{k_B T}. \tag{1.1}$$

and a characteristic time relating to the shear rate,

$$\tau_{shear} = \gamma^{-1}, \tag{1.2}$$

where $\eta_\circ$ is the viscosity of the solution, a is the particles radius, k_B is the Boltzmann constant, and T is absolute temperature. The Peclet number, Pe, is then given by,

$$Pe = \frac{\tau_D}{\tau_{shear}} = \frac{6\pi\eta_\circ a^3\gamma}{k_B T}. \tag{1.3}$$

For Peclet numbers less than unity, Brownian motion is able to re-disperse the particles during shearing, while for Peclet numbers larger than unity, the shear-induced structure is unaffected by Brownian motion [1].

The gravitational length is also used to determine if a dispersion is in the colloidal regime. The gravitational length is defined,

$$l_g = \frac{k_B T}{\frac{4}{3}\pi a^3 \Delta\rho g}. \tag{1.4}$$

where $\Delta\rho$ is the difference in the density between the solute and the solvent. As the ratio of l_g to the diameter approaches unity from below, the onset of non-Brownian behaviour begins [2,3]. Both of these parameters help us define the difference between a colloidal suspension and a granular system.

These systems have been of interest to people well before they were understood. Early paintings and papyrus (the first paper) are both examples of the early importance of colloids to technological advancement [4]. It was not until 1861 when Thomas Graham conducted experiments, that the difference between colloids and aqueous solutions was established. His experimental observations yielded two different diffusion coefficient regimes. Slower diffusion coefficient with solutions containing gelatin or starch (colloids), and a faster diffusion coefficient with solutions containing salts or sugars. He named these two categories of material colloids (from the Greek word for glue) and crystalloids respectively [4, 5]

Colloidal systems have been studied through the years by many scientists. From the botanist Robert Brown in 1827, for whom the random motion of particles in a liquid is named (Brownian Motion), to Albert Einstein, who along with others worked to quantify this diffusion ultimately arriving at the Stokes-Einstein theoretical relation for diffusion coefficients in 1905. The underlying concept of the Stokes-Einstein relation is that particles in the Brownian regime undergo a random walk due to thermal collisions of the surrounding molecules with the particle. With the development of the laser and other technologies such as confocal microscopy, we have actually been able to study the dynamics and structure of these types of system on the particle scale [5]. We are thus able to acquire quantifiable data about the system by imaging the individual particles. Therefore, although the study of colloidal systems is a very old one, with the aid of these new technologies there are many more things to discover.

1.2 Motivation for Study

Fundamental to the study of the physics of fluids is the equation of state (EOS). The simplest EOS is one of an ideal gas, composed of a non-interacting point particles. The equation of state for this system is defined as.

$$PV = Nk_BT \tag{1.5}$$

and is known as the ideal gas law, where P is absolute pressure, V is the volume, N is the number of particles, k_B is the Boltzmann constant, and T is absolute temperature. In a system of interacting particles, we can relate the EOS to the underlying interactions. A system commonly used in physics to model molecular and atomic systems, is the hard-sphere potential. In this case the particles have a finite radius and an infinite step-function potential at their surface and no other interactions. Stated simply, the particle volumes cannot over lap. In this case we can obtain an equation of state for this system as a function of the *osmotic pressure* Π, and the *volume fraction* ϕ. This hard-sphere equation of state is well described by the phenomenological Carnahan-Starling relation [6]:

$$\Pi(\phi) = nk_BT\frac{1+\phi+\phi^2-\phi^3}{(1-\phi)^3}, \tag{1.6}$$

where Π is the osmotic pressure, n is the number density ($\frac{N}{V}$), and ϕ is the local volume fraction. It has been shown experimentally that charge-screened colloidal suspensions (discussed in section 2.1) show excellent agreement with the Carnahan-Starling relation in the bulk [3, 7]. Charge-screened colloidal suspensions can be viewed as approximate hard-spheres systems. Such colloidal suspensions can be used to study hard-sphere phase behaviour. This is an important discovery due to the

phase transitions that can be observed in colloidal suspensions that are the same (or very similar) to an ideal hard-sphere system, which is used as a model for atomic and molecular systems. Colloidal particles are large enough to view this phase behaviour and study the structure and dynamics of colloidal particles on the particle scale simultaneously.

Examining the local structure and dynamics of colloids, however does have pitfalls. A typical 100x confocal oil immersion microscope objective has a working distance of 170μm. This is of order 100a for a micron scale colloidal particle. In these cases particles are more confined than in a bulk suspension, as rigid walls cannot be assumed to be at an infinite distance away. Deviations in the dynamics of colloidal particles have been observed [8]. The need to obtain the equation of state for these confined cases is also a matter of importance, to determine if they remain approximations of hard-sphere fluids in a confined geometry where interactions with rigid boundaries may alter the systems behaviour. In addition to the EOS, we can also study the real time dynamics of the particles. The diffusion coefficient of a Brownian sphere (radius a) in a solvent (viscosity η) is given by the Stokes-Einstein relation,

$$D_0 = \frac{k_B T}{6\pi\eta a}, \tag{1.7}$$

in dilute regions (far from the substrates) [5].

An attractive feature of colloidal systems is their "tunability". The density of the fluid medium can be matched to that of the particle to make the effective gravitational force felt by the particle negligible. Also, salt can be added to the particles to

shorten the Debye-Hückel screening length (discussed more in Section 2.1) and thus screen the particles from possible inter-particle electrostatic repulsions. However, the above methods of controlling sample properties are static: they cannot be switched on and off. A versatile tuning technique is to apply a high frequency AC electric field to colloidal suspension. Because the particles and suspension medium often have a dielectric mismatch, the particles feel an induced field response. This can be approximated to be a dipole-dipole interaction between particles, on top of their hard sphere interaction. Not only can this effect be switched on and off during an experiment, but the strength of interactions can be changed in real time.

The first motivation for this work is to test hard-sphere-like colloidal systems in a confined geometry by testing their agreement to the Carnahan-Starling relation. This will be done by measuring the concentration as a function of height in a particle sediment, and directly extracting the equation of state. As a second test of hard-sphere agreement, the diffusion as a function of height in the sample will be measured and compared with the Stokes-Einstein value in the dilute regions.

Secondly, colloids in AC electric fields behave convincingly like hard-spheres with an additional induced dipole-dipole interaction [9–11]. However there have been interesting exceptions observed [12, 13]. In this work linear electric fields will be applied to the suspensions to induce different colloidal structures, which are micron-scale analogs of thermodynamic phases [14]. For these cases, equations of state and diffusion coefficients will also be extracted to classify the true interactions in these systems and

see if they can be compared to hard-sphere plus dipole-dipole interactions.

Third, the effect of bidispersity on these experiments will be tested by looking at two differently sized particles in the same system. Certain particle size ratios, and particle concentration ratios can be tweaked to allow for bidisperse crystal formation, for the polydispersity to prevent crystal formation, or for unique chain structures. In linear fields monodisperse colloidal systems in an electric field create chain-like structures along the direction of the field [12, 15]. The effect of bidispersity, or a controlled polydispersity may alter this behaviour.

Chapter 2

Background and Theory

2.1 Colloidal Interactions

In order to have a complete understanding of a system of colloidal particles, we first need to understand the basic interparticle interactions that the spheres feel in the suspension. Considered in this work, and discussed in this chapter are the hard sphere interaction, Brownian motion, electrostatic interactions, gravitational and induced dipolar interactions.

2.1.1 The Hard Sphere Interaction

The simplest system in physics is a system of point particles. In this case the objects take up no actual volume in space, and can overlap and therefore exist in the same physical space at the same time. This system only exhibits one phase: that of an "ideal gas". Moving up in complexity from this is a system of hard spheres. Each "hard sphere" occupies a fixed volume in space. Particles do not interact with each other

apart from this "excluded volume interaction." Two hard spheres do not interact with each other when their surfaces are not touching, and there is effectively an infinite repulsive interaction potential upon contact that prevents them from overlapping. Hard-sphere systems have been studied quantitatively to model dense fluids [16]. It is the simplest system in which a fluid-solid phase transition is known to occur.

Upon packing in a fixed volume, there is an "excluded volume" to which the spheres do not have access. It was originally postulated by 17th-century scientist Johannes Kepler that the maximum packing of spheres was in an FCC crystal, which has a maximum packing fraction of 74%. As simple of an idea as this seems, a rigorous proof was only proposed in the past decade by Thomas Hales [17]. In practice, spheres are often packed randomly as closely as possible, called random close packing, and in this instance the maximum volume fraction (referred to interchangeably as VF or ϕ in this thesis) to be achieved can be shown to be around 63% [1]. The fact that the random close packed system can be rearranged to a FCC and be more closely packed begs the question, can a crystal form at lower packing? Computer simulations done by Hoover and Ree in 1968 show a first-order freezing transition at a volume fraction as low as 49.4%, and a first-order melting transition as high as 54.5%. This region is known as a coexistence region [16, 18].

The hard-sphere model is represented analytically with high accuracy by a model put forth by Carnahan and Starling in 1969 [6]. The osmotic pressure of the hard

spheres, Π, is written as

$$\Pi = nk_BT\frac{(1+\phi+\phi^2-\phi^3)}{(1-\phi)^3}. \tag{2.1}$$

where

$$\phi = (4/3)\pi r^3 n \tag{2.2}$$

is the volume fraction, and $n = N/V$. In this system and equation of state we use the osmotic pressure as opposed to pressure as seen in the ideal gas law, given in equation 1.5. The osmotic pressure is given by the total pressure of the system, comprised of the hydrostatic pressure of the system as well as the pressure of the colloidal particles, minus the hydrostatic pressure. This relation is accepted as the analytic model for a hard sphere equation of state [16].

2.1.2 Brownian Motion and Diffusion

Small particles in a fluid can be observed to undergo a constant random transport, called Brownian motion. This discovery is attributed to the botanist Robert Brown, who, although he was not the first to note the motion, was the first to correctly attribute it to molecular collisions. It was not until the early twentieth century that with work by Einstein and Perrin that this notion became commonly accepted [19,20]. The molecules of the fluid are in constant thermal motion. The random collisions of these moving molecules with a colloidal particle causes the random walk of the particle. The energy transferred to the particle by the thermal motion of the solvent molecules is $\frac{3}{2}k_BT$, split evenly between the three translational degrees of freedom. There is a balancing of this energy transference and the viscous damping of the particles motion by the solvent.

It can be shown by solving the Langevin equation, which balances Brownian motion with viscous damping, that the motion of the Brownian particle is described best by the variance in the displacement, also known as the mean squared displacement (MSD). We may write the MSD as

$$\langle (\mathbf{r}_t - \mathbf{r}_0)^2 \rangle = 2kD_0t, \tag{2.3}$$

where $\mathbf{r}_t$ and $\mathbf{r}_0$ are the particles position in k dimensional space (1, 2, or 3) at time t and at its initial position respectively. D_0 is the Stokes-Einstein diffusions coefficient given by,

$$D_0 = \frac{k_B T}{6\pi\eta a}. \tag{2.4}$$

This links the MSD, a variable calculable from measurable particle displacement, to the diffusion coefficient which is not directly measurable. An an example, if one were studying the diffusion of a sphere only along the $\mathbf{x}$ direction then $k = 1$, however if studying the diffusion of a sphere in a 2-dimensional time-series (as we shall see done in chapters 3 and 4), then $k = 2$ [21].

2.1.3 Electrostatic Interactions

In colloidal systems there is often a long range repulsion between particles, depending on the medium in which they are suspended. If the particles are suspended in a highly polar solvent like water ($\epsilon_r = 80.1$ at 20° Celsius) or even a less polar solvent, an example being cyclohexyl bromide-decalin (CHB-decalin) with dielectric constant $\epsilon_r = 5.6$ (low polar media have $\epsilon_r \approx 2$), some of the chemical groups on the particle surfaces disassociate. This causes the particles to be charged creating a long range $(1/r)$ electrostatic repulsion. In a solvent with ionic impurities, there is dissociation

in the solvent forming co-ions and counter-ions. Counter-ion screening gives rise to an exponential attenuation of this interaction.

In order to reduce the long range repulsion one must reduce the associated Debye-Hückel screening length, κ^{-1} defined by,

$$\kappa^{-1} = \sqrt{\frac{\epsilon_\circ \epsilon_r k_B T}{2e^2 C_\circ N_A}} \tag{2.5}$$

where $C_\circ$ is the solutions ionic strength, N_A is Avogadro's number, $\epsilon_\circ$ is the permittivity of free space, ϵ_r is the relative dielectric constant of the solvent, k_B is Boltzmann's constant, e is elementary charge, and T is absolute temperature [22]. When the Debye-Hückel screening length is small compared to the particle radius, that is $\kappa a \gg 1$, then the electrostatic interaction is effectively screened.

Looking at the definition of the Debye-Hückel screening length in equation 2.5, a clear way to vary it is to try to change the ionic strength of the solvent. In practice this is done by adding ionic compounds like salts to polar solvents. The salts dissociate in the solvent into anions and cations. The positive cations are attracted to the negatively charged surface molecules, or the negative anions surround the positively charged surface ions of the colloidal particles (depending on the solvent), and effectively, "screening" the charge of the particles from one another. The more salt added, the greater the ionic strength of the solvent, which leads to more cations surrounding the particle for a smaller Debye-Hückel screening length. In highly polar solvents like water, simple salts can be used such as potasium chloride (KCl), which dissociate into K^+ and Cl^-. However for moderately polar solvents, like a CHB-decalin mixture,

surface ions can still dissociate causing strong repulsion. Screening in these weakly polar solvents require salts with amphiphilic groups.

For non-polar solvents such as the one used in this research ($\epsilon_r \sim 2$), decalin-tetrachloroethylene (decalin/TCE), long range repulsion isn't observed. The dielectric constant is smaller and as a result the surface ions of the particles dissociate to a lesser extent.

2.2 Colloidal Structure

Hard-sphere colloidal suspensions as described above are used as model particles for statistical mechanical models for fluids and solids. They mimic the strong repulsion demonstrated in atomic and spherical molecular systems [14].

2.2.1 Colloids as Hard Spheres

With the right sample preparation (see section 2.1.3) colloids can be shown to be equivalent to hard-spheres, or at least "hard-sphere like." This is done by comparing the equation of state (EOS) of a colloidal system to that of the Carnahan-Starling relation above in equation 2.1. It is a challenge to extract the EOS from a physical system. Osmotic pressure is not directly measurable, so a related parameter must be found. It was shown by Biben *et al* through simulation that a density snapshot (or density profile as we will refer to it) of a colloidal sediment in a gravitational field can lead us to the EOS [23]. The shape of the density profile is very sensitive to the interactions occurring in the colloidal system, and thus the EOS can be extracted.

Colloids in a gravitational field sediment caused by gravity, but because of their small size not all of them just sink to the bottom. Some of the colloidal particles are pushed upwards by an osmotic pressure differential, $\Pi(z)$. The sediment can be described by

$$\frac{\Pi(z)}{k_B T} = l_g^{-1} \int_z^h n(z) dz, \tag{2.6}$$

where $n(z)$ is the particle number density, which approaches zero at some height h. $n(z)$ is the density profile. The extent of this profile and the time it takes for equilibration are dependent on several factors including the gravitational length, l_g, and the Peclet number, Pe. In practice the particles need to be left to sediment to an equilibrated state. The time required for this is the Stokes time. This time is calculated from Stokes' law as

$$\tau_s = \frac{9\eta d_{cell}}{2a^2 \Delta\rho g}, \tag{2.7}$$

where η is the solvent viscosity, d_{cell} is the distance from the top of the cell to the bottom that the particles have to sediment, a is particle radius, and $\Delta\rho$ is the density difference between solvent and particle. For our system (60:40 decalin/TCE by volume) we get a Stokes time of $\tau_s \approx 64$ minutes.

The colloidal EOS in hard-sphere-like colloids was determined experimentally by Piazza *et al* in 1993 [3]. Using a light scattering experiment on a bulk suspension, defined as a suspension in a large container such that the length scales of the container are much much larger than the scale of the particle, the density profile of the colloids was measured and thus the EOS was extracted. When compared to the Carnahan-Starling relation they showed that the two were similar enough that the colloidal system could be treated as an approximate hard-sphere system. However, it

has yet to be seen if in the confined dimensions of microscopy cells, where the length scales of the container are only on the order of 100x the particle diameter and there are many interactions with the wall, the colloidal EOS can still be approximated by the Carnahan-Starling relation for the EOS of hard-spheres. More recent work has been done showing agreement with Piazza's results in similar scattering experiments by Buzzaccaro *et al* and Rutgers *et al* [7, 24]. The work by Buzzaccaro even goes a step further to show a "sticky" attractive interaction along with the hard-sphere interaction [24]. Previous work by Ning Li *et al* has shown deviation from this agreement in a system of charge screened silica spheres in dimethyl sulfoxide and water in confocal microscopy experiments [25].

2.2.2 Dipolar Interactions

One of the best experimental examples of tuning a colloidal suspension is the use of external electric fields [1]. This can be done after sample preparation during an experiment. AC and DC electric fields, as well as magnetic fields, can be turned on and off allowing active control over colloidal interactions, while volume fraction, particle size and screening lengths are important, they cannot be changed once an experiment is in progress. Specifically in this work we will focus on the effects of high frequency AC electric fields along the direction of gravity.

When using a high frequency (1 MHz) AC field to tune a colloidal suspension it is necessary for the solvent and particles to have a mismatch of dielectric constants, ϵ_r, in order to induce a dipole moment in the particle. The index of refraction n is

defined by

$$n = \sqrt{\epsilon_r \mu_r} \tag{2.8}$$

where μ_r is the relative permeability and $\mu_r \approx 1$ for non magnetic materials. This gives us

$$n \approx \sqrt{\epsilon_r}. \tag{2.9}$$

Dielectric constants vary at different frequencies, so the values for optical frequencies in the gigahertz range and for high frequency AC fields in the megahertz range are quite different. Thus, it is possible to make the particles transparent in the optical frequency range, while having the appreciable particle-solvent mismatch in low frequency dielectric constants that is needed for electric field induced effects. Applying linear AC fields at strengths of $\approx 0.1 - 1kV/mm$ causes the particles to form chain like structures. This is due to an induced dipolar attraction in the colloidal spheres, along the direction of the applied field. The chains can attract each other when they are staggered (translated by half a particle diameter along the field direction with respect to a neighbouring chain) to one another forming clustered chains which may be several particles thick perpendicular to the field. If the chains are stacked (particles not offset from one another in neighbouring chains in the field direction) then the chains will repel. The dipolar interaction energy between the particles with a displacement vector $\mathbf{R} = (R, \theta, \phi)$ is expressed as

$$U_{dip}(R, \theta) = -\frac{4\pi\epsilon_\circ\epsilon_f\beta^2 a^6 E_\circ^2}{R^3}\left[\frac{3\cos^2\theta - 1}{2}\right], \tag{2.10}$$

where $\beta = \frac{\epsilon_p - \epsilon_f}{\epsilon_p + 2\epsilon_f}$, and ϵ_p and ϵ_f are particle and fluid dielectric constants. The angle at which colloidal chains attract or repel each other to form clusters perpendicular to the field can be determined from equation 2.10, as $\theta = 54.7°$ [25]. The dipolar

interaction may also be expressed by the dimensionless dipolar strength parameter Λ, defined as,

$$\Lambda = \frac{\pi \epsilon_0 \epsilon_f \beta^2 a^3 E_0^2}{2 k_B T}. \tag{2.11}$$

Applying a high frequency electric field in this way and creating these chain like structures changes many things about the system, most notably its rheological properties (known as the electrorheological effect) [26]. Electrorheological fluids are modelled as hard-spheres with point dipoles, but previous studies (Ning Li *et al*) found that zero field results did not follow the hard-sphere equation of state [25]. Since this system also gave an unexpected low density phase (Agarwal *et al*) it is important to have a system where the interactions can be known precisely [12]. Hence having a system that shows a field response and is hard-sphere-like in zero field is important.

2.3 Laser Scanning Confocal Microscopy

When doing optical microscopy on thick specimens one will find that as the thickness of the specimen increases the image quality will be degraded due to scattered light introduced from outside of the focal plane. This scattered light reduces the signal-to-noise (S/N) ratio and the contrast, effectively obscuring important image information. Berek explored this in 1927, and determined the three elements effecting image quality were the magnification of the image, the detection system sensitivity, and the spreading of the light beam out of the sample [27]. For the purposes of microscopy one always strives for higher magnifications to study smaller and smaller science. While the detection sensitivity in Berek's time was the human eye and we

now have the charge coupled device and the electron multiplied charge coupled device (CCD and EMCCD) cameras. This leaves only the spreading of the light beam. The restricting of this out of focus light was the primary purpose of the confocal microscope. A second outcome is the increase in lateral and axial resolution (the latter of which remains a struggle to improve). Confocal microscopy coupled with fluorescence has proven to be a powerful tool.

2.3.1 General Principles of Fluorescence Theory

Is is important to take note of the basic principles of fluorescence, before moving onto the optical configuration of the confocal microscope. Fluorescence imaging can provide a high contrast signal that, when matched with confocal microscopy, can enhance the results achieved by the removing of out of focus light [27].

A fluorescent molecule (fluorochrome) is a molecule that will absorb photons of light of a specific narrow range of wavelengths through a process refereed to as excitation, and shortly after partially emit the absorbed energy as photons of longer wavelength range corresponding to a lower energy due to the inverse relationship of wavelength and energy described in Planck's Law

$$E = \frac{h\nu}{\lambda}. \tag{2.12}$$

The time between excitation and emission is known as the fluorescence lifetime, and the difference in wavelength between the absorbed and emitted photons is called the Stoke's shift which is dependent on the fluorochrome used.

The cause of the excitation is the interaction of the oscillating electric field vector and the electrons in the fluorochrome. Electrons in different molecules require different amount of energies to be excited to the higher electron orbital. This is the reason

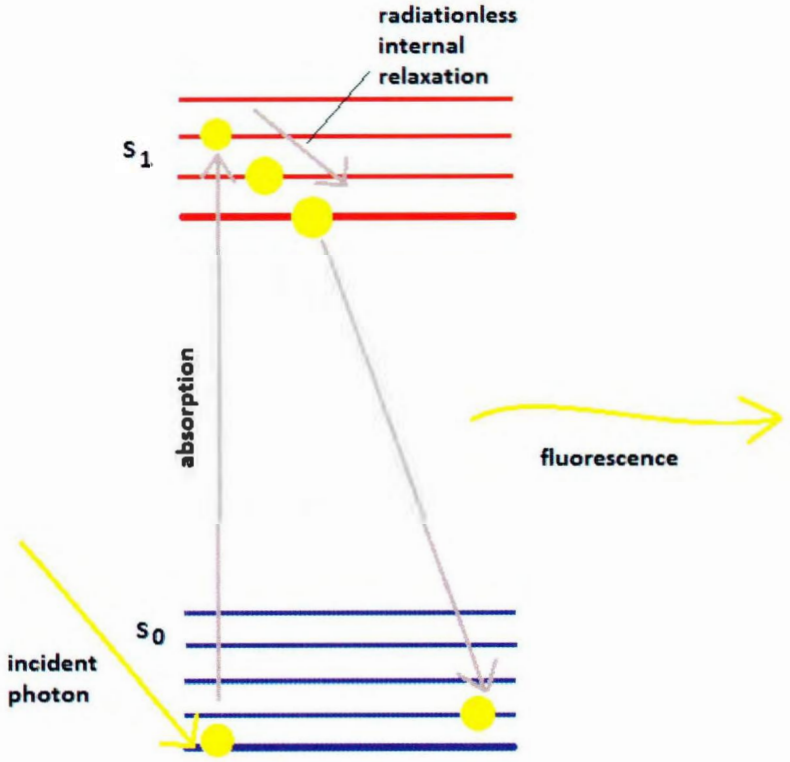

Figure 2.1: An example of a Jablonski diagram showing the principle of fluorescence

that different fluorochromes are excited by and emit different wavelengths with the relationship between the energy and wavelength of light, as explained above. This process is usually described by a Jablonski diagram, named for the Polish physicist who introduced it in 1953 [27]. An example of this diagram can be seen in figure 2.1. Once excited to the higher electron orbital, the electron may decay to a lower vibrational state within this orbital. This causes energy to be lost mostly through heat

absorbed by the solvent, which is the reason the resultant emitted photon is of lower energy and higher wavelength.

2.3.2 Principles of Confocal Microscopy

The confocal microscope requires a few key components: A light source with a pinhole (optional), a beam splitter, an objective, and a detector with a pinhole. There are many ways to construct a confocal microscope including the spinning disk, galvonometer scanning, resonant scanning, or swept field confocal systems, but all are derived from these basic components, assembled as seen in figure 2.2. The light source pinhole causes the light source to only illuminate a single point in the specimen, of which the size is defined by the size of the pinhole and the diffraction limited spot of the objective. The only light that is allowed to pass to the sample, is light that will focus on this point. The detector pinhole is aligned such that only light originating from that point in the specimen and then reflected by the dichroic beam splitter, will be able to pass through to the detector, and form an image. Any stray light from other areas of the sample will be excluded by the pinhole aperture. This is the essence of the confocal microscope: illuminating a size limited spot instead of an entire sample, and then imaging the exact same spot while excluding all other light.

As previously mentioned, confocal microscopy is typically paired with fluorescence. This is done using a series of lasers as the illumination source for the confocal microscope. In this case, the areas of interest of a microscopy sample are labelled with a fluorescent dye and matched with appropriate sets of excitation and emission

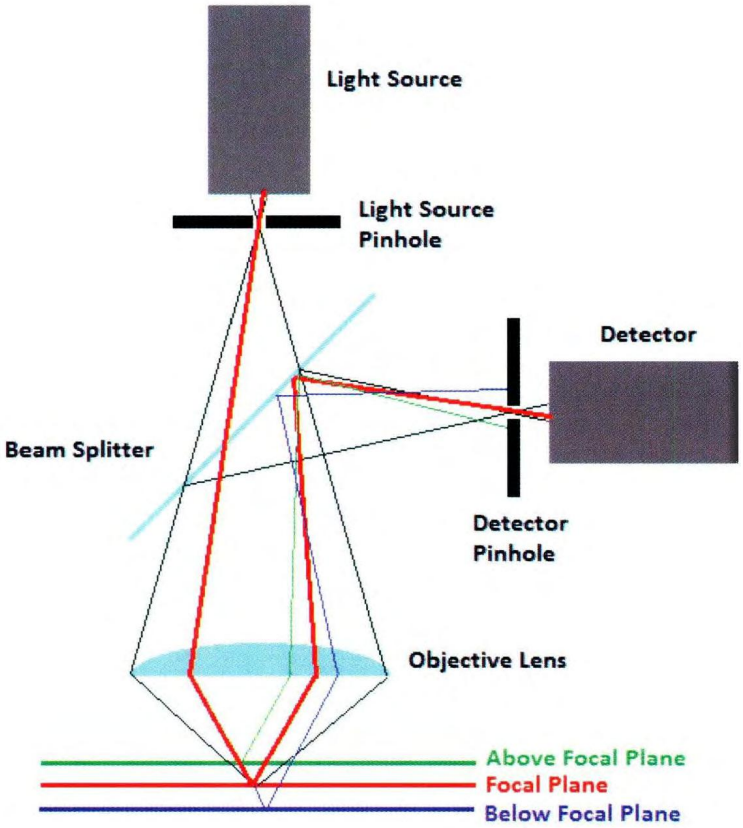

Figure 2.2: A basic diagram of a confocal microscope

filters for illumination and detection. Common examples of dyes used are DAPI (excites with UV and emits in violet), FITC (excites with blue and emits in green), and rhodamine (excites with green and emits red). This eliminates all light except that which is generated by the excitation of the fluorochromes in the region of interest that is labelled, allowing excellent signal-to-noise ratio.

In our samples, the colloidal particles are made transparent by refractive index matching, allowing us to image deep into the sample. At the same time they are fluorescent and hence their fluorescence can be excited in three dimensions in a point by point manner, allowing for both two dimensional time series (xyt stacks) and three dimensional z-stacks (xyz stacks).

Chapter 3

Experimental Procedure

3.1 Sample Preparation

In this work we use poly(methyl methacrylate) (PMMA) spheres in a cis-trans decahydronaphthalene (decalin) and tetrachloroethylene (TCE) mixture to examine the EOS as well as the dynamics. PMMA in TCE and decalin has been reported to be more hard-sphere like than other common colloidal systems. One of the goals is to assess this system as a hard-sphere model system. Owing to the low polarity of the solvents there are very few charge effects, and density matching and index matching are also achieved at the same solvent ratio.

3.1.1 Particle Synthesis

The Poly(methyl methacrylate) particles used were synthesized by Andrew Schofield at the University of Edinburgh. These particles are stabilized using poly(hydroxysteric

acid), referred to as PHSA-stabilized PMMA. We used multiple sizes throughout this work including $\sim 0.6\mu m$, $\sim 0.8\mu m$, $\sim 1.0\mu m$, and $\sim 1.6\mu m$ diameter. The first two fluorescent labelled with DIIC and the latter two labelled with NBD. The synthesis follows a simple and widely used method presented by Antl *et al* [28] while work by Bosma *et al* modified this procedure to incorporate fluorescent dye [29].

3.1.2 Index Matching of Particles and Solvent

To prepare a colloidal suspension for imaging and analysis there are a couple of parameters that need to be tuned by solvent selection. One of the first things to consider is the index of refraction mismatch of the particle and the solvent. A large mismatch will cause multiple scattering in the sample and cause the image quality to decrease the further in the sample imaged. When imaging from below this can cause the higher parts of the sediment to be inaccessible to the confocal microscope. A solvent 50:50 by volume decalin/TCE was used to density match the PMMA particle solution, to study crystal nucleation. In addition, this ratio gives an index of refraction of $n_p \approx 1.49$, which is matched with the estimated index of PMMA. However for our EOS measurement we need a slightly density mismatched system; this will be discussed more in the next section.

3.1.3 Tuning the Extent of the Sedimentation Profile

In order to extract an EOS from a colloidal sediment the extent of the sediment must only be restricted by the bottom surface of the container. The sedimentation profile must go to zero before the top plate of the sample. To do this solvents and their ratios are chosen to mismatch the density of the solvent and the particles. A measure of how sensitive the particles are to sedimentation is the gravitational length, l_g, given by equation 1.4. Gravitational forces can be considered negligible when l_g is much greater than the particle diameter, σ, corresponding to a very small difference in density between the solvent and particle. The PMMA system when index matched is nearly density matched, meaning $\frac{l_g}{\sigma} \gg 1$. In order to get a proper sediment the ratios of the solvents can be tweaked to get a lower gravitational height while sacrificing the quality of the index of refraction match. The decalin/TCE ratio is changed from 50:50 by volume to 60:40. This change causes a slight mismatch in index of refraction of the particle and solvent, but not enough to degrade the image quality from the confocal microscope significantly. It also makes the particles heavier than the solvent, so a sediment can form. The new gravitational length of the decalin/TCE system is $l_g = 12.0\mu m$, which is just over ten times the particle diameter, but is still small enough that gravity is still important. The PMMA in 60:40 decalin/TCE takes several hours to sediment (Stokes time discussed in section 2.2.1), but the extent is short enough to not span the height of the cell, allowing us to obtain the EOS.

3.1.4 Dielectric properties of the experimental system

Looking at the equations for dipolar energy U_{dip} (equation 2.10) and the dipolar strength parameter Λ (equation 2.11) we can see that besides the strength of the electric field E, the main tunable variable is the dielectric constant, ϵ. Materials parameters in these equations are ϵ_f and β, where $\beta = \frac{\epsilon_p - \epsilon_f}{\epsilon_p + 2\epsilon_f}$, and ϵ_f is the dielectric constant of the fluid or solvent, and ϵ_p is the dielectric of the particle material. If $\beta = 0$, then $\Lambda = 0$, which would result in the suspension showing no effect to an applied electric field. The two solvents in the suspensions used in this work, decalin and TCE, have $\epsilon = 2.2$ and $\epsilon = 2.5$ respectively. Because of these low dielectric constants, it is likely that the surface groups on the PMMA spheres do not disassociate and therefore do not become strongly charged. The dielectric constant of the mixture is determined by linear interpolation, by volume, of the values for the pure solvents, e.g. for a 50:50 mixture $\epsilon_f = 2.35$. As an example, if we were to apply a $E = 1000V/mm$ peak-to-peak AC field to this 50:50 suspension with $1\mu m$ diameter PMMA ($\epsilon_p = 2.6$), this would result in $\Lambda = 1.16$. If dipolar forces and k_BT were the only energy scales in the problem, then we would expect to see field-induced structure when $\Lambda > 1$.

Once solvent ratios are chosen based on index matching, dielectric constant mismatch, and density mismatch, the suspension is ready for study. The sample is shaken up and ultrasonicated for 5-10 minutes, then it can be filled into a waiting microscope cell.

3.2 Electric Field Cell Construction

The electric field cell construction is a crucial step in this experiment, and new methods were developed for cell construction. Microscope sample cells needed to be constructed with the ability to apply linear AC field parallel to gravity.

3.2.1 Electric Field Apparatus

The fields are applied to the sample using several pieces of equipment. A Tektronix AFG 3022 dual channel arbitrary function generator is used to generate the AC waveforms. These waveforms are output to a Tektronix TDS 1002 two channel digital storage oscilloscope as well as a Krohn-Hite Model 7602M wide band amplifier. The apparatus is shown in figure 3.1. The outputs of the amplifier are then hooked up to the electrodes in the electric field cell. The ground and live wire from the amplifier are connected to two separated electrodes. The difference in potential causes an electric field between the plates.

3.2.2 Constructing the Linear Z-Field Cell

The simplest cell to build and use is the cell for our linear z field experiment, parallel to gravity. For all the cells the top and bottom plates are made of glass microscope cover slips ($\sim 145\mu m$ thick, and $22mm$ long and wide), coated on one side with indium tin oxide (ITO). ITO is a conductor that is almost transparent to white light (it gives the glass a slightly purple tint) so these slides allow us to apply the electric

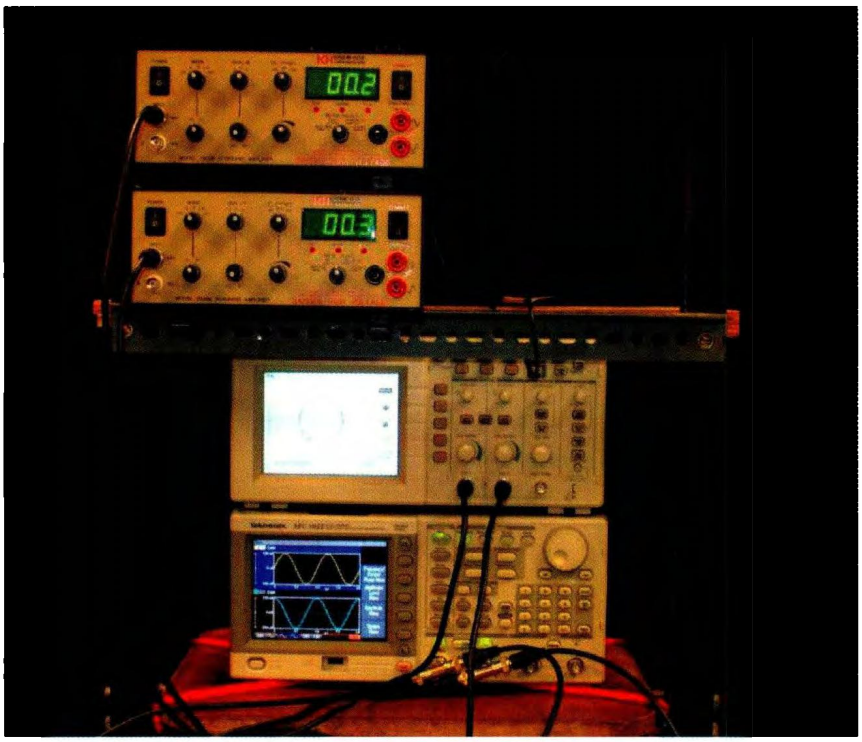

Figure 3.1: Equipment used for electric field generation and amplification. Shown here are two Krohn-Hite Model 7602M amplifiers, a Tektronix AFG 3022 dual channel arbitrary function generator. and a Tektronic TDS 1002 two channel digital storage oscilloscope. The apparatus is setup for a rotating AC field in this configuration, not discussed in this work.

fields without obstructing imaging. The bottom plate, ITO facing up, is glued using Norland optical glue, which cures under UV light, to a full size microscope slide. The goal is to create a thin channel to fill with our colloidal suspension. We use two sets of two $0.050mm$ or $50\mu m$ polyethylene terephthalate film as spacers stacked on one another to give $\sim 100\mu m$ spacing. These spacers are cut to $\sim 3mm$ wide and over $22mm$ long. They are placed on the middle of the bottom plate, with a space of several millimeters between them. This will be our channel. The top plate is then placed on top of this with the ITO side facing down. The top plate and bottom plate are offset so that an electrical connection can be made independently to each electrode. The area between the top and bottom plates is then filled with Norland optical glue, excluding the channel area. Small, flat alligator clips are used to hold the top plate to the bottom plate on the the area with the spaces. This serves the purpose of holding the alignment while the glue is drying as well as preventing the glue from expanding the thickness of the sample too much. The cell can now be filled with colloidal suspension via capillary action and the ends of the channel sealed with more Norland optical glue. The completed cell for the linear z experiments is shown in figure 3.2. Electrical contact is then made using small flat alligator clips to the exposed areas of ITO on the top and bottom plates. This eliminates the need for permanently attaching wires to a microscope cell via conducting glues.

3.3 Imaging using the Confocal Microscope

The imaging equipment used for this work is a Nikon Eclipse TE2000-U inverted microscope coupled with a Visitech VT-Eye laser confocal system as pictured in

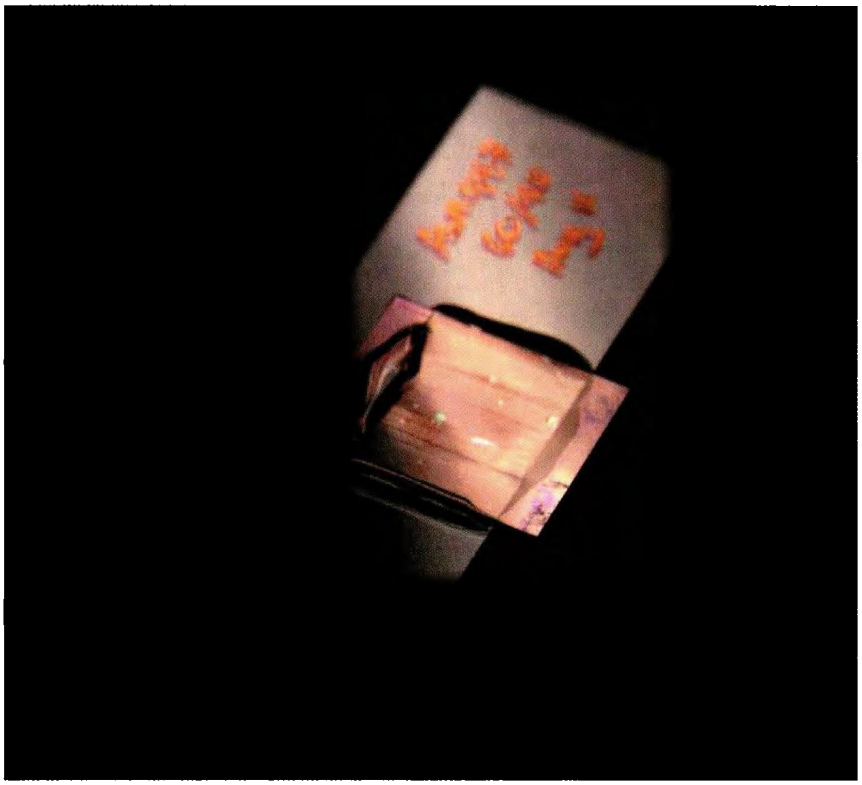

Figure 3.2: Electric field cell for linear fields parallel to gravity

figure 3.3. It is equipped with a white light, a mercury lamp and 561 nm and 491 nm excitation laser sources. To resolve individual particles in three dimensions a 100x Plan Apochromatic oil immersion microscope objective with a numerical aperture, $NA = 1.40$, is used. The higher the numerical aperture, the smaller the resolvable object where resolution, R, is defined by,

$$R = \frac{0.61\lambda}{NA}. \tag{3.1}$$

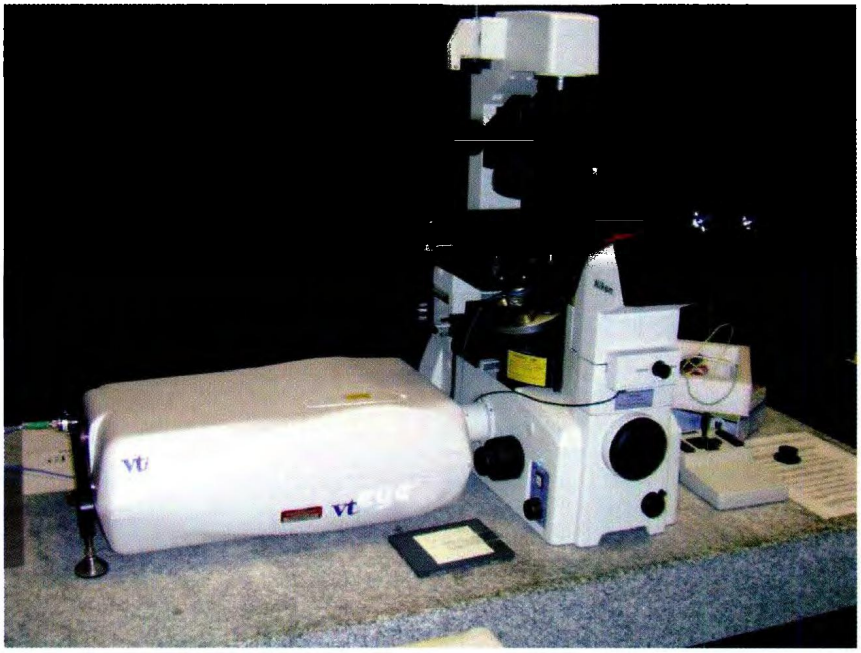

Figure 3.3: Nikon Eclipse TE2000-U inverted microscope (right) with Visitech VT-Eye confocal unit (left).

The sample is placed upside down on the imaging stage which is capable of translating the sample in x and y (horizontal) directions. A drop of imaging oil is placed on

the lens and the lens is moved upwards until the oil makes contact with the sample. Using the microscope binoculars and the white light source to illuminate or mercury lamp to fluoresce the sample, one can find the focus depth of the beginning of the sample and then move to the general area of interest. Once this is done the rest of the work is done using computer software. Voxcell Scan is the software used to control the VTeye confocal system. Contained within the software is control for laser power, confocal aperture, imaging frame rate, an automated experiment control, and more including the focus depth using an electronic z-stage called the Nanofocus. The Nanofocus can image over $100\mu m$ in $0.01\mu m$ increments. This particular confocal apparatus uses a rotating mirror and an acousto-optic crystal to scan in x and y, as opposed to two rotating mirrors used in many other confocal microscopes. The mirrors are limited in speed due to mechanical operation, while the acousto-optic crystal is able to scan the laser beam at significantly faster speeds. However, the image quality is poorer compared to the slower mechanism. The confocal apparatus allows us to scan an area of $5898\mu m^2$ at $29fps$ with $0.15\mu m/pixel$. This is on the lower end of imaging speed. Frame rates over $100fps$ are possible, but a smaller area is scanned and image quality is reduced. With the capability of high frame rates, the increased z resolution due to the confocal, and the ability to scan in z with the Nanofocus as well as x and y, this apparatus is able to image in both two dimensions and three dimensions non-invasively.

3.3.1 Imaging the Colloidal Sediment

For the purposes of this work there were two imaging methods used. The first entails obtaining three dimensional images of the entire colloidal sediment. This method is done by manually focusing just below the bottom plate of the sample, where a layer of particles typically remain stuck due to charge. The Nanofocus is set to $0\mu m$ at this point. An end point for the imaging is chosen to be at some height into the sediment where particles are no longer visible ($\sim 60 - 70\mu m$ in this case). The automated imaging procedure (referred to as *Z-stack capture*) collects two dimensional images as the Nanofocus shifts the focus further into the sample with each image until it reached the end point. This shift in focus is referred to as the Z-step and in this work is set to $0.15\mu m$, comparable to the $\mu m/pixel$ value in the x and y. However the resolution in the z direction is still less than in the x and y, due to anisotropy in the diffraction limited spot. It is important that the z-step is fine enough so that image processing software (discussed more in section 3.4) can resolve individual particles. Once the z-stack capture has scanned through the entire sediment the series of images can be combined to form a three dimensional pseudo-static representation of the sediment. The reason it is only pseudo-static is as follows. It is important to image fast enough so that an entire particle is imaged before it moves significantly, otherwise the recreated three dimensional image of that particle will not be spherical. A frame capture rate of 29 frames per second (fps) is more than enough in this case to satisfy this condition. However, once past that sphere it will move a significant distance from its original position before the image of the sediment is completed, but this is acceptable, as the sediment is already at equilibrium and particles are merely diffusing. For the smaller

particles (and the binary system to be discussed). we imaged at $56fps$ with a 512 x 256 image (as opposed to the 512 x 512 used normally). This gives us the same micron/pixel conversion but allows us to image faster for the smaller particle sizes.

3.3.2 Imaging 2D Diffusion

The second method used is to image 2D time-series at different heights in the sediment. The purpose of this method of imaging used in this work is to study diffusion. Again the microscope is focused near the bottom plate and then moved into the area just past the plate to where freely diffusing particles are at the bottom of the sediment. A 200 frame movie is captured at $29fps$ (or $56fps$ as mentioned above). This is done in a z-series, where after every movie the height in the sample is increased by one particle diameter and another image is taken. This is repeated until the end of the sediment. In this case imaging speed is again important. The time between frames ($\mathbf{d}t$) must be much smaller than the Brownian time, τ_D, so that the distance moved by one particle between two frames is much smaller than its diameter. This is needed to extract proper diffusion data from the particles trajectories.

3.4 Image Processing using IDL

The next and final step in our experimental procedure is to extract information from our 3-dimensional, and time series images from our confocal microscope. We do this using Interactive Data Languag (IDL). This is a language that is popular for particle tracking in the scientific community, and has many procedures and functions available

for download listed on researchers websites. In this project we followed a particle tracking tutorial by Eric Weeks, and used modified versions of several procedures provided by Weeks [30] and and described by Crocker and Grier [31].

3.4.1 Extracting Particle Locations in the Colloidal Sediment

The image format that must be used for the following procedures is a 8-bit Tagged Image File Format, or Tiff (*.tif). The tiff is a stack of greyscale images with a black background, and the fluorescing spheres showing up white. Each image in the stack is a 2D slice of the colloidal sediment, with the entire stack representing the sediment from bottom to top. If not originally in this configuration, images can be edited and converted to 8-bit tiff using image processing software such as ImageJ, availble free for download from rsbweb.nih.gov. The tiff is then read into IDL and is then represented by a 3-dimensional array, with each point corresponding to the pixel value (from 0 to 255) at that point in the image stack. The first step in the image processing is to filter out background noise using a spatial bandpass filter. The procedure *bpass3d.pro* filters the image 3-dimensionally by convolving a Gaussian-like function with a defined width similar to our features. The result of this band pass can be seen in a 2-dimensional example in figure 3.4.

Once filtered, particle coordinates need to be extracted from the image stack. This is done using *feature3d.pro*. This procedure requires the suggested particle diameter, particle minimum separation, and optionally (but usually required for real results) a

Figure 3.4: A sample of a 2-dimensional image of colloids before (left) and after (right) a spatial bandpass filter has smoothed 1-pixel noise.

minimum integrated brightness value, all as user defined inputs. The procedure then finds all the local brightness maxima in the image using a 3-dimensional anisotropic parabolic mask with the same dimensions as the user defined set particle diameter. These maxima correspond to what the procedure considers to be particle centers. Returned are the particle positions in x, y, and z (pixels), integrated brightness value of the feature, the squared radius of gyration (note: this is not a true radius of gyration, but one which substitutes brightness for mass to give an indication of feature size), and several other columns of information that for the scope of this work are not used. To get an idea of what is a real particle and what is not, it is helpful to plot the integrated brightness against the squared radius of gyration. As seen in figure 3.5.

There are initially (before clipping the data) many more features with very low brightness values and a wide spread of the radius of gyration. These correspond to

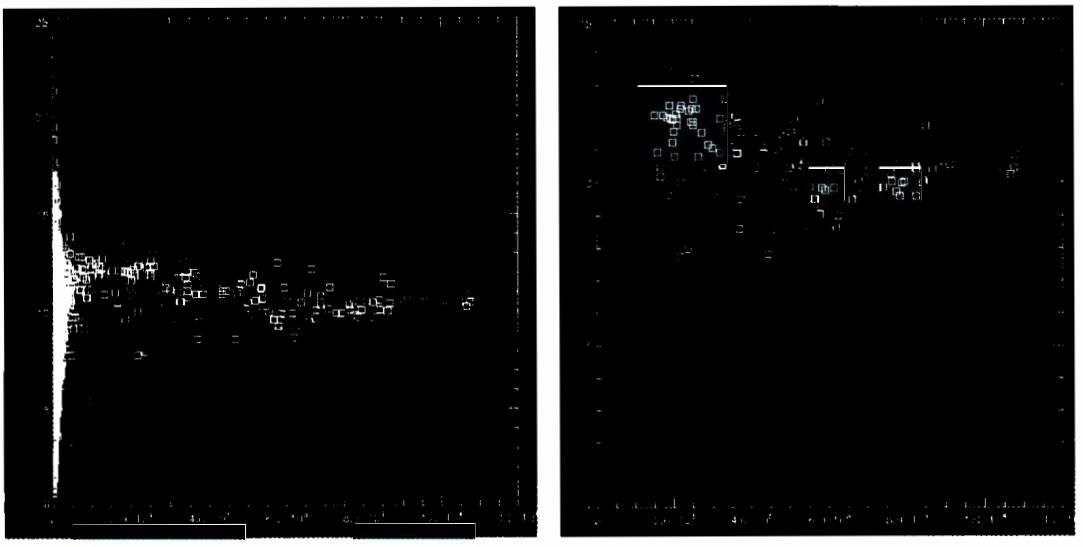

Figure 3.5: Squared Radius of Gyration vs. Integrated Brightness as given by the procedure feature3d.pro for all the features found (left). Features found after the data has been clipped according to brightness values (right).

spurious image data that the procedure confuses to be particles. At higher brightness values we can see there are only several features, all within similar radius of gyration values which number around the same number of particles as we can count by eye. This helps us choose a value for our minimum brightness cutoff. The post-clipped data shows all the low brightness features to be eliminated leaving only our true features. The data can be clipped by running feature3d.pro again, which due to the 3-dimensional convolution is rather time consuming, or the original output of feature can be clipped using the integrated brightness as the clipping parameter using the procedure, *cclip.pro*. This is just a simple array operation and is much quicker. This feature-finding procedure is optimized for particles at least 5 pixels in diameter, and the resulting centroid coordinates will have errors on order of 0.1 pixels for images with low noise. This procedure is also optimized for low particle concentration systems. This procedure can also be done on a 2-dimensional image using similar procedures

as above also available from Eric Weeks, feature.pro and bpass.pro, etc.

3.4.2 Extracting a Sedimentation Profile and Equation of State

Once all the particle coordinates are found, we can then use them to calculate the sedimentation profile for the sample. To do this we count all the particles in each z-slice of the image stack and plot that as a function of z. This gives us particle number vs z. The local volume fraction is the volume of particles in a given section, divided by the volume of that section. This is defined as

$$\Phi_{local} = \frac{n_{local}\frac{4}{3}\pi a^3}{A\Delta z}, \tag{3.2}$$

where Φ_{local} is the local volume fraction at a given height, a is particle radius, A is the area imaged, Δz is the Z-step, and n_{local} is the number of particles counted in the reference area A between height z ad $z + \delta z$. Plotting this against z gives us our sedimentation profile.

From sedimentation profiles we are then able to extract the EOS for this system using equation 2.6 to calculate the osmotic pressure, Π, and plot it against the volume fraction, Φ_{local}. Comparison with the Carnahan-Starling EOS allows us to establish any deviation from hard-sphere like behaviour.

3.4.3 Calculating the Diffusion Coefficient

The diffusion coefficient data is also a tiff image stack, however rather than consecutive images corresponding to a change in height, in these images it corresponds to a change in time. This is the type of imaging described in section 3.3.2, called a time-series. Using the 2-dimensional equivalent of feature.pro as well as the other procedures previously described, all the particle centers are found in every frame. As discussed in chapter 2, the diffusion of a particle can be calculated from it's change in position over time by calculating its mean squared displacement (MSD), by the relation in equation 2.3. The procedure, track.pro, is called which, using a user defined maximum displacement in pixels for one time step, assigns each particle a unique ID and decides what features coincide with that ID in every successive frame. We then have a particle center for an identified particle as a function of time. To get better statistical averages we calculate the MSD multiple times for each particle for each time step length, and then average. Consider as an example the calculation of a 1-dimensional MSD for several particles with 4 positions in time. To calculate the MSD for one time step normally one does the following:

$$\langle x_1 - x_0 \rangle^2.$$

With the averaging we can consider every point a "first" point for a different particle. Mathematically we do this the following way:

$$\frac{\langle x_1 - x_0 \rangle^2 + \langle x_2 - x_1 \rangle^2 + \langle x_3 - x_2 \rangle^2}{M}.$$

where M here is the number of iterations of this averaging. Notice that there are two averages taking place; a thermal average over all of the particles, as well as an

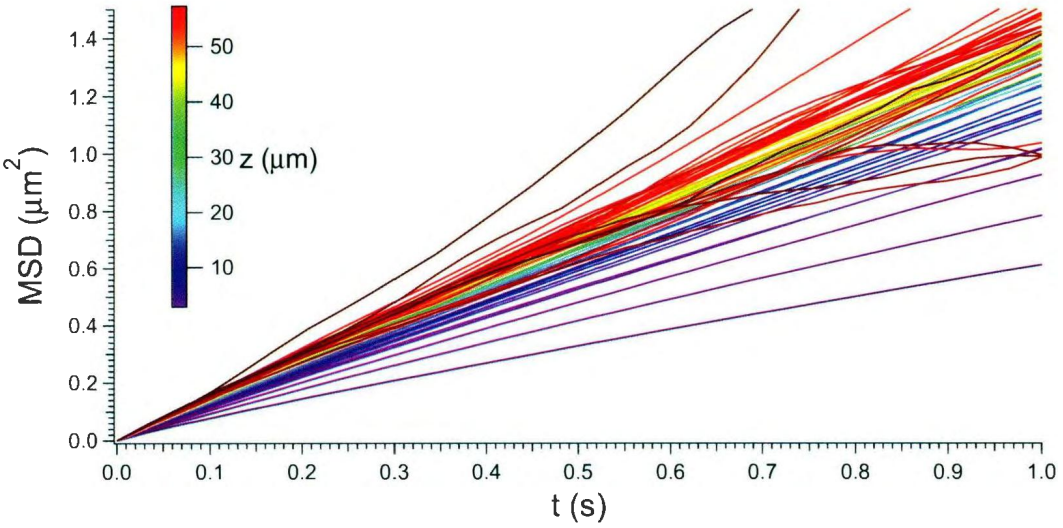

Figure 3.6: MSD as a function of time for $1\mu m$ PMMA colloids in 60:40 decalin/TCE. This plot is cropped for short times to show the region fit for diffusion coefficient calculation.

internal averaging over each individual particle track. This second averaging can be done for one time step right up to the length of the track. However for the maximum length there will only be one value, and for one less than the length of the track there will be two values, etc. Once the MSD is calculated it is plotted against time, as seen in figure 3.6, and from the slope of a section at small times of this graph we can then determine the diffusion coefficient for the particles in this particular image. Seen in the figure, not all curves are perfectly linear. Only the first twenty points are fit to obtain the diffusion coefficients (to around $0.7s$). These fits are weighted with the error (standard deviation), as shown in the Results section in figure 4.16. The diffusion coefficient calculated here is the short-time self-diffusion coefficient

$$D_s^S = D_0(1 + K_s^S\phi), \tag{3.3}$$

where K_s^S is the hydrodynamic factor. The theoretical values for the shot-time hydrodynamic factor vary from 1.7-1.8 [32, 33].

Chapter 4

Results and Discussion

Two kinds of measurements were carried out in this thesis. First, static sedimentation profiles of the colloidal suspension were obtained in zero field and at different values of an AC external electric field (at a frequency of 1 MHz). Second. under the same conditions, dynamical measurements were carried that yielded a height profile of the diffusion coreffficient. These measurements were carried out for three systems.

4.1 Sedimentation profiles of hard-sphere colloids in an external field

In this section we will be testing a system of PMMA colloids in a decahydronaphthalene (decalin) and tetrachloroethylene (TCE) solvent for hard-sphere behaviour. We will also be examining the system for dipolar response in an AC electric field. This will be done by analysing the sedimentation profiles obtained using a confocal microscope and extracting from them the equation of state for the system.

	PMMA	50:50	60:40	70:30
ρ (kg/m^3)	1259	1259	1186.4	1113.8
n	1.4895	1.4895	1.4864	1.4833
ϵ_r	2.6	2.35	2.32	2.29
l_g (μm)	-	$\gg 100$	10.9 $(2a = 1\mu m)$	10.7 $(2a = 0.8\mu m)$

Table 4.1: Density, index of refraction, and dielectric constants for the PMMA particles and three solvent mixtures composed of 50:50. 60:40, and 70:30 (by volume) ratios of decalin and TCE. In addition, the calculated gravitational lengths used in the corresponding experiments are listed.

First we report the static equilibrium sedimentation profile of our colloidal suspension and use it to obtain the equation of state (EOS) of the system. The sediment is imaged by rapidly acquiring a z-stack ($77\mu m$ x $77\mu m$ x $108\mu m$) in $0.15\mu m$ z-increments to match the $\mu m/pixel$ value of the 2D images acquired. The EOS is then obtained from the sedimentation profile as seen in figure 4.1, and discussed in section 3.4.2. As shown in table 4.1, the 50:50 decalin/TCE solvent mixture and the PMMA spheres are density matched with $\rho = 1.259 g/cm^3$, making the gravitational length, l_g, significantly larger than the sample thickness.

4.1.1 $1\mu m$ PMMA in 60:40 decalin/TCE mixture

Using the 60:40 solvent mixture allows a density mismatch between the PMMA particles, and the new solvent mixture with $\rho = 1.19 g/cm^3$, gives $l_g = 10.9\mu m$, seen in table 4.1. Seen in figure 4.1 are the sedimentation profiles, obtained by particle counting a fast 3D z-stack of the entire sample. The initial peak located at the bottom wall

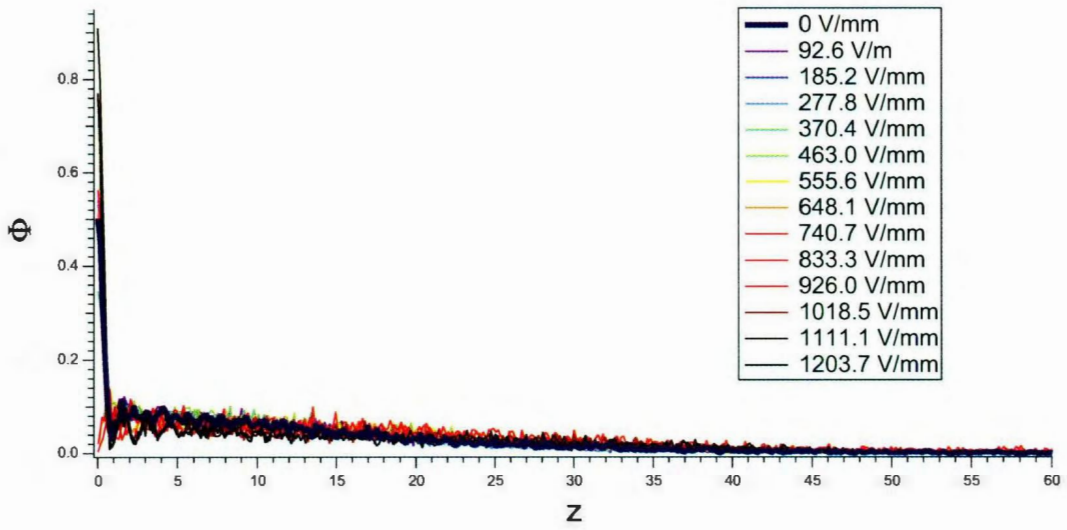

Figure 4.1: Sedimentation Profiles for a range of sinusoidal peak-to-peak field strengths from $E = 0V/mm$ to $E = 1207.7V/mm$ obtained from counting particles using feature finding program for $1\mu m$ diameter PMMA colloids in 60:40 decalin/TCE. The large spurious peak at zero is due to particles stuck at the substrate and is how we define $z = 0$.

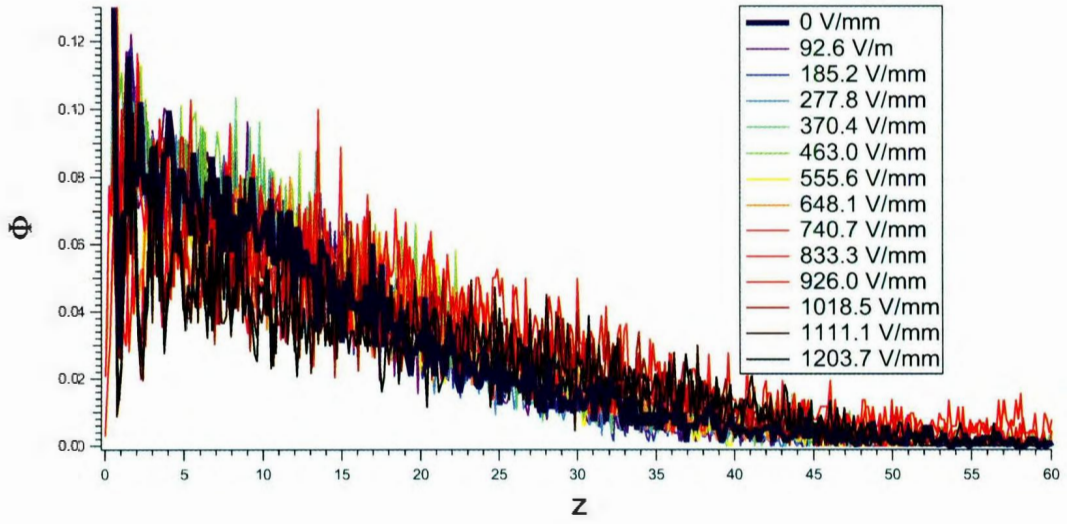

Figure 4.2: Zoomed in sedimentation profiles for a range of field strengths from $E = 0V/mm$ to $E = 1207.7V/mm$ obtained from counting particles using feature finding program for $1\mu m$ diameter PMMA colloids in 60:40 decalin/TCE. The noise in the data is due to low statistics.

of the sample is defined as $0\mu m$. Counting is poor here due to a high concentration of particles stuck to the wall (the software has trouble detecting individual particles correctly at high volume fraction, or VF). As can be seen, the data for the rest of the curve is quite noisy, and can be seen more clearly in figure 4.2. Without a smoothing technique, not much can be discerned from this graph. However we find that using

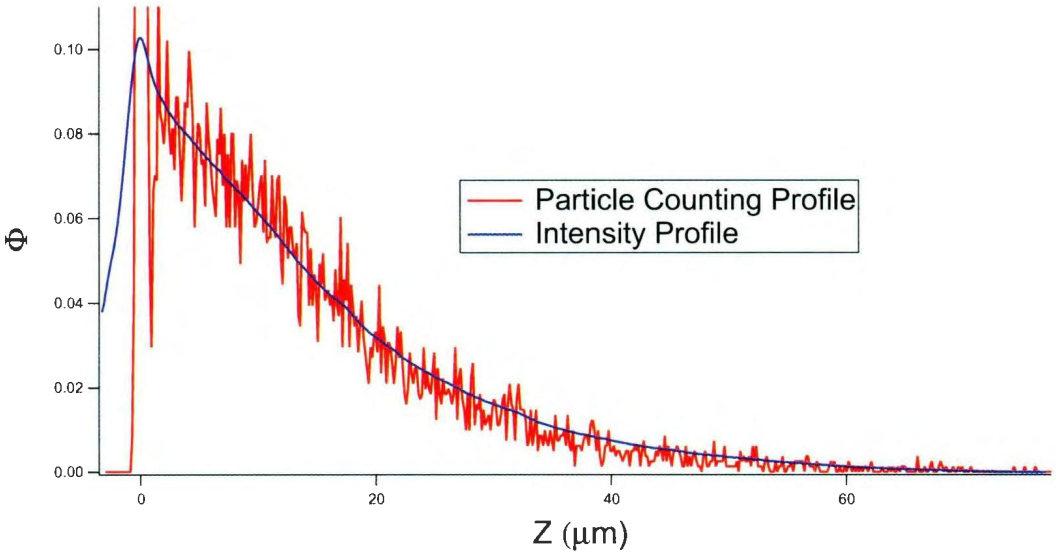

Figure 4.3: Zero-field sedimentation profiles obtained from particle counting and summed intensity for $1\mu m$ diameter PMMA colloids in 60:40 decalin/TCE compared.

the summed intensity of each image in the z-stack and a correction technique [34], a plot of the corrected intensity as a function of z shows good agreement with the particle counting technique, as seen in figure 4.3. In what follows, we will use the intensity method (rather than a smoothing of the particle counting results) to show our sedimentation profiles.

Shown in figure 4.4 are the intensity sedimentation profiles, i.e. ϕ as a function of z.

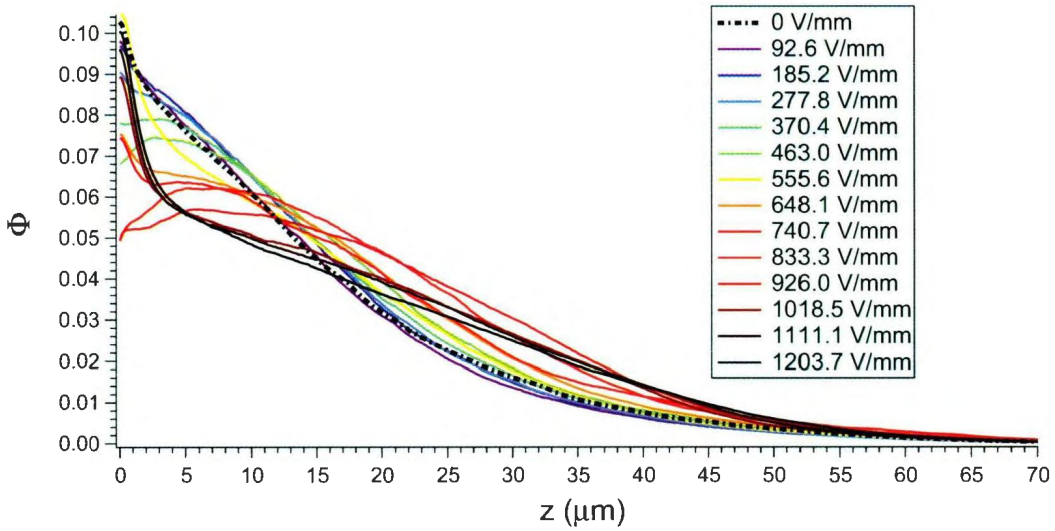

Figure 4.4: Intensity sedimentation profiles for a range of field strengths from $E = 0V/mm$ to $E = 1207.7V/mm$ for $1\mu m$ diameter PMMA colloids in 60:40 decalin/TCE. The gravitational legnth, l_g in this system is $10.9\mu m$.

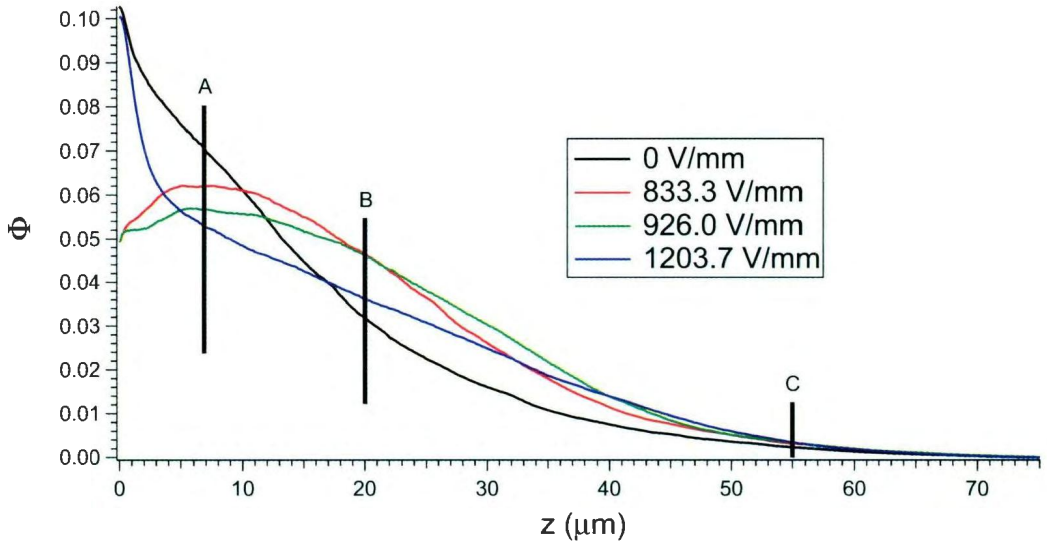

Figure 4.5: Four field strengths are selected showing the transition from individual particles to chains, and three regions in the sample are highlighted to show this change in the different regimes. Intensity sedimentation profiles for $1\mu m$ diameter PMMA colloids in 60:40 decalin/TCE.

Four field strengths are chosen to highlight the transition from independent particles to chain formation: this is shown in figure 4.5. A snapshot of these sediments at these selected field strengths can be shown in figure 4.6. We notice that for $E = 833.3V/mm$

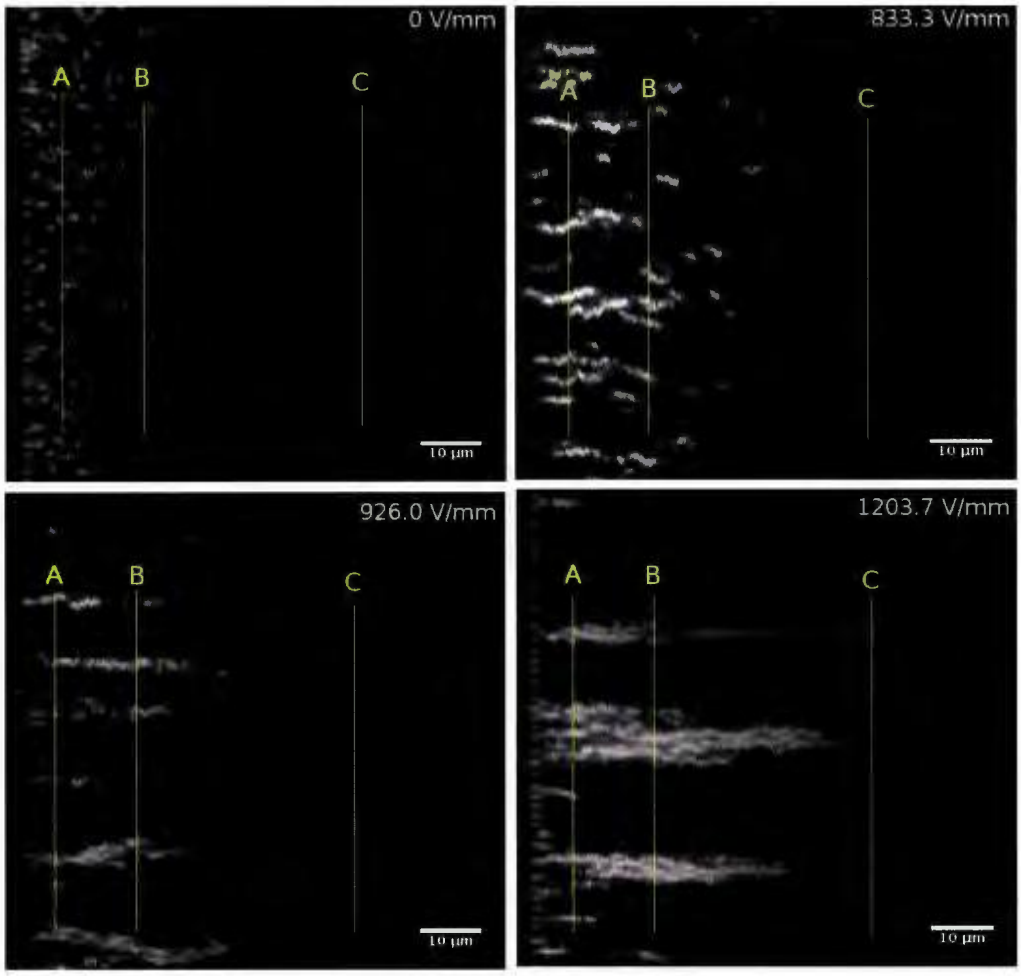

Figure 4.6: XZ transposed images of the sediment of $1\mu m$ PMMA colloidal sediments in 60:40 decalin/TCE at selected field strengths (gravity to the left, and z increasing to the right).

and $E = 926.0V/mm$, there is no peak at the beginning of the sediment, while at $E = 0V/mm$ and $1203.7V/mm$ there is. When we examine the images these data sets are taken from (figure 4.6), we see that the layer of particles stuck to the substrate

has been bleached by the laser. The peak returns at higher field as we moved our region of interest to an area that is not bleached. In order to compare the zero field system to a hard-sphere system we must calculate the experimental equation of state and compare with the Carnahan-Starling equation of state [6]. This, along

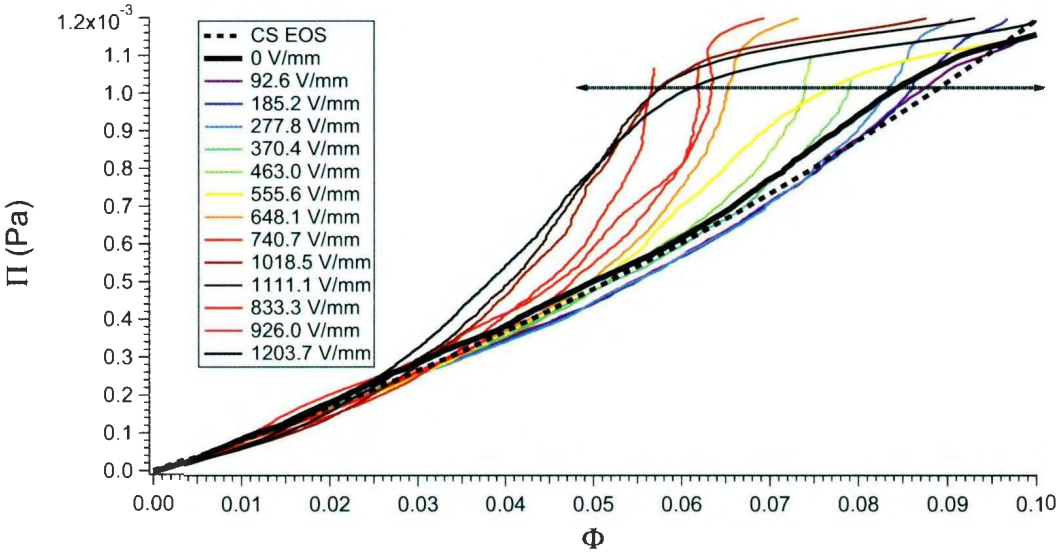

Figure 4.7: Equations of state for a range of field strengths from $E = 0V/mm$ to $E = 1207.7V/mm$ for $1\mu m$ diameter PMMA colloids in 60:40 decalin/TCE, calculated from the intensity sedimentation profiles. The horizontal line denotes the area above which will likely have boundary effects.

with the calculated EOS as a function of field strength, is shown in figure 4.7. The horizontal line drawn at$\sim$ $1mPa$ in this figure denotes the area above which we likely have boundary effects. In figure 4.8 we highlight the EOS for the same field strengths chosen in figure 4.5 and 4.6. We can see that up to about $\phi = 0.065$ the zero field EOS for $1\mu m$ PMMA particles shows excellent agreement with what is expected for a hard-sphere EOS from the CS relation. This shows that, for low particle concentration, our system is an approximate hard-sphere system and is in

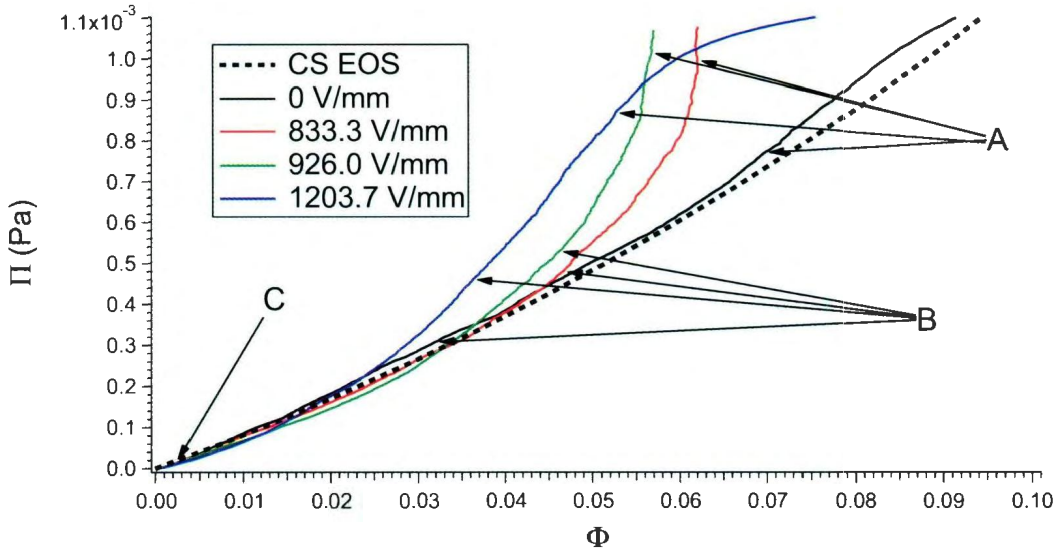

Figure 4.8: Selected field strengths with the regions A, B, and C highlighted. Equations of state for $1\mu m$ diameter PMMA colloids in 60:40 decalin/TCE, calculated from the intensity sedimentation profiles

agreement with the literature [3, 7]. This is in spite of the slight mismatch of index of refraction to allow density mismatch for sedimentation, which in principle might increase the van der Waals attractions. At higher field strengths, we can again see that at lower VF, corresponding to higher positions in the sample, these also agree with the hard-sphere EOS. As one goes up in the sediment, i.e. with decreasing ϕ, the $E = 833.3V/mm$ and $E = 926.0V/mm$ field strengths align with the CS relation for VF below $\phi = 0.03$, while the $1203.7V/mm$ field strength only does for $\phi < 0.02$. This shows that, high enough in the sediment, or at low enough VF, hard-sphere behaviour is seen in the structure except for extreme cases of high electric field strength.

Past work on the study of experimental equations of state of hard-sphere-like colloids in an external field had one challenge: the zero field EOS was not in agreement

with the Carnahan-Starling EOS [15]. Much commentary has also been made of the search for the true hard-sphere system [14,30]. The agreement in a system where both density and refractive index can be matched is remarkable, and is discussed more in section 3.1.4.

4.1.2 $0.8\mu m$ PMMA in 70:30 decalin/TCE mixture

We now look at the same structural analysis for smaller, $0.8\mu m$ diameter PMMA colloids. In this second case the solvent used was a mixture of decalin and TCE with a 70:30 ratio by volume. This makes the density mismatch slightly greater preventing the smaller and lighter particle sediment from spanning the entire sample. At this solvent ratio $\Delta\rho = 145.2kg/m^3$, keeping the gravitational length similar to the previous case, at $l_g = 10.7\mu m$, as shown in table 4.1. In order to extract equations of state, the sedimentation profile must go to zero before being constricted by a rigid boundary.

As in the previous experiment, we proceed with analysing the structure of the sediment through the use of sedimentation profiles and extracting the EOS. Shown in figure 4.9 are the sedimentation profiles for $2a = 0.8\mu m$ particles, and shown in figure 4.10 are seven selected field strengths highlighted in four regions of the sediment. These field strengths and regions were chosen in order to compare with the previous experiment as well as to highlight transitions in the chain structure. Again a snapshot of these sediments at the selected field strengths is shown in figure 4.11. From these sedimentation profiles we can that see as electric field is increased, the lower area

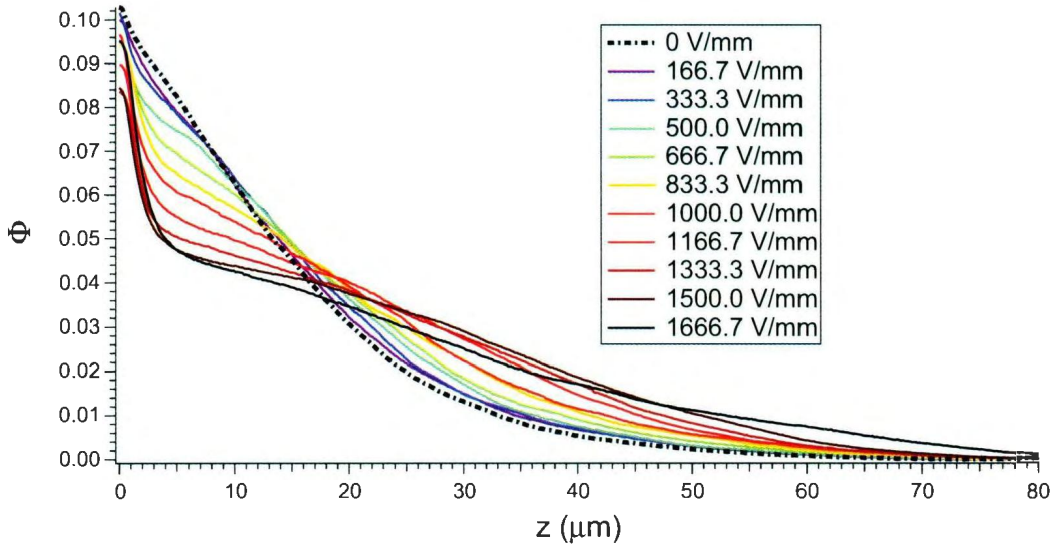

Figure 4.9: Intensity sedimentation profiles for a range of field strengths from $E = 0V/mm$ to $E = 1666.7V/mm$ for $0.8\mu m$ diameter PMMA colloids in 70:30 decalin/TCE. The gravitational length, l_g, in this system is $10.7\mu m$.

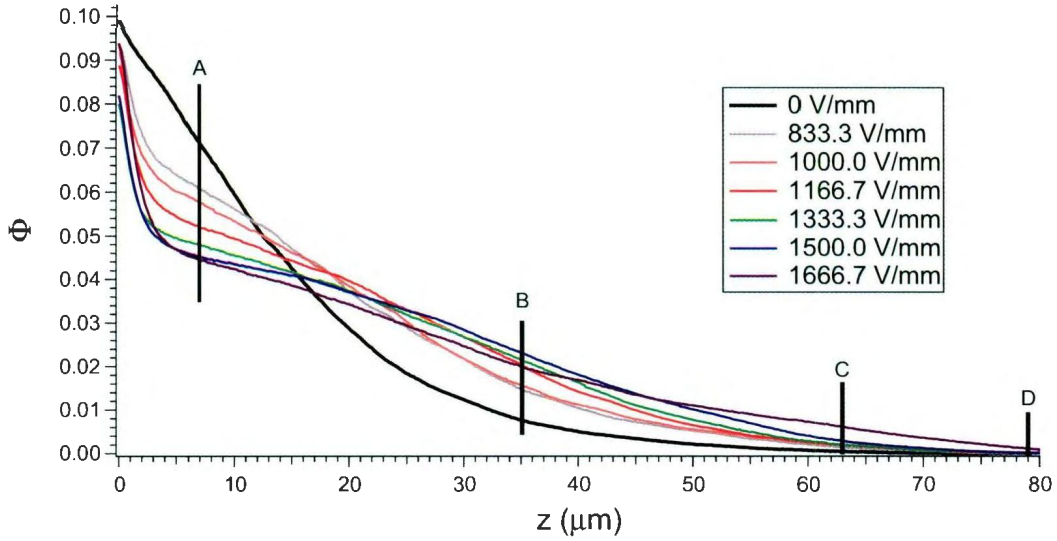

Figure 4.10: Seven field strengths are selected showing the transition from individual particles to chains, and four regions in the sample are highlighted to show this change in the different regimes. Intensity sedimentation profiles for $0.8\mu m$ diameter PMMA colloids in 60:40 decalin/TCE.

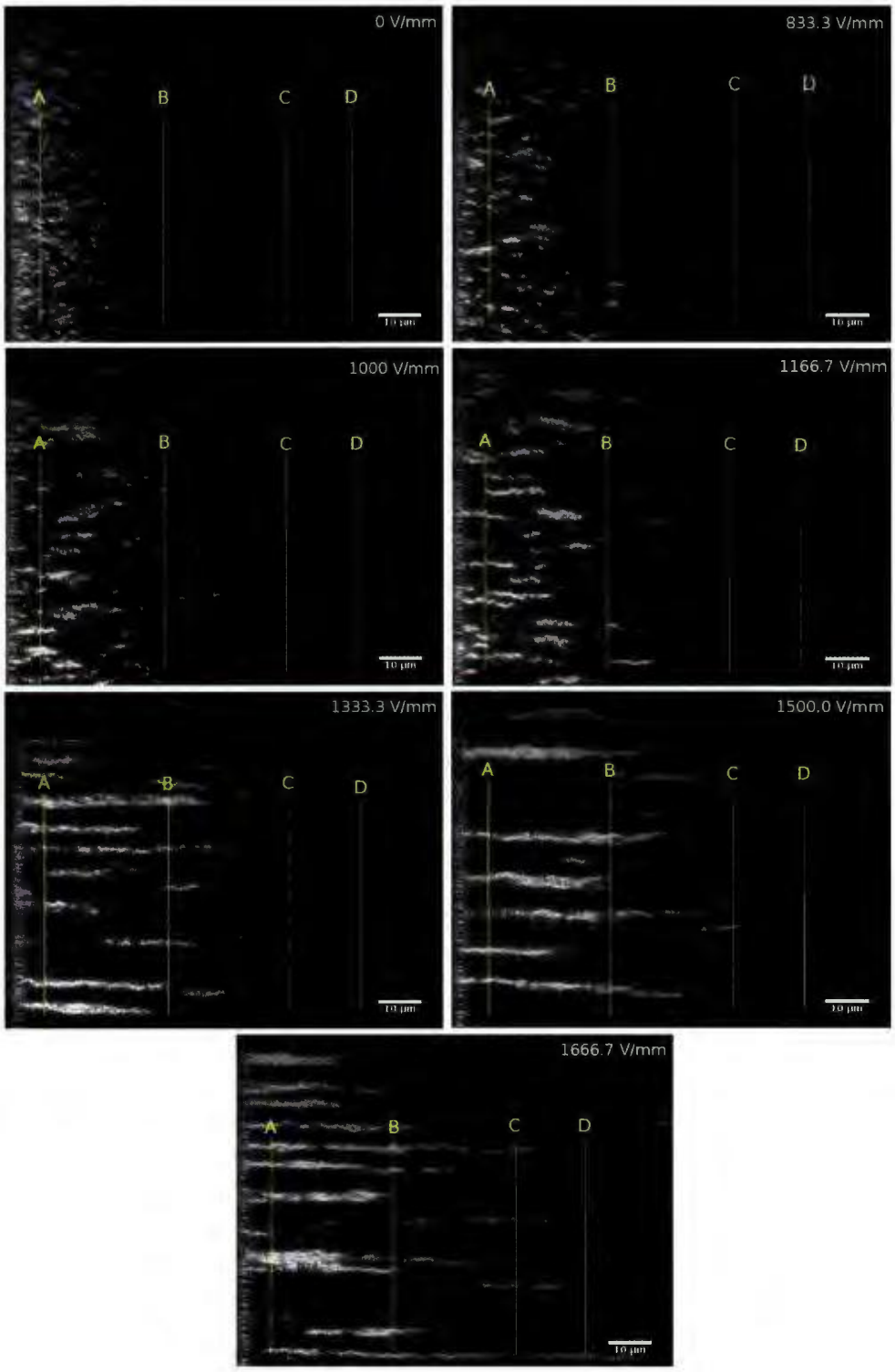

Figure 4.11: XZ transposed images of the sediment of $0.8\mu m$ PMMA colloidal sediments in 70:30 decalin/TCE at selected field strengths (gravity to the left, and z increasing to the right).

in the samples become depleted with the VF decreasing. The particles lost here are pushed upwards, and for higher field, extend the sediment via long chains. In the $1666.7 V/mm$ case, the VF near the bottom of the sample is reduced by almost half. We again want to confirm if our zero field example is indeed hard-sphere like, and to do this we again extract the EOS from these profiles, shown in figures 4.12 and 4.13.

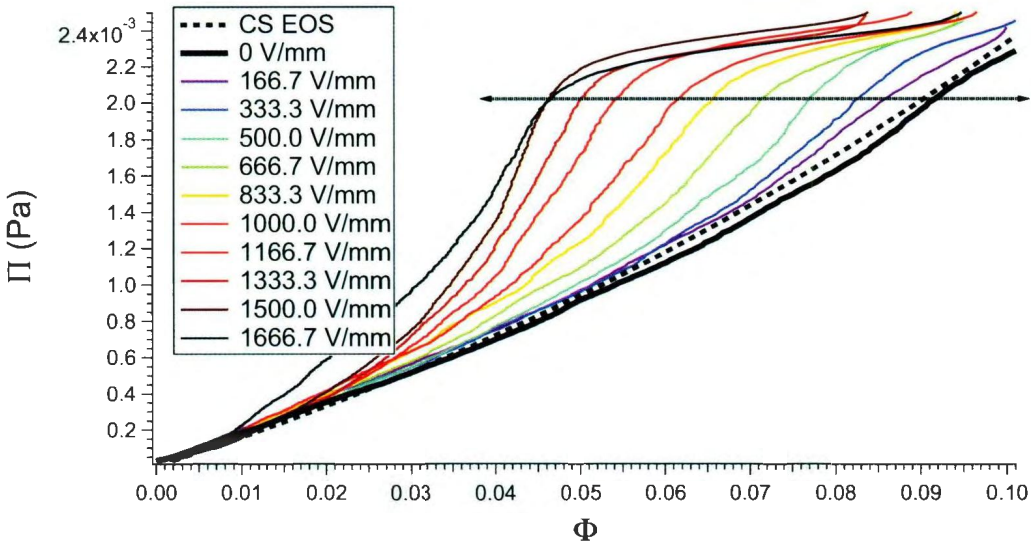

Figure 4.12: Equations of state for $0.8\mu m$ particles, calculated from the intensity sedimentation profile. The horizontal line denotes the area above which we expect boundary effects.

Plotted along with these is the Carnahan-Starling equation of state calculated for $0.8\mu m$ diameter spheres. Again in figure 4.12 the horizontal line seen in this figure denotes the area above which we expect boundary effects. The results for this particle size again shows excellent agreement with theory at zero-field, and throughout the entire range of experimental VF. This shows again, that this sample is hard-sphere like in the restricted region of a microscope slide even at a higher index of refraction mismatch (off by 0.012, see table 4.1), agreeing with other experiments [3]. Due to the

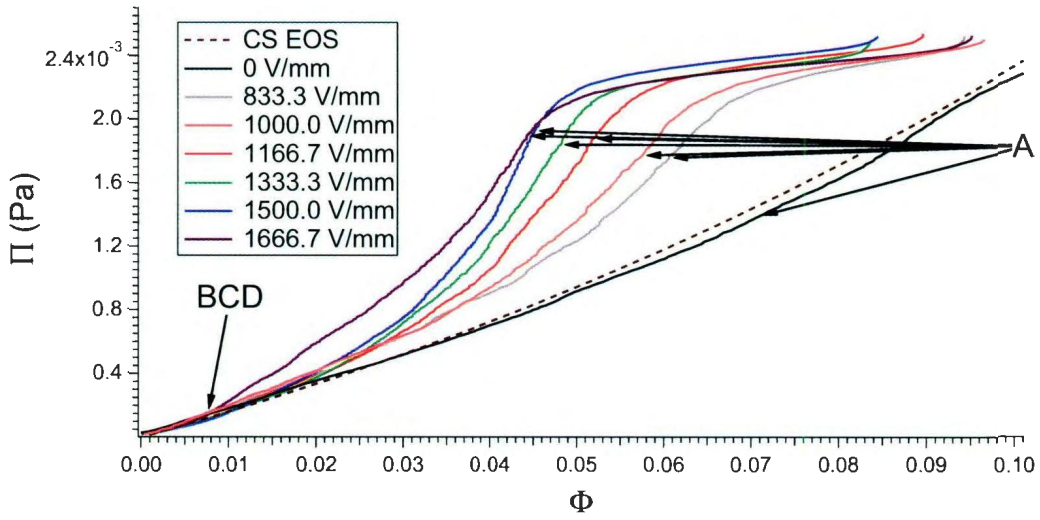

Figure 4.13: Selected field strengths with the regions A, B, C, and D highlighted at their corresponding ϕ values. Equations of state for $0.8\mu m$ particles, calculated from the intensity sedimentation profile.

absence of theoretical literature on the EOS of dipolar hard-spheres, we have restricted our comparison to the hard-sphere EOS. These results now enable comparisons of two separate particle sizes to simulations of hard-sphere-plus-dipolar systems.

4.1.3 Comparison of the zero-field profiles for both monodisperse experiments

In order to objectively compare the sediment of these two systems ($2a = 1\mu m$ in 60:40 decalin/TCE and $2a = 0.8\mu m$ in 70:30 decalin/TCE) we can plot the sedimentation profile in the dimensionless form of ϕ vs. z/l_g. By plotting sedimentation profiles of different systems in this manner, we can estimate from the differences in the plot any error in particle size as ϕ is proportional to a^3. We can see the zero-field sedimentation profile for both experiments plotted together in figure 4.14. Both curves appear to

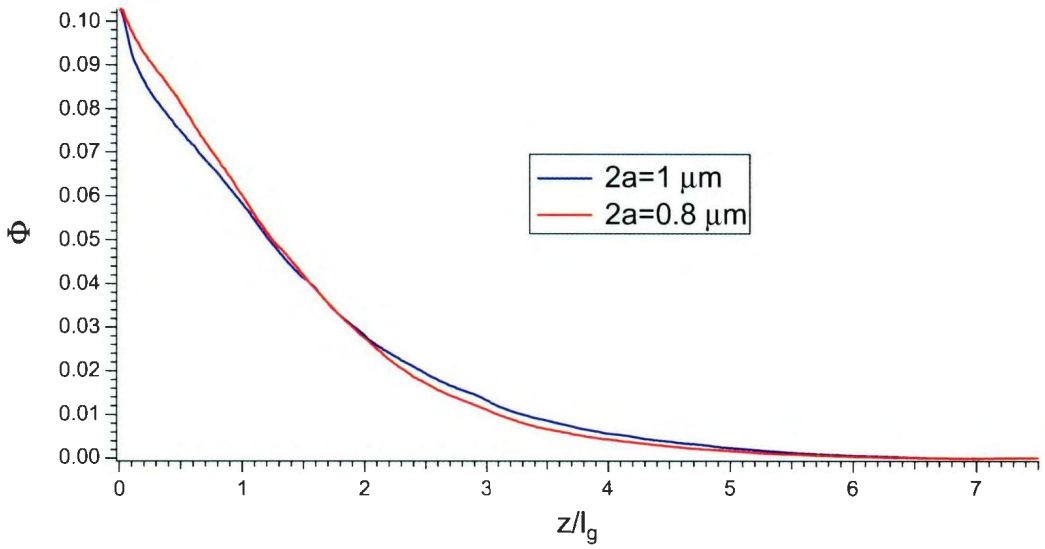

Figure 4.14: By plotting the volume fraction, ϕ, against the dimensionless z/l_g, we are able to show a sedimentation profile which is not effected by particle diameter. Zero-field sedimentation profiles for $2a = 1\mu m$ PMMA colloids in 60:40 decalin/TCE and $2a = 0.8\mu m$ PMMA colloids in 70:30 decalin/TCE.

agree with one another quite well, indicating that our particle size ratio (estimated by microscopy) is indeed correct.

4.2 Diffusion of Colloidal Clusters

To calculate diffusion coefficients we must plot the MSD against time. From a linear fit of this plot, we see from equation 2.3 that the slope of this line will be equal to $4D$. An example of this fit can be seen in figure 4.15. This is the same data shown in figure 3.6 with only three MSD data sets at different heights in the sample shown, in order to clearly show the fit. From this fit, and the error in the fit we calculate the diffusion coefficient and its error at this height in the sample. We fit these curves for relatively short times, just the first twenty data points out of two hundred (i.e. the

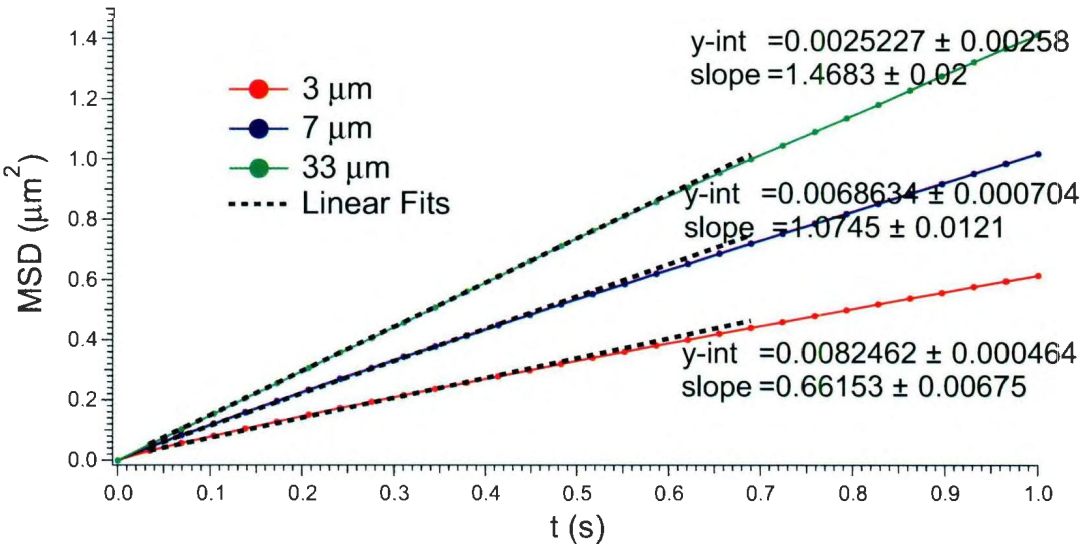

Figure 4.15: MSD as a function of time for $1\mu m$ diameter PMMA colloids in 60:40 decalin/TCE with linear fits. This plot is cropped for short times to show the area fit for diffusion coefficient calculation.

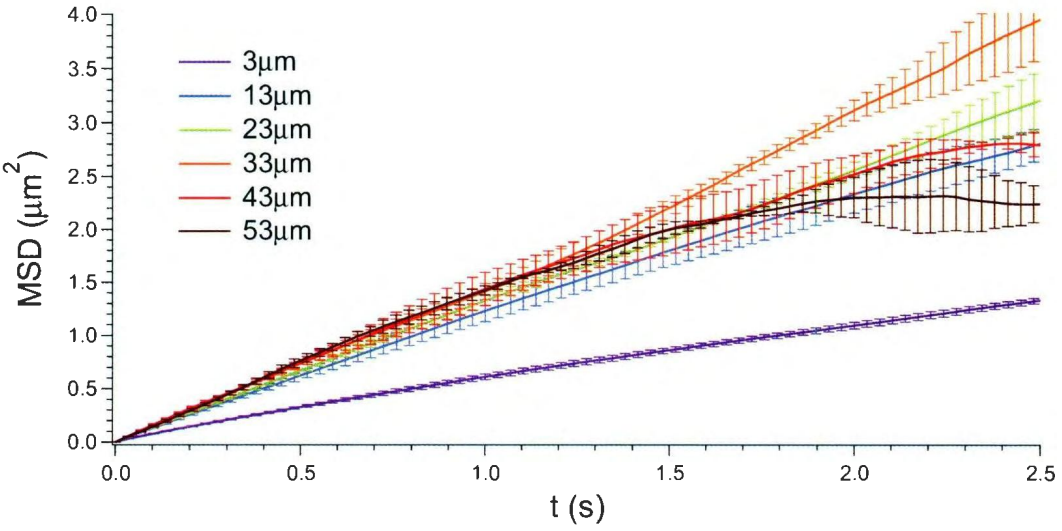

Figure 4.16: MSD as a function of time for $1\mu m$ diameter PMMA colloids in 60:40 decalin/TCE with error shown for duration of experiment. Error bars are calculated from the scatter in the data.

first 0.7 seconds out of 7 seconds of data). Due to the averaging technique used in the MSD calculations, the statistics for very short times are excellent and are decreasing less so as time increases. At the maximum time there is then only one data point for each particle that was tracked for that duration, thus leading to poor statistics. The error in the MSD calculation for the duration of the experiment can be seen in figure 4.16. The error in MSD is taken from the scatter of the data, when in fact error is most likely larger at long times. If only one particle contributes to a data point, then the scatter is zero, and we know that this cannot be the case for the error in the MSD measurement.

4.2.1 Zero-field diffusion in a density matched dilute system

In order to have a reference point for the diffusion coefficients measured, and as well to test the Brownian behaviour of the particles, we first look at the diffusion of a dilute and density matched suspension. For this we use a 50:50 ratio of decalin/TCE to be density matched with $1\mu m$ PMMA colloidal spheres. We dilute the suspension so the total volume fraction (VF) of the particles is $\sim 1\%$. In this case the diffusion should be the same throughout the extent of the sample as the local volume fraction should remain constant and low, making hydrodynamic interactions negligible. The result (shown in figure 4.17), is a diffusion coefficient that is constant through the extent of the sample with a value of approximately $D_0 = 0.42 \pm 0.02 \mu m^2/s$ (the error calculated is derived from the scatter in the data along the plateau). Using an estimated value for viscosity by using fractional values of the known viscosities at $22°C$ for each of our solvents, we use a viscosity of $\eta \approx 1.26 mPa \cdot s$ (calculated from the ratios of the

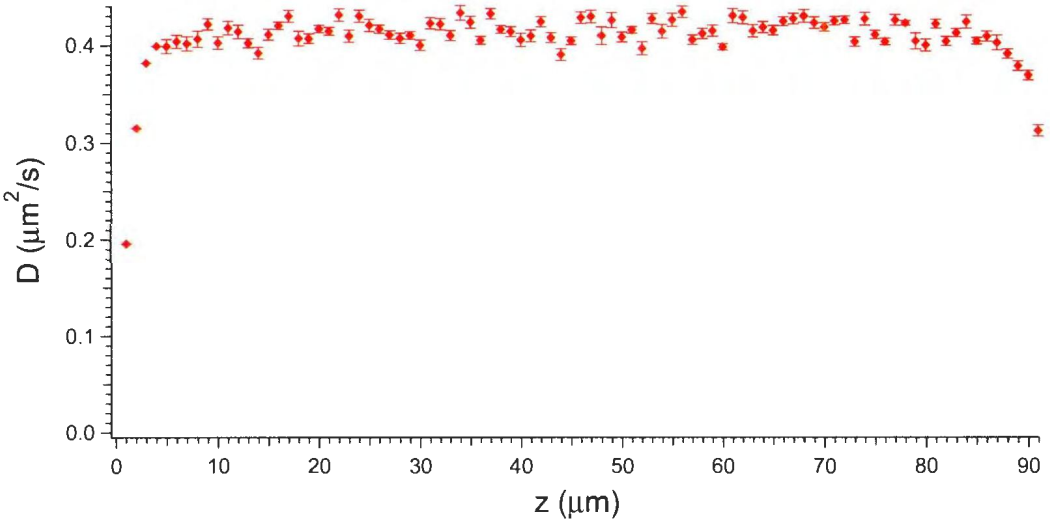

Figure 4.17: Diffusion coefficient as a function of height of $2a = 1\mu m$ PMMA colloids in a density matched suspension of 50:50 decalin/TCE with $\Phi = 1\%$. In this scenario we can measure the bulk diffusion coefficient and can also see the effect the proximity of a rigid boundary has on the diffusion coefficient.

manufactures stated viscosity for each solvent) to calculate our theoretical diffusion coefficient. Our theoretical Stokes-Einstein value is $D_{SE} = 0.34\mu m^2/s$ calculated from equation 2.4. A source of error for this difference could be an incorrect determination of the viscosity due to temperature flux.

There is a systematic decrease from the bulk diffusion coefficient near the top and bottom plates within $7\mu m$, or seven particle diameters, from these boundaries. This is in agreement with previous work by Carbajal-Tinoco *et al* [8], whose work showed the same slowing of diffusion near a rigid boundary.

4.2.2 Diffusion in a thin sediment for $1\mu m$ diameter PMMA in 60:40 decalin/TCE

For the next step in our series of experiments, we prepare a sample for microscopy of a density mismatched colloidal suspension and apply an AC electric field along the direction of gravity (z). The applied AC electric field is at a frequency of 1MHz, and is thus too fast for the electric double layer around the particle to respond. As a result, we expect a dielectric response to be instantaneous on our slow microscopy time scales. In past work, this response has been modelled as a point dipole at the centre of the sphere [9, 10, 26, 35]. Part of the motivation of a detailed study of equations of state and particle dynamics is to provide quantitative evidence with which to evaluate the validity of the point dipolar approximation. The first in this series of experiments is a 60:40 (by volume) solvent of decalin and TCE respectively with $1\mu m$ diameter PMMA particles. Time series are taken at different depths across the sediment at intervals of $1\mu m$, chosen to match the particle diameter. The electric field is then increased and allowed to equilibrate for $\sim$ 15mins: then the experiment is repeated. In figure 4.18 we see the results for the diffusion coefficient as a function of height for different electric field strengths. At $0V/mm$ the diffusion as a function of height increases to a plateau level representing the bulk diffusion coefficient, $D_0 = 0.38 \pm 0.01\mu m^2/s$.

There are two hydrodynamic effects observed in the density-mismatched sample in figure 4.18 that are directly or indirectly related to the wall. The first is a wall-sphere hydrodynamic effect, also seen in the density matched sample (figure 4.17)

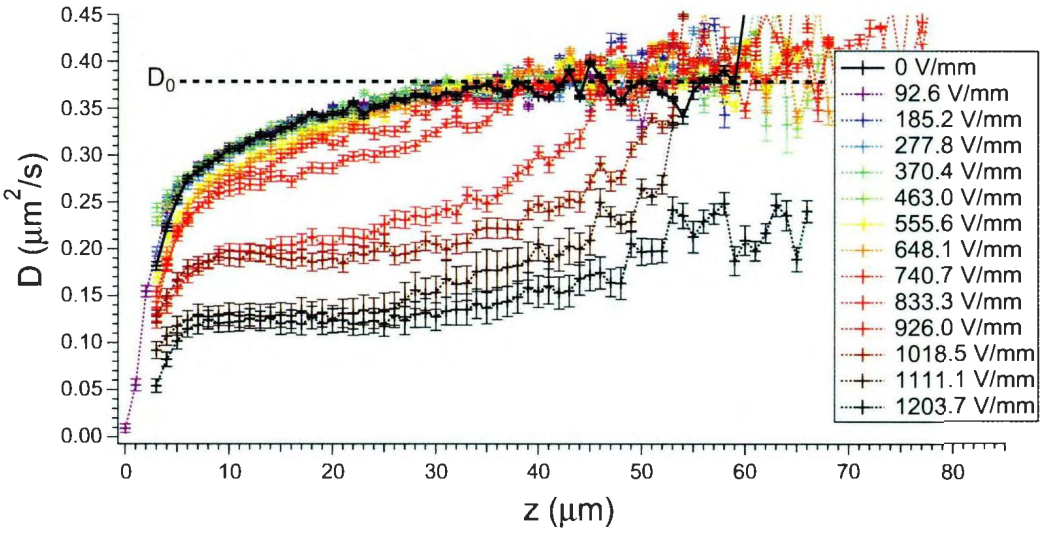

Figure 4.18: Diffusion as a function of z for a range of field strengths from $E = 0V/mm$ to $E = 1203.7V/mm$ of $2a = 1\mu m$ PMMA colloids in 60:40 decalin/TCE. The diffusion coefficient can be seen to change as a function of height due to effects of varying concentration as well as wall effects. Phase-like regions can be seen with varying electric field strengths. $D_0 = 0.38 \pm 0.01 \mu m^2/s$ is the bulk diffusion coefficient for this suspension. The gravitational length, l_g, in this system is $10.9\mu m$.

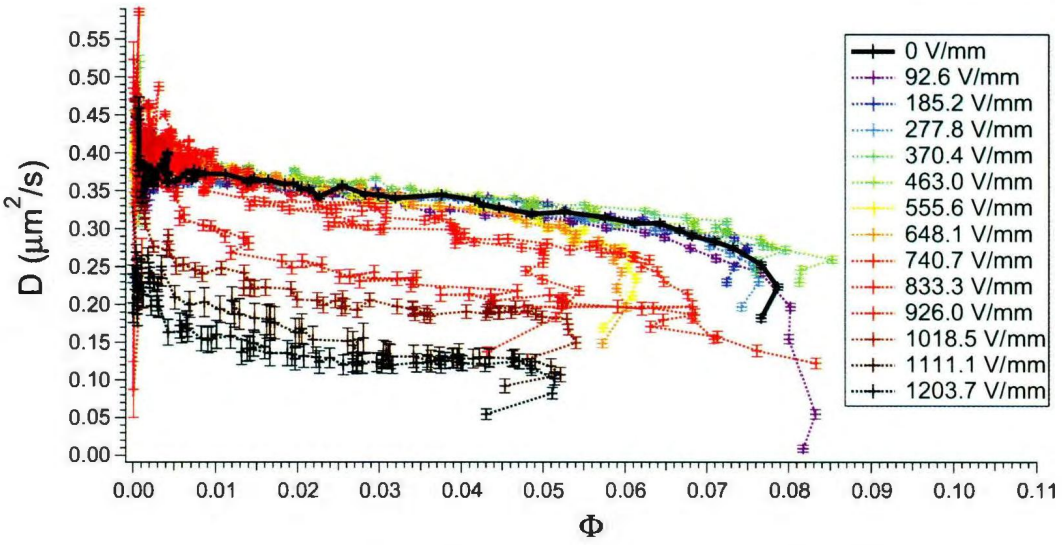

Figure 4.19: To view the data another way, the volume fraction can be obtained from sedimentation profiles of the same system by interpolating the profile and extracting the volume fraction at the height the diffusion data was taken. On this graph high volume fraction corresponds to low height and vice versa. The area over small changes in z but with large changes in Φ are accentuated here. Diffusion coefficient as a function of volume fraction for a range of field strengths from $E = 0V/mm$ to $E = 1203.7V/mm$ of $2a = 1\mu m$ PMMA colloids in 60:40 decalin/TCE.

and extending about seven particle diameters (or $7\mu m$). The second is a much more extended effect that arises from sphere-sphere hydrodynamic interactions. Wall proximity here plays an indirect role due to the particle density profile (figure 4.4). From the diffusion profiles (figure 4.18), it would appear this effect extends 40-50μm (4-5 gravitational lengths).

The results can be presented another way by looking at the diffusion coefficient as a function of the volume fraction, Φ, as seen in figure 4.19. In this graph high Φ corresponds to low z in the previous figure (shown in figure 4.4). Here we can see the distinction between the change in diffusion coefficient due to volume fraction and the change due to the rigid boundary even more clearly. At high Φ (for example, $\Phi = 0.06$ for $E = 555.6V/mm$, and $\Phi = 0.08$ for $E = 92.6V/mm$) we see that D increases for several points while Φ remains relatively unchanged. This change in D is related to the rigid boundary effect, demonstrated in section 4.2.1 [8]. We then see D increasing as Φ decreases as well. At low electric field strengths (i.e. $E < 800V/mm$) the diffusion coefficient as a function of height changes only a little from the $0V/mm$ profile. At higher field strengths ($E > 833.3V/mm$), corresponding to a dipolar strength $\Lambda = 1.028$ as will be seen in section 4.2.4, major deviations are seen at lower depths. However all except the highest $1203.7V/mm$ ($\Lambda = 2.15$) rise back to the bulk value as z increases. As can be seen from figure 4.6, $E = 833.3V/mm$ is characterized by the the onset of formation of small chain like structures. By plotting D against ϕ, we are clearly able to distinguish changes in D due to the proximity to a rigid boundary, as well as the changes in D caused by hydrodynamic interactions at high

ϕ in a sediment.

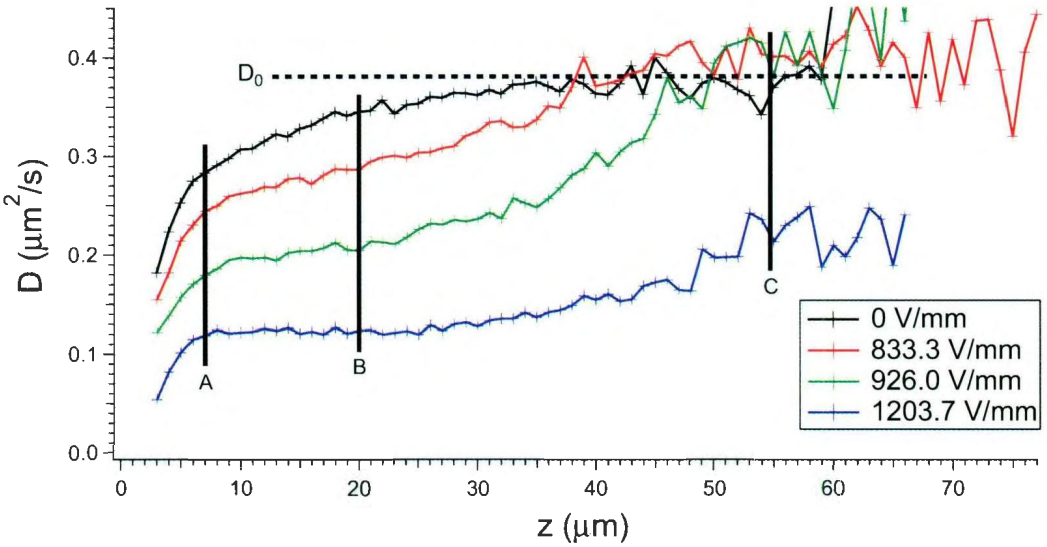

Figure 4.20: Three regions are highlighted for four selected field strengths, showing distinct phase-like behaviour in the diffusion as a function of z. $2a = 1\mu m$ PMMA colloids in 60:40 decalin/TCE.

Diffusion coefficient curves for the field strengths previously selected in section 4.1.1 are seen in figure 4.20. The zero field curve was selected as the reference point and $E = 833.3V/mm$ is where significant deviation from the zero field curve is noticeable. Low in the sediment (small z), the dynamics are much slower than the bulk value for $E = 926.0V/mm$ and $E = 1203.7V/mm$. High enough in the sediment, D returns to the bulk value for $E = 926.0V/mm$, but not for $E = 1203.7V/mm$. The three regions selected are shown in figure 4.20 as A, B, and C. Region A is low in the sediment, yet beyond the effect of the rigid boundary, region B is where the zero-field curve begins to experience bulk diffusion coefficients, and region C is is the extreme dilute region

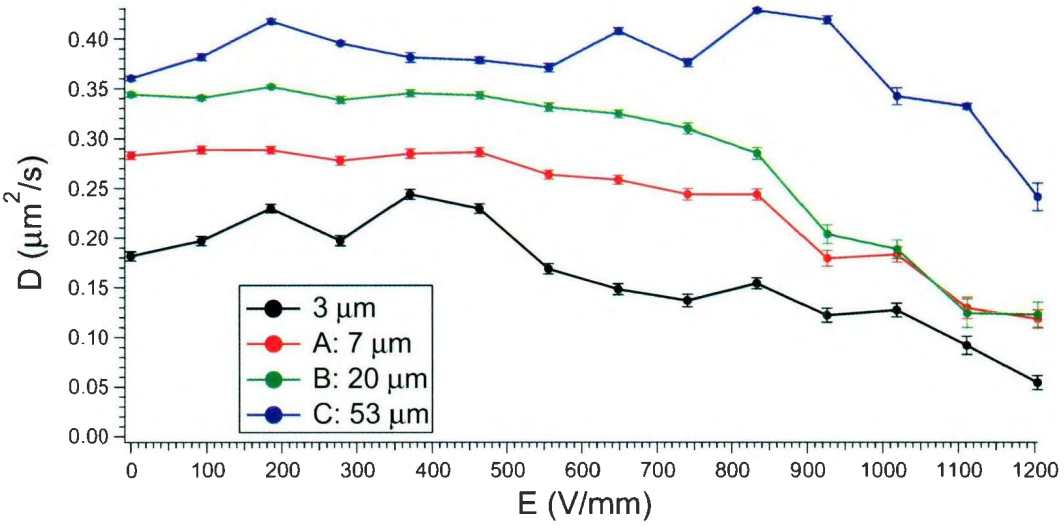

Figure 4.21: This shows how the diffusion changes as a function of the field strength in the selected regions. Diffusion as a function of electric field strength for regions A, B, and C for $2a = 1\mu m$ PMMA colloids in 60:40 decalin/TCE.

at the top of the sediment. To help quantify our results we also look at the diffusion as a function of field at these regions in figure 4.21 as well as images of the suspension in each region and cluster size distributions.

We first look at region A, $7\mu m$ into the sample. In figure 4.20 all four highlighted field strengths show significantly different diffusion coefficients, decreasing from $D = 0.28 \pm 0.01 \mu m^2/s$ to $0.12 \pm 0.01 \mu m^2/s$ in order of increasing field strength. Comparing these diffusion coefficients to what is observed in figure 4.22, we see that for the zero field the diffusion coefficient is smaller than the bulk value due to the higher VF close to the bottom of the sediment. At $E = 833.3 V/mm$ the VF near the bottom of the sediment is reduced due to the beginning of chain formation in the z direction (into the page). The reason we see particles forming clusters in the xy plane is due to the bonding of multiple chains from dipolar interactions. As described by Ning Li *et al*

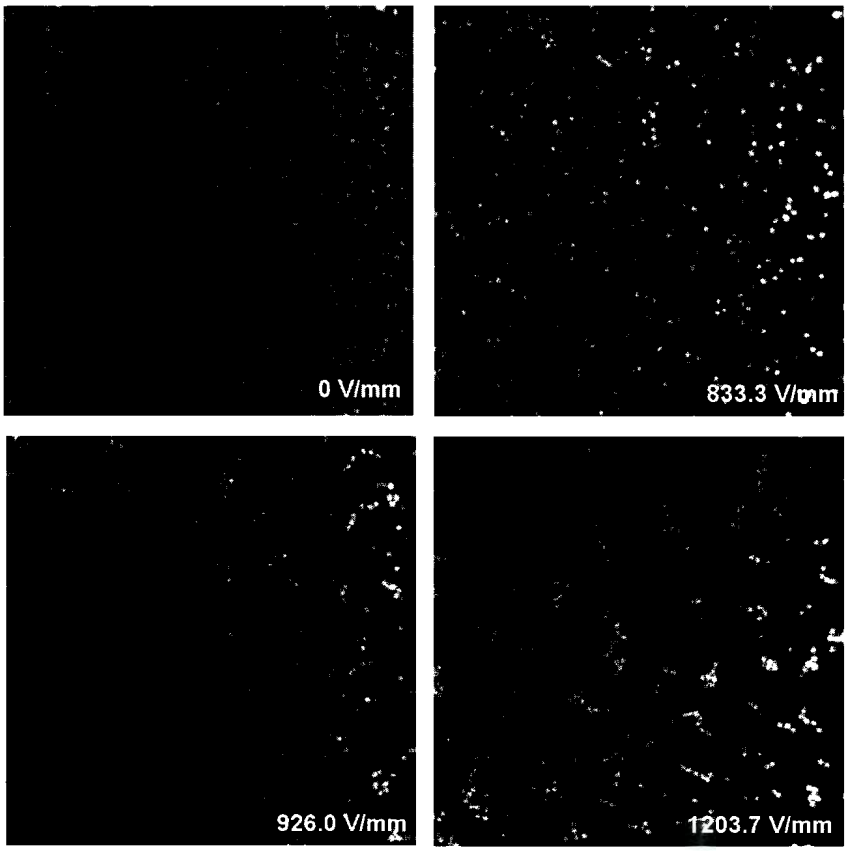

Figure 4.22: Images corresponding to the different field strengths at region A ($z = 7\mu m$) shown in figure 4.20. As the electric field increases, the particle concentration at the bottom decreases due to chain formation along the z direction. PMMA colloids ($2a = 1\mu m$) in 60:40 decalin/TCE.

and Ahmad Almudallal *et al* [15, 25, 36] two chains that are "staggered," i.e. their particle positions in z are not perfectly in phase, experience attractive interactions at small separations. As the field strength is increased to $926.0V/mm$ and $1203.7V/mm$ we see the local VF decrease further due to chain formation and stronger dipolar bonds between particles, leading to slower diffusion coefficients. The reduction in VF in this region is confirmed by referring to figure 4.4: the local VF decreases from 7.0%, to 5.3% in order of increasing field strength.

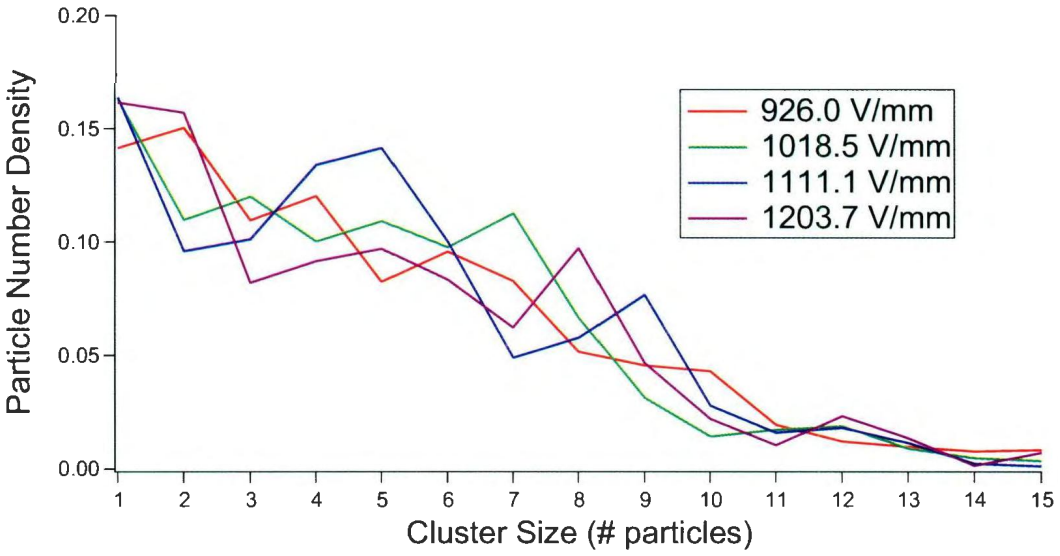

Figure 4.23: Normalized cluster analysis for region A ($z = 7\mu m$) with only high fields, $E \geq 926.0V/mm$, showing where chains have formed. Lower field strengths have been removed. $2a = 1\mu m$ PMMA colloids in 60:40 decalin/TCE.

Not only chain formation, but the formation of clusters of chains can be confirmed by looking at a cluster analysis of the sample, which is the normalized number of particles in a cluster of size N shown in figure 4.23. The cluster analysis at this

position in the sample has to be analysed carefully, as the high VF at this low position in the sediment leads the cluster analysis code to misinterpret an amorphous close packed sample as varying sizes of large clusters. The code checks distances between particle centers, and if they are within a set distance, $1.1 \times (2a)$, they are given a cluster id. This is done over an entire time-series. Thus this only works well at low VF. Due to this, invalid data is not shown. If the code were to take into account the dynamical information, this could be corrected, as particles not in a cluster would eventually diffuse apart from one another. Below $926.0V/mm$, the cluster analysis does not reliably report on field induced clusters. At these higher fields, there are significant numbers of particles in clusters of size between 2 and 9.

We now compare diffusion as a function of height seen in figure 4.20 at region B ($20\mu m$ into the sample) to images in figure 4.24. As we see from the graph, the zero field diffusion is approaching that of the bulk diffusion coefficient, at $D = 0.34 \pm 0.01\mu m^2/s$. Examining figure 4.24 we can see that at $20\mu m$ it does not look dilute, but is significantly more so than at $7\mu m$ as seen in both the images, figure 4.22, with a VF of 3.29%, from figure 4.5. The diffusion coefficient for the $E = 833.3V/mm$ field strength has increased from the value in region A to $D = 0.29 \pm 0.01\mu m^2/s$, yet is retarded due to the chain formation. In this case, $\Lambda \sim 1$ and particles are still able to diffuse loosely as well as in a cluster. We can see the evidence of this in the difference in the images in figure 4.22 and 4.24 for the $E = 833.3V/mm$ field strength, with the particle configuration changing and the VF decreasing to 4.7%. For the $E = 926V/mm$ and the $E = 1203V/mm$ field strengths the diffusion remains

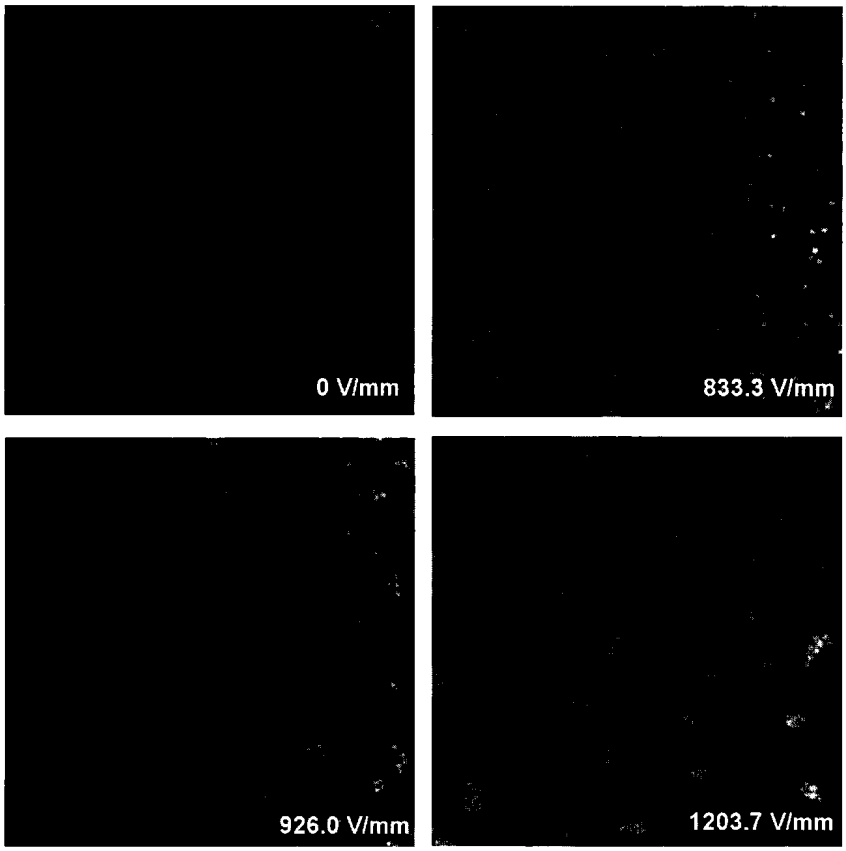

Figure 4.24: Images corresponding to the different field strengths at region B ($z = 20\mu m$) shown in figure 4.20. At this height for the different field strengths, the clustering of particles is of varying levels. The difference in the chain formation can be seen in the different diffusion coefficients. PMMA colloids ($2a = 1\mu m$) in 60:40 decalin/TCE.

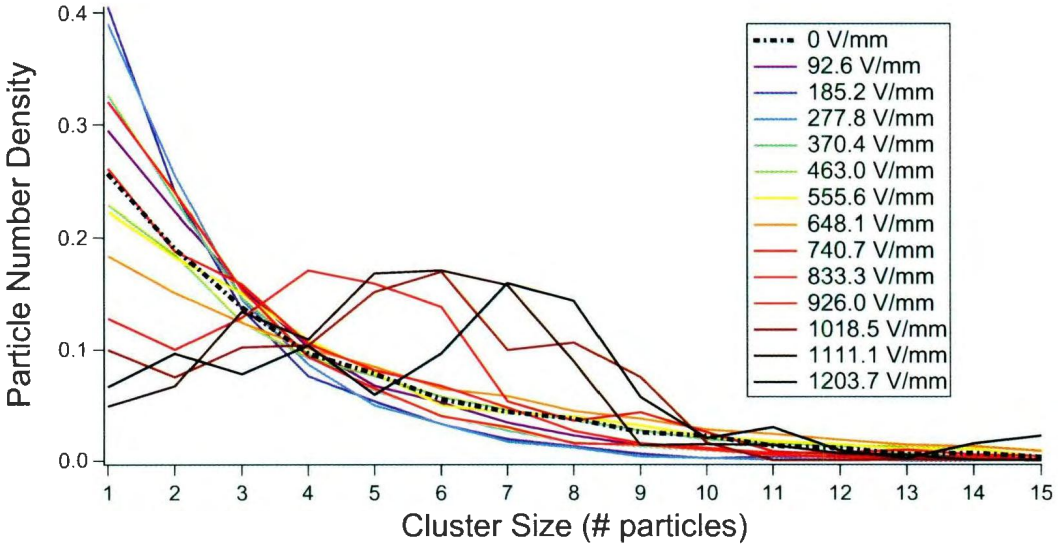

Figure 4.25: Normalized cluster analysis for region B ($z = 20\mu m$). A clear transition from single particles to larger induced clusters due to attractive chains can be shown to occur at $E = 926.0V/mm$. $2a = 1\mu m$ PMMA colloids in 60:40 decalin/TCE.

relatively unchanged at $20\mu m$ from the initial $7\mu m$ with values of $0.20 \pm 0.01\mu m^2/s$ and $0.12 \pm 0.01\mu m^2/s$ respectively. This is due to the fact that at these field strengths strong chains have formed that extend at least the depth of region B. Looking at the these field strengths in figure 4.24 and comparing to figure 4.22 (and figure 4.5) we can see that the configuration and VF appear to remain unchanged any significant amount at 4.5% and 3.6% respectively, a smaller decrease than the low field cases. We can see the improvement in the cluster analysis in this region in figure 4.25. Here we see that at low field ($E < 833.3V/mm$) there is a single-particle cluster peak, with some clusters of varying size found in uniform decreasing probability. The analysis works well for the low field examples, with larger clusters likely being due to freely diffusing particles that are within 1.1σ of each other. At the higher fields ($E > 833.3V/mm$) we see that the peak cluster size shifts from 4 at $E = 833.3V/mm$ ($\Lambda = 1.03$) to 8 at

$E = 1203.7V/mm$ ($\Lambda = 2.15$).

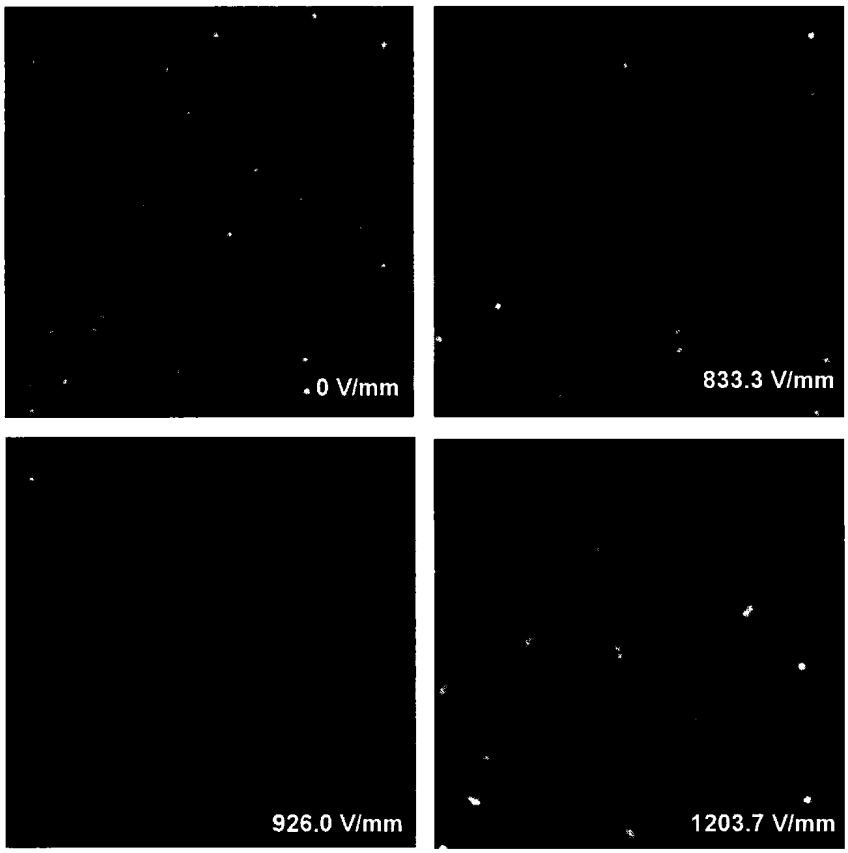

Figure 4.26: Images corresponding to the different field strengths at region C ($z = 55\mu m$) shown in figure 4.20. At this height the volume fraction is so low that the three lowest field strengths all resemble a gas phase, which is demonstrated by the diffusion coefficients approaching the zero-field value. While the highest field strength still shows particles clustering together, and also a still reduced diffusion coefficient. PMMA colloids ($2a = 1\mu m$) in 60:40 decalin/TCE.

We now look at the final region, region C as shown in figure 4.26. Here, $55\mu m$ into the sample, we see some interesting changes in the diffusion curves. The zero-field curve is still around its plateau value at $0.38 \pm 0.01\mu m^2/s$, while the $E = 833.3V/mm$ and the $E = 926.0V/mm$ curves have increased from their retarded values to the

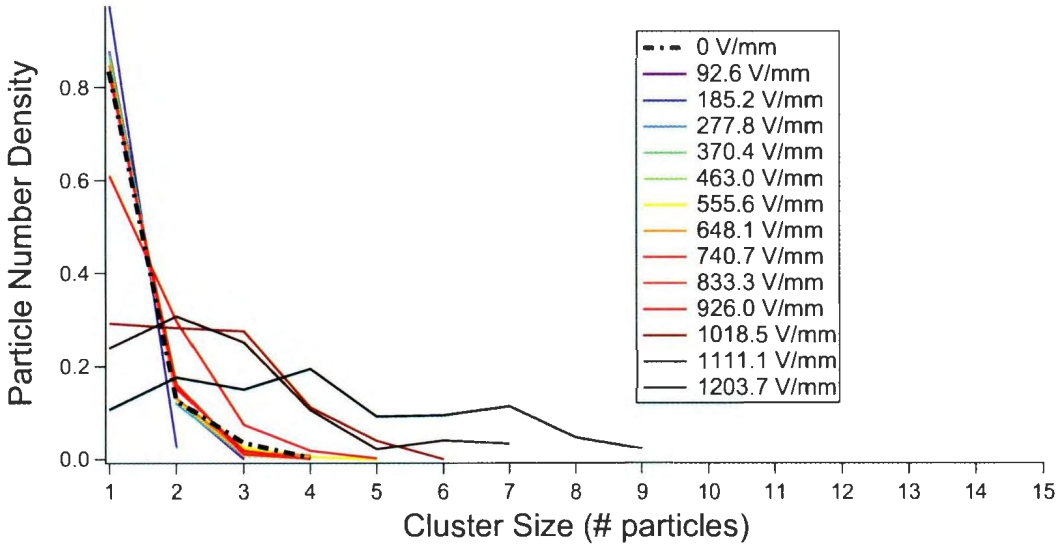

Figure 4.27: Normalized cluster analysis for $z = 40\mu m$ ($15\mu m$ below region C). A clear transition from single particles to larger induced clusters due to atractive chains can be shown to occur at $E = 1018.5V/mm$, a higher field strength than in region B. $2a = 1\mu m$ PMMA colloids in 60:40 decalin/TCE.

zero-field plateau values. When we look at figure 4.26, we see that the zero-field case is in the dilute regime, and comparing the $833.3V/mm$ and $926.0V/mm$ to the zero-field case we see that they both appear to be in the dilute regime as well and show no signs of large clusters. In the XZ profiles of figure 4.6 we see can see that chains only extend up to region C at fields of $E = 926.0V/mm$ and above. The diffusion curve for the $1203.7V/mm$ field strength ($\Lambda = 2.15$), still has a retarded value of $0.21 \pm 0.02\mu m^2/s$. We can see from figure 4.26 that the diffusion has increased due to decrease in cluster size. The VF is low enough to not have enough particles at that depth to create large clusters of chains, but we can still see the effects of strong chain formation in the particle pairs that are visible. Due to the very low volume fraction in region C, a cluster analysis couldn't be performed due to the lack of particles. And as one can see from figure 4.26, it is almost completely single particles in the XY

plane. However cluster analysis at an incremental height between $20\mu m$ and $55\mu m$ was done to show the trend of what was occurring. Cluster analysis was done at $z = 40\mu m$ in the sample, and the results are shown in figure 4.27. At $40\mu m$ into the sample we can see from figure 4.27 that for $E < 1018.5V/mm$ the graph is peaked around 1. At fields above $E = 1000V/mm$, there is a cluster peak at around 3 or 4 and a lower probability for single particles, those larger clusters are smaller than at $20\mu m$ where the probability is peaked around 6 or 7. This along with figure 4.6, shows as the height increases, and VF decreases, field effects only become important at $E \geq 926.0V/mm$ which corresponds to a dipolar strength of $\Lambda = 1.27$.

4.2.3 Diffusion in a thin sediment for $0.8\mu m$ diameter PMMA in 70:30 decalin/TCE

The same experimental process is repeated with a suspension of smaller PMMA particle with a diameter of $0.8\mu m$. In this case the solvent used was a mixture of decalin/TCE with a 70:30 ratio by volume. The suspension is again allowed to sediment to equilibrium and then time series are taken from the bottom of the sample to the end of the sediment in $0.8\mu m$ increments (one diameter spacing). AC electric fields of similar strengths are applied to the sample in the direction of gravity in the same manner as before. The resulting diffusion coefficients as a function of depth can be seen in figure 4.28. The result here is similar to the one for $1\mu m$ particles. The zero-field curve is our reference point and is retarded from a bulk diffusion coefficient at low depth due to effects due to a rigid boundary as well as inter-particle hydrodynamic interactions at higher volume fraction (these hydrodynamic interactions at

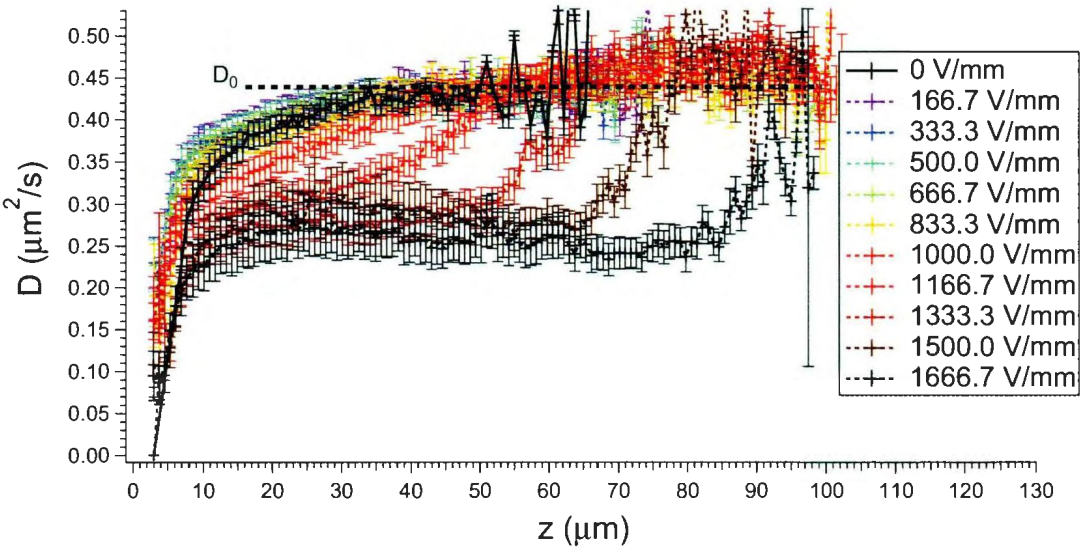

Figure 4.28: Diffusion as a function of z for a range of field strengths from $E = 0V/mm$ to $E = 1666.7V/mm$ of $0.8\mu m$ diameter PMMA colloids in 70:30 decalin/TCE. The diffusion coefficient can be seen to change as a function of height due to effects of varying concentration as well as wall effects.

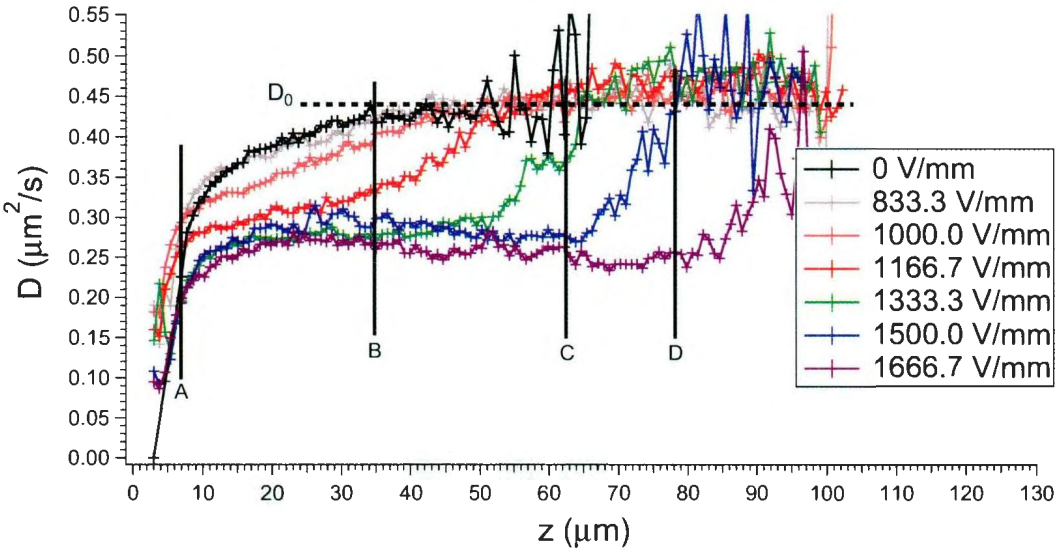

Figure 4.29: Diffusion coefficient as a function of z for seven specific field strengths $0.8\mu m$ diameter PMMA colloids in 70:30 decalin/TCE. Four regions are highlighted showing distinct phase-like behaviour.

zero field are quantified in section 4.2.4). However, high enough into the sample the $0V/mm$ curve plateaus out to the bulk diffusion coefficient of $0.44 \pm 0.01\mu m^2/s$ for the $0.8\mu m$ diameter spheres. We again see that at low field values the diffusion curve follows the same trend as the zero-field case, until around $1000.0V/mm$ and higher. In order to see this more clearly several curves are selected and four heights in the sediment are highlighted so that we may discuss each individually and compare them, seen in figure 4.29.

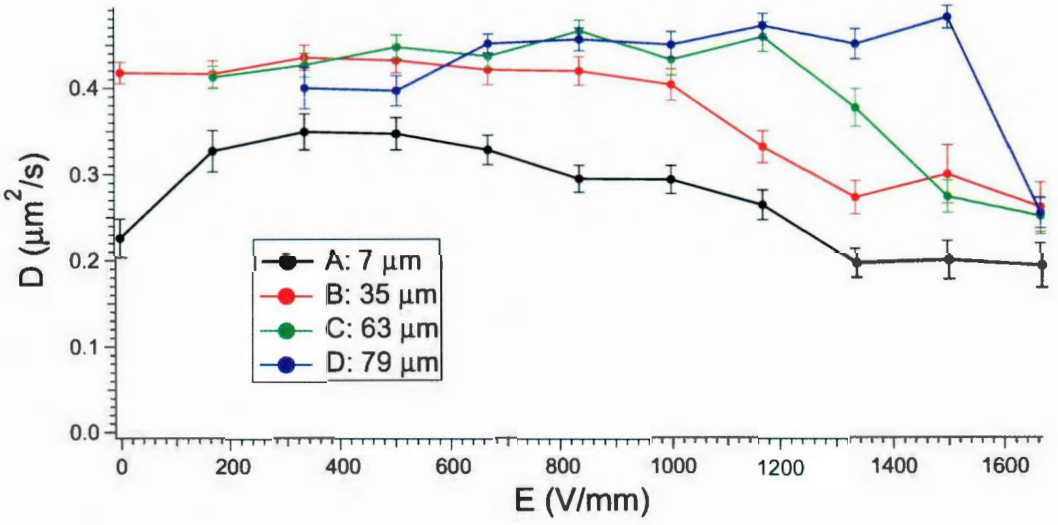

Figure 4.30: Diffusion as a function of of field strength for discussed regions for $0.8\mu m$ diameter PMMA colloids in 70:30 decalin/TCE.

In figure 4.29, we are once again looking at the change from single particle diffusion near the top of a sediment to the diffusion of colloidal particles within clusters and chains in a sediment. The zero-field curve is again used as our standard reference for colloids diffusing in a sediment. The $833.3V/mm$ curve is shown to compare to the

$1\mu m$ case, as that is the field strength where the deviation from single particle diffusion began. However the induced dipolar effect is lessened in a smaller particle, and as shown in figure 4.29 at this field strength the diffusion coefficient of the smaller $0.8\mu m$ diameter particles remains the same as the zero-field reference curve and we don't see significant retardation until $1000.0V/mm$. As in the $1\mu m$ spheres, this corresponds to a dipolar strength of $\Lambda \sim 1$ (see table 4.2). We show four more field strengths beyond this and highlight four depths at regions of interest. The diffusion coefficient as a function of the field strength along these regions can be seen in figure 4.30.

We first look at region A as shown in figure 4.29, $7\mu m$ into the sample. At this height, field strengths in the $E = 0V/mm$ to $E = 1166.7V/mm$ have diffusion coefficients of $D = 0.27 \pm 0.03\mu^2/s$, while for the higher field strengths the diffusion coefficients are again close to each other but with a lower average value, $D = 0.20 \pm 0.03\mu^2/s$. In figure 4.31 we can see that in the lower three field strengths the VF is decreasing as field increases, consistent with our finding in figure 4.9 that the VF at this height decreased from 7.1% at $0V/mm$ to 5.8% at $1000.0V/mm$.

In figure 4.32, the cluster analysis for field strengths above $E = 1333.3V/mm$ are shown. At lower fields, and low in the sample (i.e. at high VF) the cluster analysis has to be discarded because of the natural proximity between particles. For low field examples, the high VF amorphous fluid confuses the cluster analysis code into thinking these are larger structures, when in fact there are many independent particles. We can see the change at $1166.7V/mm$ and higher where clusters are

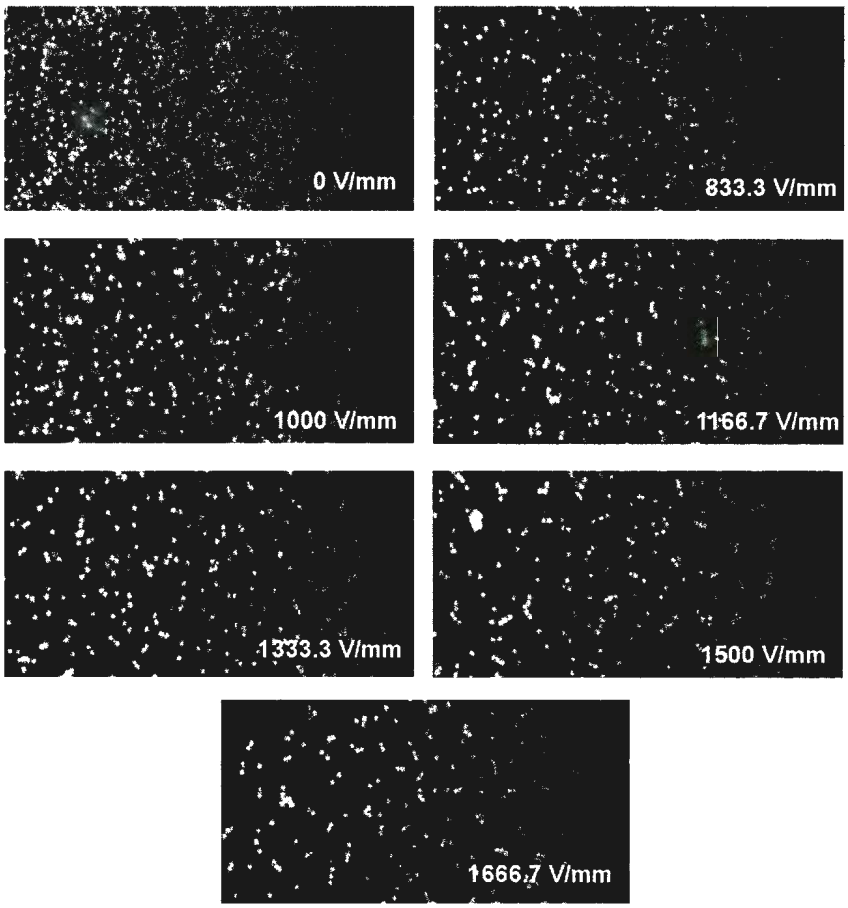

Figure 4.31: Images of $0.8\mu m$ diameter PMMA colloids in 70:30 decalin/TCE corresponding to the different field strengths at region A ($z = 7\mu m$) shown in Fig. 4.29. As the electric field increases, particle concentration at the bottom decreases due to chain formation along the z direction.

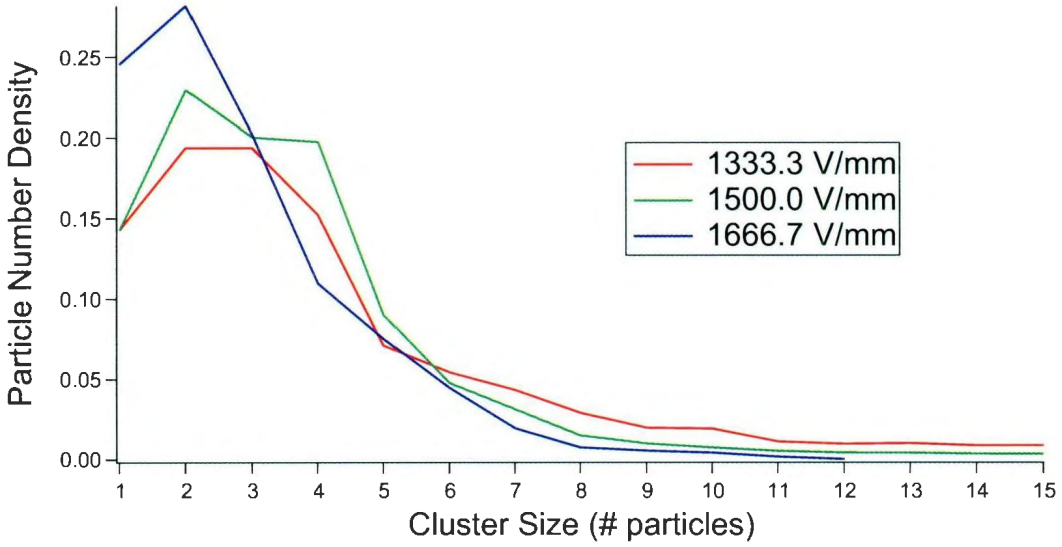

Figure 4.32: Normalized cluster analysis of $0.8\mu m$ diameter PMMA colloids in 70:30 decalin/TCE at region A ($z = 7\mu m$)

forming, as confirmed by figure 4.31, with probability peaked around the size of 2 to 4 particle size.

In region B, $35\mu m$ into the sample, we saw in figure 4.29 that that the three highest field strengths of $1333.3V/mm$, $1500.0V/mm$, and $1666.7V/mm$ have all reached a plateau value for the diffusion coefficient between 0.26 and $0.30\mu m^2/s$, significantly lower than the zero-field value of $0.44 \pm 0.01\mu m^2/s$, which is at the bulk value. As seen in the XZ profiles of figure 4.11, chain formation is first evident at fields above $E = 1000V/mm$. In figure 4.33 we see clusters of chains first occuring at $E = 1333.3V/mm$. This is consistent with the cluster distributions (figure 4.34) having a peak at 2 for $E > 1166V/mm$. At $E > 1333.3V/mm$, the clusters are smaller than in region A. Clustering in the $0.8\mu m$ colloids is qualitatively quite different from the $1\mu m$ diameter PMMA colloids. With the $0.8\mu m$ particles the chains formed do

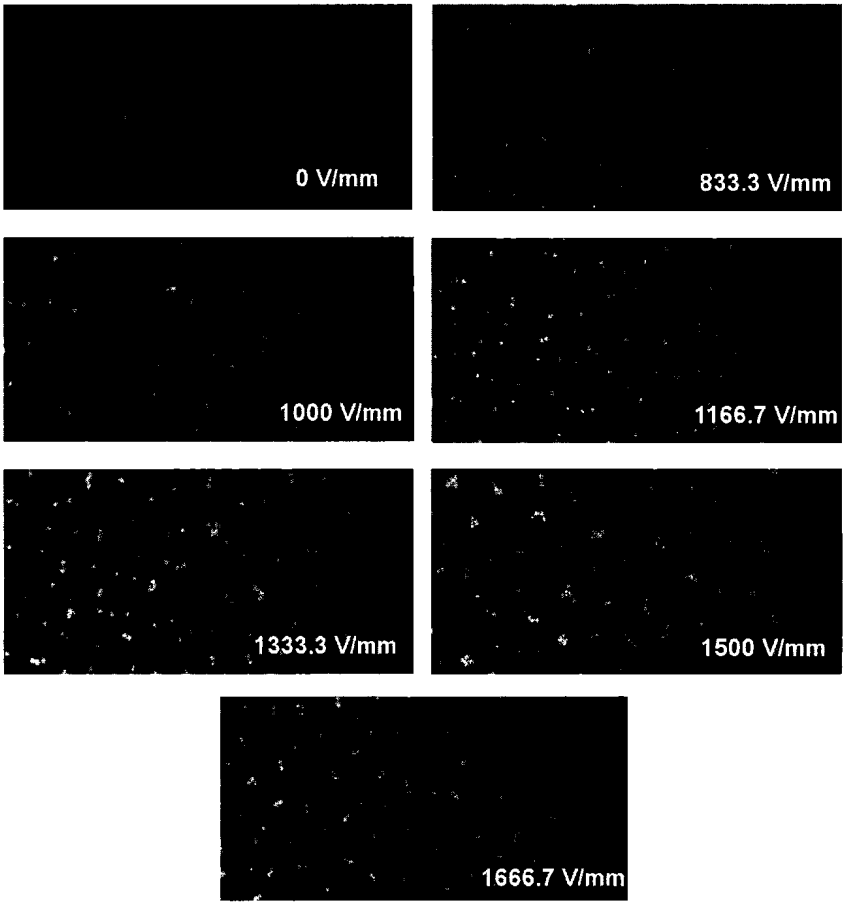

Figure 4.33: Images of $0.8\mu m$ diameter PMMA colloids in 70:30 decalin/TCE corresponding to the different field strengths at region B ($z = 35\mu m$) shown in Fig. 4.29. While the images at fields of $1000V/mm$ and $1333.3V/mm$ do not clearly demonstrate chain formation like the higher fields, the dipolar effect in these systems can be shown to be significant by looking at the diffusion coefficients in this region in Fig. 4.29.

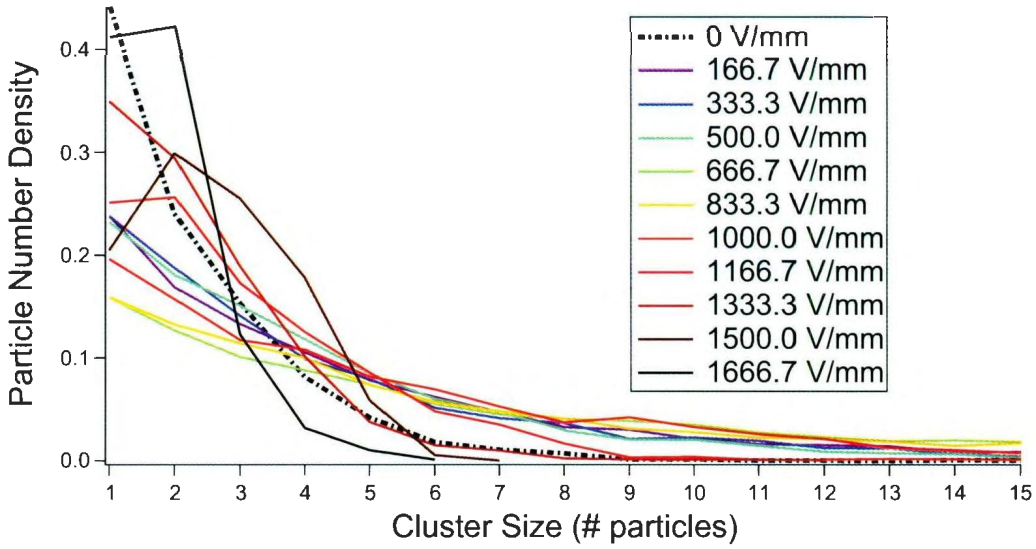

Figure 4.34: Normalized cluster analysis of $0.8\mu m$ diameter PMMA colloids in 70:30 decalin/TCE near region B ($z = 30\mu m$)

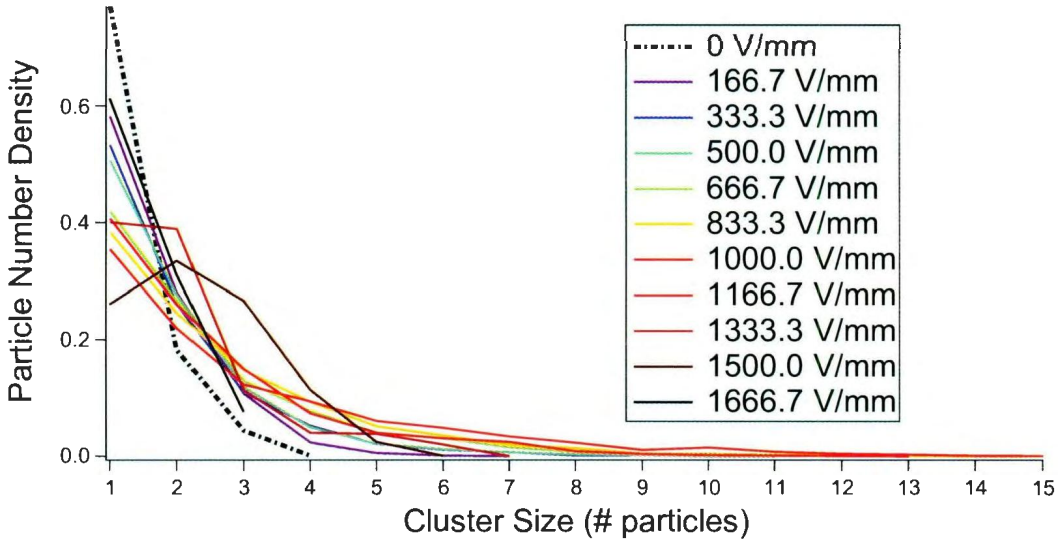

Figure 4.35: Normalized cluster analysis of $0.8\mu m$ diameter PMMA colloids in 70:30 decalin/TCE near region C ($z = 40\mu m$)

not cluster as much as the larger particles, resulting in tall thin chains. This may be seen by comparing the position of the cluster peak in region B in figure 4.34 at $E = 1500.0V/mm$ to that for region B at $E = 1203.7V/mm$ for $1\mu m$ diameter colloids ($\Lambda \sim 2.1$ in both cases). In the latter case, there were too few particles to carry out a cluster analysis. The more extended nature of the chains in the small-particle system can also be seen by direct comparison of the XZ profiles in figures 4.6 and 4.11.

Referring back to figure 4.29 we see that at region C, $63\mu m$ into the sample, the $E = 1333.3V/mm$ field strength curve has increased from the lower plateau level, up to the zero-field diffusion coefficient, indicating that this field strength is too low to extend chains to this depth. It is difficult to confirm this by looking at figure 4.36 as there is no dramatic change in 2-dimensional clusters. However it can be confirmed using the xz profiles in figure 4.11. This indicates we can use the diffusion curves to determine the extent of chain formation. Cluster analysis graphs are not done at these higher regions, and looking at figures 4.36 and 4.37 it is clear why. Due to the lack of these chains clustering together in large numbers, the chains are much smaller than the $1\mu m$ particle case, and at these heights consist of single particles along the z-direction. Referring to figures 4.36 and 4.11, we see that at $E = 1500V/mm$ and $E = 1666.7V/mm$, we still see strong chains at this height, which is supported by their lower plateau diffusion coefficient in figure 4.29.

At $79\mu m$ we see, seen in figure 4.37, a similar thing happen to the $1500V/mm$ diffusion curve as we saw happen to the $1333.3V/mm$ curve at $63\mu m$. Around the

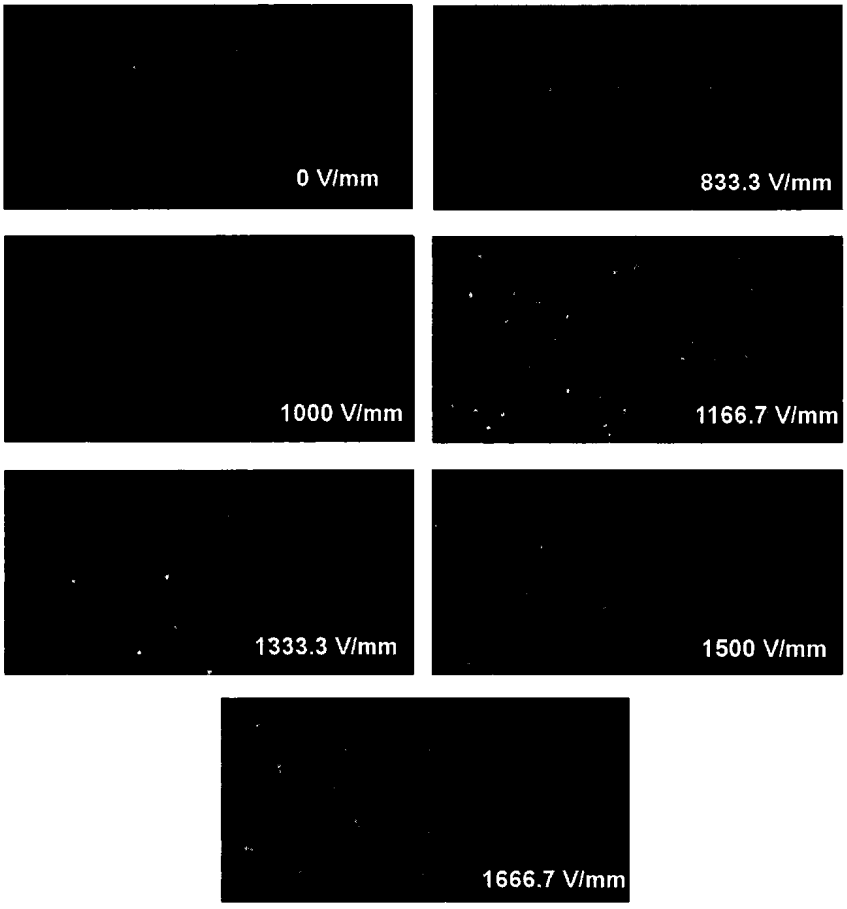

Figure 4.36: Images of $0.8\mu m$ diameter PMMA colloids in 70:30 decalin/TCE corresponding to the different field strengths at region C ($z = 63\mu m$) shown in Fig. 4.29. Looking at the diffusion coefficient data, at this height D for all field strengths have returned to the zero-field value at this height except for $1500V/mm$ and $1666.7V/mm$. The higher intensity in these respective images is due to the fluorescence from the particles above and below in the same chain.

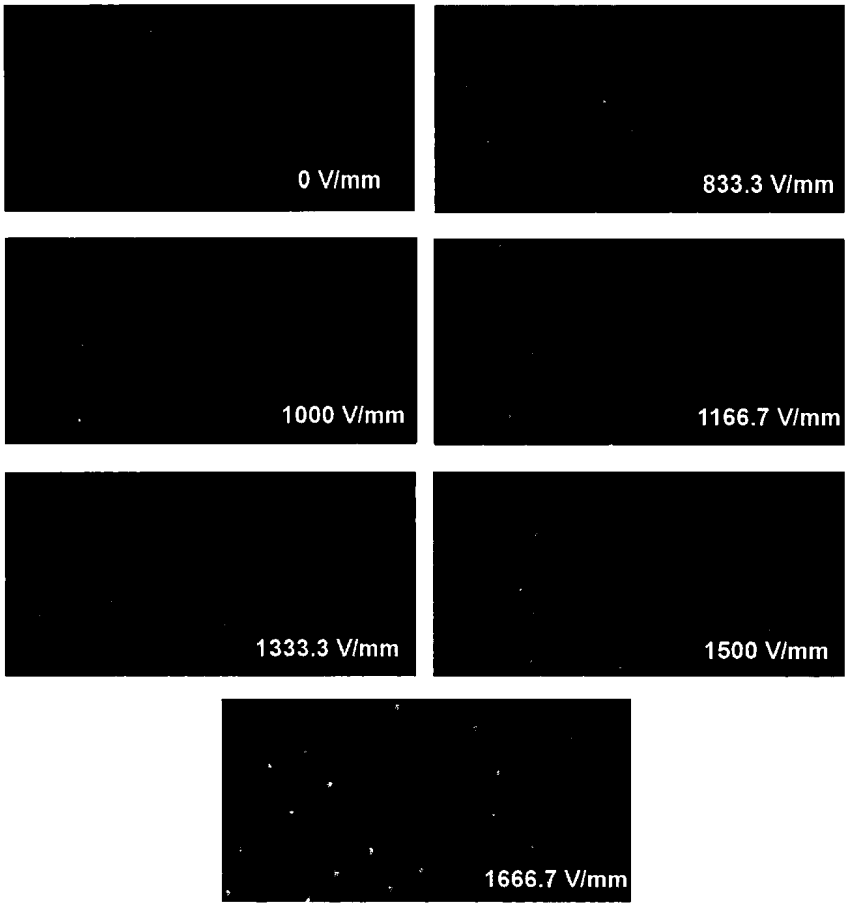

Figure 4.37: Images of $0.8\mu m$ diameter PMMA colloids in 70:30 decalin/TCE corresponding to the different field strengths at region D ($z = 79\mu m$) shown in Fig. 4.29. Looking at the diffusion coefficient data, at this height D for all field strengths have returned to the zero-field value at this height except for the highest, $1666.7V/mm$. The higher intensity in these respective images is due to the fluorescence from the particles above and below in the same chain.

same height that the $1333.3V/mm$ curve reached the zero-field diffusion plateau value, the $1500V/mm$ diffusion began to increase from it's retarded diffusion plateau. Now at $79\mu m$, the $1500V/mm$ diffusion has reached the zero-field diffusion plateau value, leaving only the $1666.7V/mm$ with a retarded diffusion due to chain formation, still unaffected by the extreme height in the sample. Looking at figure 4.37, again it is not very clear at what field strengths chain formation is occurring and what field strengths it is not. To help clarify this we again look at figure 4.11, and we see that at $79\mu m$, all cases show dispersed particles, except for the $1666.7V/mm$ field strength, where chain formation persists.

4.2.4 Comparison of the diffusion coefficients and cluster analysis for both monodisperse experiments

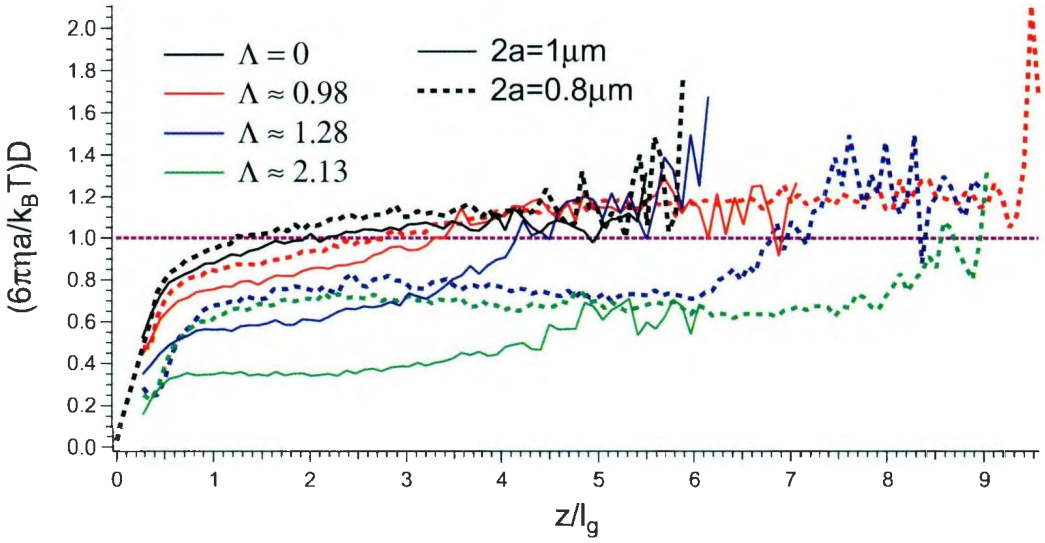

Figure 4.38: Scaled diffusion coefficients multiplied by $6\pi\eta a/(k_BT)$ for both monodisperse experiments ($2a = 1\mu m$ PMMA in 60:40 decalin/TCE and $2a = 0.8\mu m$ PMMA in 70:30 decalin/TCE) plotted against the dimensionless z/l_g.

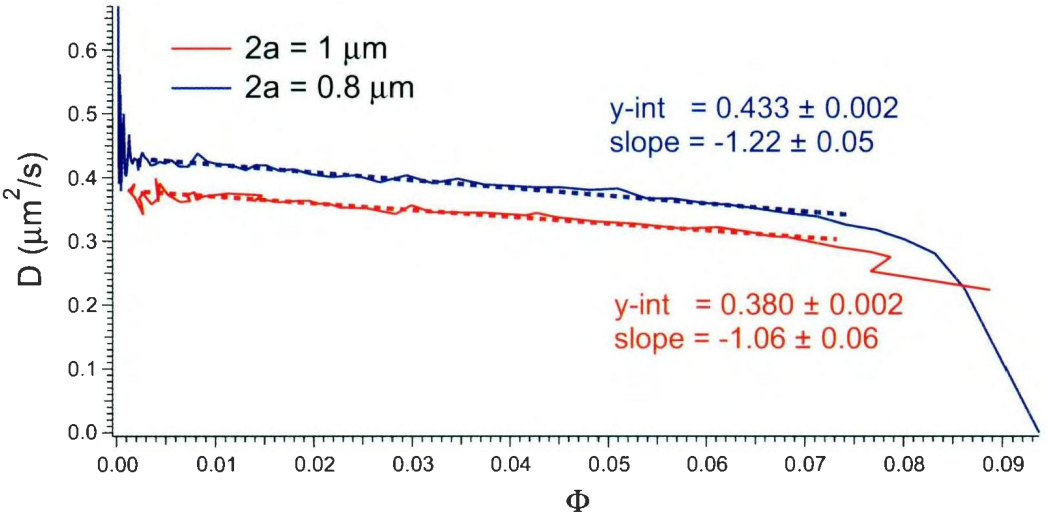

Figure 4.39: Diffusion coefficients as a function of local volume fraction, ϕ, for both monodisperse experiments ($2a = 1\mu m$ PMMA in 60:40 decalin/TCE and $2a = 0.8\mu m$ PMMA in 70:30 decalin/TCE) for zero-field. By fitting the section of the curve beyond 7σ (boundary effect as discussed by Carbajal-Tinoco *et al* [8]) we can extract the short-time self-diffusion coefficient and the hydrodynamic factor.

In order to get a more precise value for our bulk diffusion value we also plot D vs. ϕ for both monodisperse zero-field experiments, in figure 4.39. We fit the section where diffusion coefficients decrease linearly as a function of VF to a line in order to extract the bulk diffusion value D_0 as well as the hydrodynamic factor K_s^S as shown in equation 3.3. The bulk diffusion values are given by the y-intercept of these fits, and agree with our earlier stated values. From this we also calculate $K_s^S = 2.8 \pm 0.1$ for $2a = 1\mu m$ PMMA particles, and $K_s^S = 2.8 \pm 0.1$ for $2a = 0.8$ PMMA particles. This is somewhat larger than the value of 1.7-1.8 expected from hydrodynamic theories [32, 33].

In order to examine the deviation in the diffusion coefficients from the predicted

Stokes-Einstein value we plot $D \times \frac{6\pi\eta a}{k_B T}$ vs. z/l_g and so that we can compare our two experiments. In the bulk, this value must equal 1, if the viscosities are correct. This comparison can be seen in figure 4.38.

As can be seen, the plateau value at large height is larger than 1, but all the curves do indeed have a common plateau value, within errors. The discrepancy is likely due to small differences in viscosity measurements (prepared separately).

The profiles of the scaled diffusion coefficients for the two particle-diameter suspensions are close to each other for $\Lambda = 0$, and deviate significantly for $\Lambda = 1$ and 2. This signals the regime where thermal energy, dipolar energy, and gravitational energy are all simultaneously important.

We make an important observation that likely is indicative of the goodness of the dipolar approximation in this system. In both systems, the field first begins to affect the profiles noticeably near $\Lambda = 1$ (when the dipolar energy equals $k_B T$), and the profiles have a low secondary plateau when $\Lambda = 2$ (when the dipolar energy equals $2 \times k_B T$). This contrasts with the observations of Ning Li *et al* where field effects were observed at a calculated $\Lambda \approx 3$ [15], and suggests that the point dipolar approximation is a better approximation in the current system due to observing the onset of chains at $\Lambda \sim 1$.

The transitions from single particle to chain formation at the different dipolar

strengths, Λ (calculated using equation 2.11 and shown in table 4.2), show similar behaviour at similar dipolar strength. However the highest dipolar strength, $\Lambda \approx 2.13$, have entirely different plateau values. This occurs due to the formation of larger clusters perpendicular to the field. The diffusion is not only being restricted by the particle diffusing with a chain, but also the chain is a larger cluster made up of multiple particle chains. Yet at $z/l_g \sim 5$ the diffusion coefficient for this curve agrees with the plateau for the other high field cases. This large clustering can be confirmed by looking at the cluster analysis for these dipolar strengths for both experiments in figure 4.40. It can be seen that the cluster size for the $2a = 1\mu m$ PMMA colloids in 60:40 decalin/TCE experiment is generally larger than the smaller particle experiment. This rise in the $D \times a$ value at $z/l_g \sim 5$ corresponds to region C in this experiment, and as can be confirmed by figure 4.26 the clustering at this region is almost non-existent, consisting of single particles with some doublets.

Comparing two systems of different particle size with similar gravitational length, l_g, at similar dipolar strength, Λ, is the best way to get an accurate comparison. However, this does not account for the difference in the ratio of dipolar energy to gravitational energy,

$$\frac{\Lambda}{mga/k_BT} = \Lambda \cdot \frac{l_g}{a},$$

which are off only by 20% in the two systems, but are not the same. The larger this ratio is, less of a role is played by gravitational energy. Thus for smaller particles, gravity is less important, which is what we see in our results. The difference in clustering is nevertheless surprising, because $\Lambda \frac{l_g}{a} > 20$ implies that the gravitational

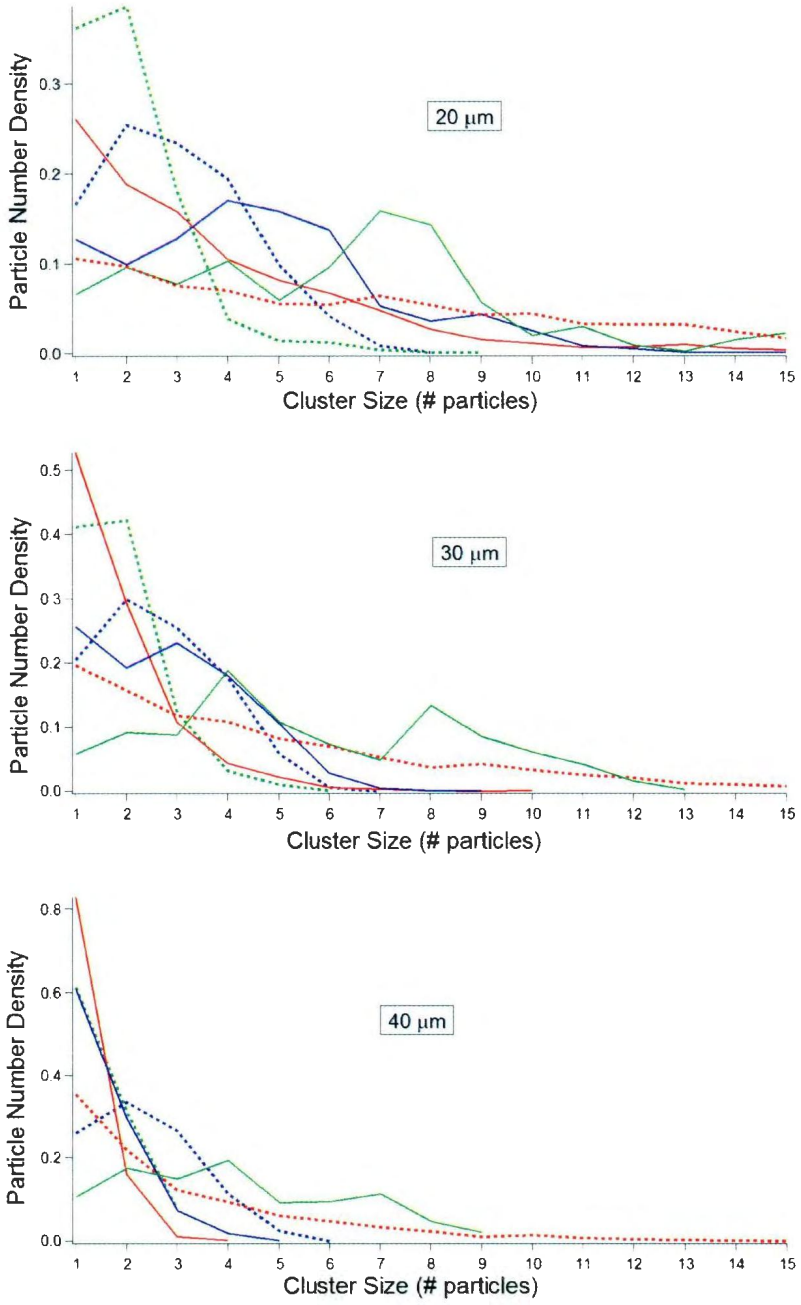

Figure 4.40: We show the cluster analysis for the two different monodisperse systems at similar dipolar strengths to show that the larger particle forms larger cluster sizes. Cluster analysis at three positions in the sediment for $2a = 1\mu m$ PMMA colloids in 60:40 decalin/TCE and $2a = 0.8\mu m$ PMMA colloids in 70:30 decalin/TCE at similar dipolar strengths, Λ

energy is very weak, but nevertheless the effect is measurable.

4.3 Sedimentation equilibrium and dynamics in a bidisperse colloidal suspension

Now that each of these particle sizes has been looked at individually, the final phase of this project was to look at the effects of sedimentation and dipolar interactions in a binary suspension. The two particles are mixed in even quantities (volume based) in the same 70:30 mixture of decalin and TCE as was done in the $0.8\mu m$ singular case. Although this will greatly reduce the extent of the $1\mu m$ particles sediment, it is necessary due to the same issues with the $0.8\mu m$ case above. The overall VF is 2% as before, with 1% of each particle size. The same experimental procedure was performed except twice; once for each particle size in different fluorescence channels. Each electric field strength was applied, then the necessary experiments were completed for each particle, and this was repeated for each field strength. However, due to poor image quality in the images of the larger particle caused by fluorescence from the other channel bleeding through, most data from the $1\mu m$ particles was unusable. Thus this section will focus on the results obtained from the $0.8\mu m$ particles.

First we again wish to analyse the overall structure of the sediment, and compare our low field EOS with hard-spheres. Here we've started with a peak-to-peak electric field of $E = 240V/mm$. The zero-field case was discarded due to spurious data

E (V/mm) $2a = 1\mu m$	Λ	E for $2a = 0.8\mu m$ (V/mm)	Λ
92.6	0.01270	166.7	0.02626
185.2	0.05080	333.3	0.1050
277.8	0.1143	500.0	0.2363
370.4	0.2032	666.7	0.4201
463.0	0.3175	833.3	0.6563
555.6	0.4572	1000.0	0.9452
648.1	0.6221	1166.7	1.287
740.7	0.8126	1333.3	1.680
833.3	1.028	1500.0	2.127
926.0	1.270	1666.7	2.626
1018.5	1.53646	-	-
1111.1	1.829	-	-
1203.7	2.146	-	-

Table 4.2: Lambda parameter for each experiment calculated from the corresponding electric field strength. In order to calculate Λ, we use dielectric constants from Table 4.1, and equation 2.11.

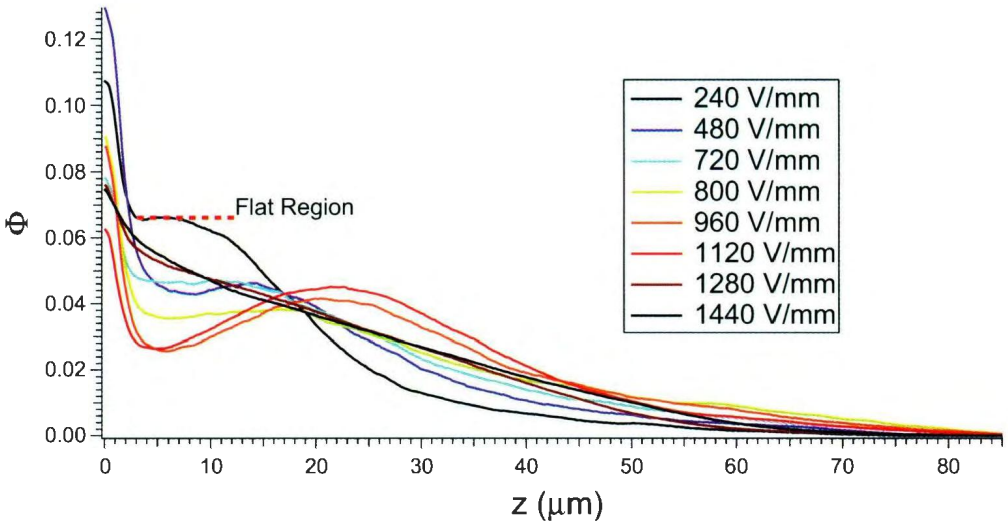

Figure 4.41: Bidisperse suspension. Intensity sedimentation profiles for a range of field strengths from $E = 240V/mm$ to $E = 1440V/mm$ for $0.8\mu m$ diameter PMMA colloids in 70:30 decalin/TCE

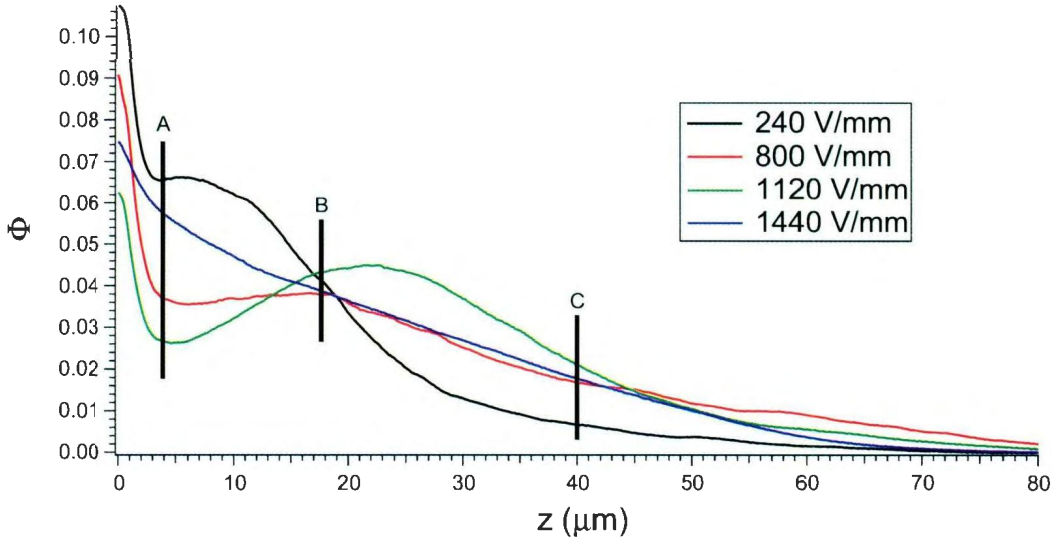

Figure 4.42: Bidisperse suspension. Intensity sedimentation profiles for four selected field strengths for $0.8\mu m$ diameter PMMA colloids in 70:30 decalin/TCE

caused by over saturated images, but as shown above in previous experiments, the $E = 240V/mm$ strength should be low enough to yield approximately the same dynamic and structural results as the zero-field case. At low field and close to the bottom of the sediment, there is a flat section (highlighted in figure 4.41) where the VF remains relatively constant in z. This was previously studied by myself and colleagues (Ning Li *et al* [25]). However that experiment used a monodisperse system. This could arise from the bidispersity of the suspension, but further study is needed. To see the main deviation noted here from our previous two single particle cases, we look at four field strengths selected in figure 4.42. At region A we see that as the field increases, the VF is decreasing. This is expected behaviour, however for $E = 800V/mm$ and $E = 1120V/mm$ the VF then increases again around region B. At high enough fields this effect is neutralized. The $1\mu m$ particles only extend approximately $20\mu m$ into the sample, so by looking at these profiles in figure 4.41, as well as checking the images in figure 4.48, we can confirm that this behaviour in figure 4.42 is physical, and that it is most likely caused by the $1\mu m$ particles forming chains and clusters, reducing the free volume, and depleting the region of the smaller particle. Once the field is high enough ($E = 1440V/mm$), the dipolar attraction of the particles is strong enough to neutralize this effect and the smaller particles join the chains along the extent of the sediment. This causes the sedimentation profile to return to an expected shape. Looking at the EOS of this system in figure 4.43 we can see that for below $\phi = 0.06$ the $240V/mm$ low field case shows excellent agreement with the CS EOS, very similar to our monodisperse cases above. However this is not a true EOS. Without proper qualitative information about the sedimentation of the $1\mu m$ particles we cannot calculate true osmotic pressure. In order to calculate Π properly,

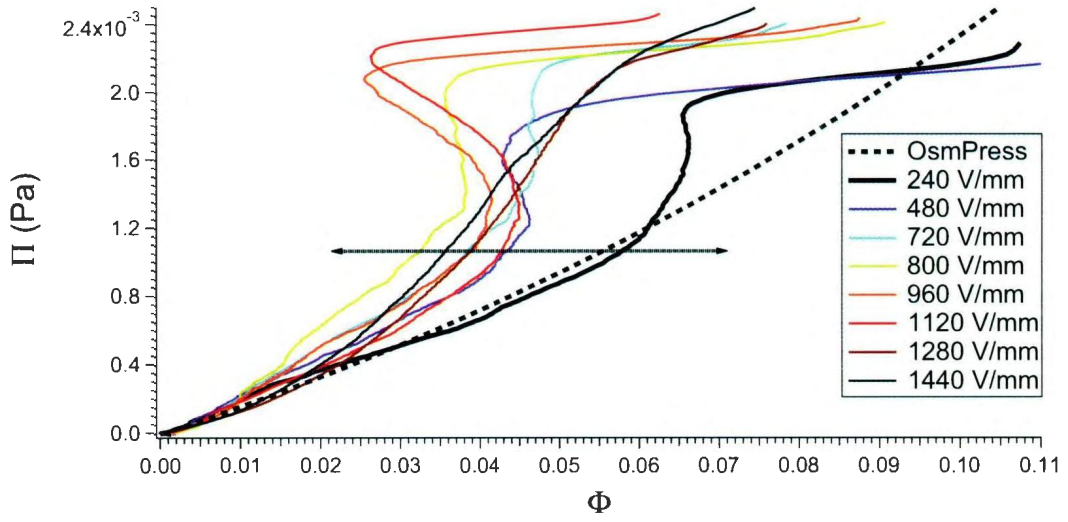

Figure 4.43: Apparent equations of state for a range of field strengths from $E = 240V/mm$ to $E = 1440V/mm$ for $0.8\mu m$ diameter PMMA colloids in 70:30 decalin/TCE, calculated from the intensity sedimentation profiles

we would need information about all the particles above the region of interest, not just a single particle. So we see that below $\phi = 0.06$ our $0.8\mu m$ particles EOS does match the hard-sphere EOS. This indicates that the concentration of $1\mu m$ particles is negligible at the height corresponding to this VF. However the deviation above this VF is significantly more in this example. The horizontal line seen in figure 4.43 denotes the osmotic pressure above which a single-species osmotic pressure is not meaningful, due to the presence of the larger particles low in the sediment. Again as the field strength is increased we see the deviation from hard-sphere behaviour.

Comparing figure 4.44 to the corresponding ones for the monodisperse suspensions (figures 4.6 and 4.11) we see that the clusters seem much larger than the $0.8\mu m$ suspension and somewhat larger than the $1\mu m$ suspension. We will revisit this issue by looking at lateral (XY) images and corresponding cluster size distributions.

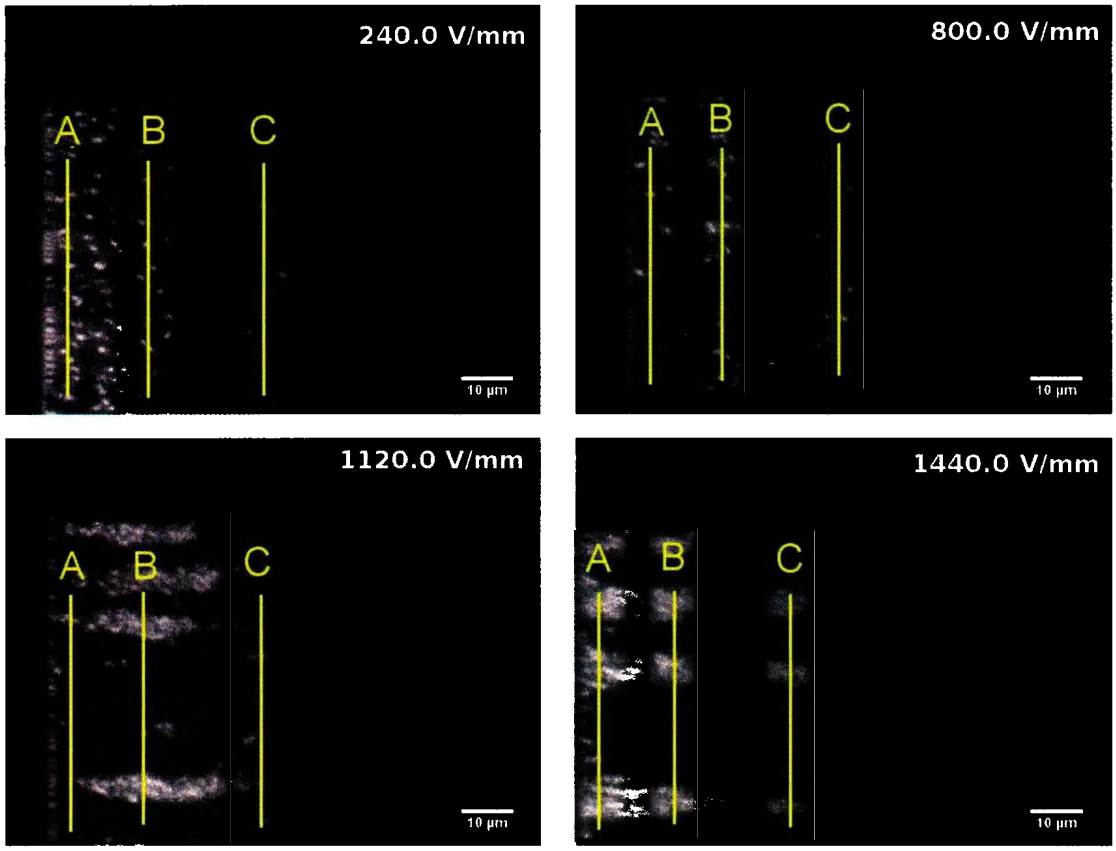

Figure 4.44: XZ transposed images of the sediment of $0.8\mu m$ PMMA colloidal sediments in 70:30 decalin/TCE at selected field strengths for a bidisperse system (gravity to the left, and z increasing to the right).

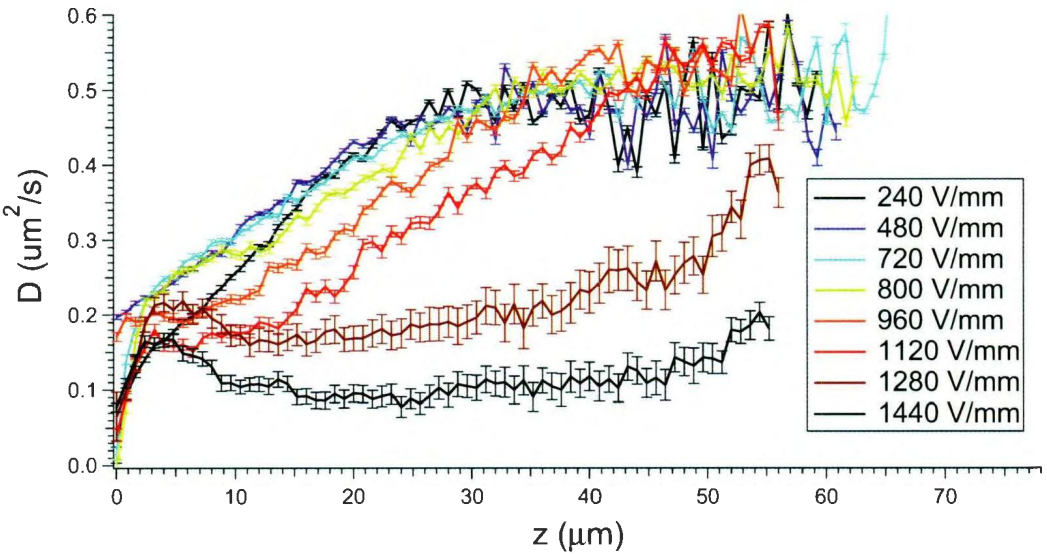

Figure 4.45: Bidisperse suspension. Diffusion coefficient as a function of z for a range of field strengths from $E = 240V/mm$ to $E = 1440V/mm$ of $0.8\mu m$ diameter PMMA colloids in 70:30 decalin/TCE. The diffusion coefficient can be seen to change not only as a function of height due to effects of varying concentration as well as wall effects, but different phase-like regions due to dipolar interaction can be seen in with varying electric field strengths along z.

The diffusion coefficients as a function of height for varying electric field strengths are shown in figure 4.45. Again we see that the diffusion coefficient increases from the bottom of the sample (region A in figure 4.46) where it is retarded due to hydrodynamic effects, both from the rigid wall as well as the interparticle interactions at higher VF, up to the bulk diffusion coefficient high in the sample (region C in figure 4.46). The bulk diffusion coefficient here is approximately $0.50 \pm 0.02\mu m^2/s$. This is higher than the bulk value for monodisperse $0.8\mu m$ in the same solvent of $D = 0.44 \pm 0.01\mu m^2/s$. As in the case of the monodisperse suspensions, the most likely cause of this discrepancy is the solvent viscosity. The viscosity could be decreased either due to a higher experimental temperature, or due to an inadvertently

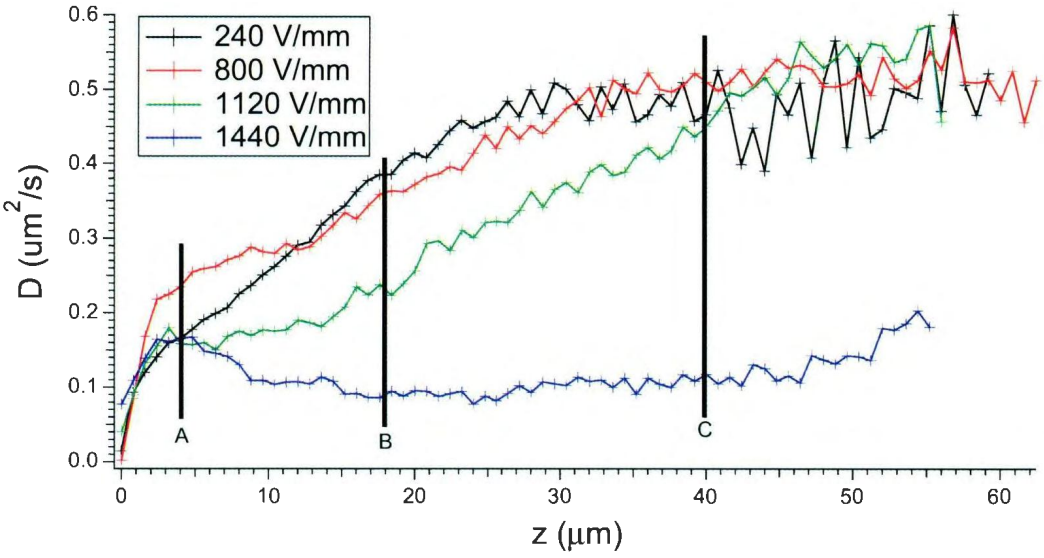

Figure 4.46: Bidisperse suspension. Diffusion coefficient as a function of z for four field strengths of $0.8\mu m$ diameter PMMA colloids in 70:30 decalin/TCE. Three regions are highlighted showing distinct phase-like behaviour.

different solvent mixture composition. While this affects the bare values of the diffusion coefficients, it will have no qualitative effect on the phenomena observed.

We select specific field strengths to highlight the behaviour seen in figure 4.46. The $E = 240V/mm$ curve was selected as the low field reference, the $E = 800V/mm$ is where deviation from low field behaviour begins to occur (as with the monodisperse $0.8\mu m$ suspension), $E = 1120V/mm$ shows a transition between low and high field, and $E = 1440V/mm$ as our highest field strength. Looking at this plot, there appear to be two significant deviations in behaviour from the previous single $0.8\mu m$ particle case. Firstly, in the binary suspension the increase in the diffusion coefficient between 5 and $25\mu m$ is almost linear, in contrast with the shoulder-like curves in the monodisperse suspensions seen in figures 4.18 and 4.28. This is likely an effect of

bidispersity related to the reduced local volume fraction in region A (see figure 4.42).

The other notable effect is the shape of the highest field ($E = 1440V/mm$) curve. Unlike the previous two cases for the highest field strength that increased to a plateau, in the binary experiment there is a non-monotonic behaviour (an initial peak near $z = 4\mu m$, followed by a decrease, then an increase at large z). As before three regions in the sample were picked in the diffusion coefficient curves (figure 4.46) as well as the sedimentation profiles (figure 4.42) for more detailed analysis.

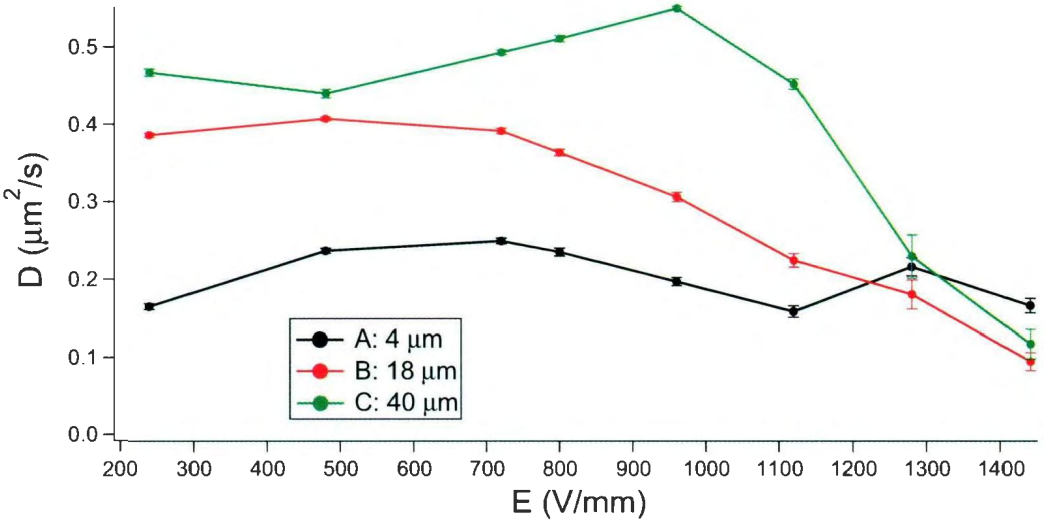

Figure 4.47: Diffusion as a function of electric field strength for selected regions

We first look at region A. $4\mu m$ into the sample. This is still within seven particle diameters of the substrate where Carbajal-Tinoco *et al* observed restricted diffusion near a rigid wall [8]. Each of the selected field strengths can be seen in this region in figure 4.48. The local VF of the smaller spheres decreases from 6.6% to 2.7% as the

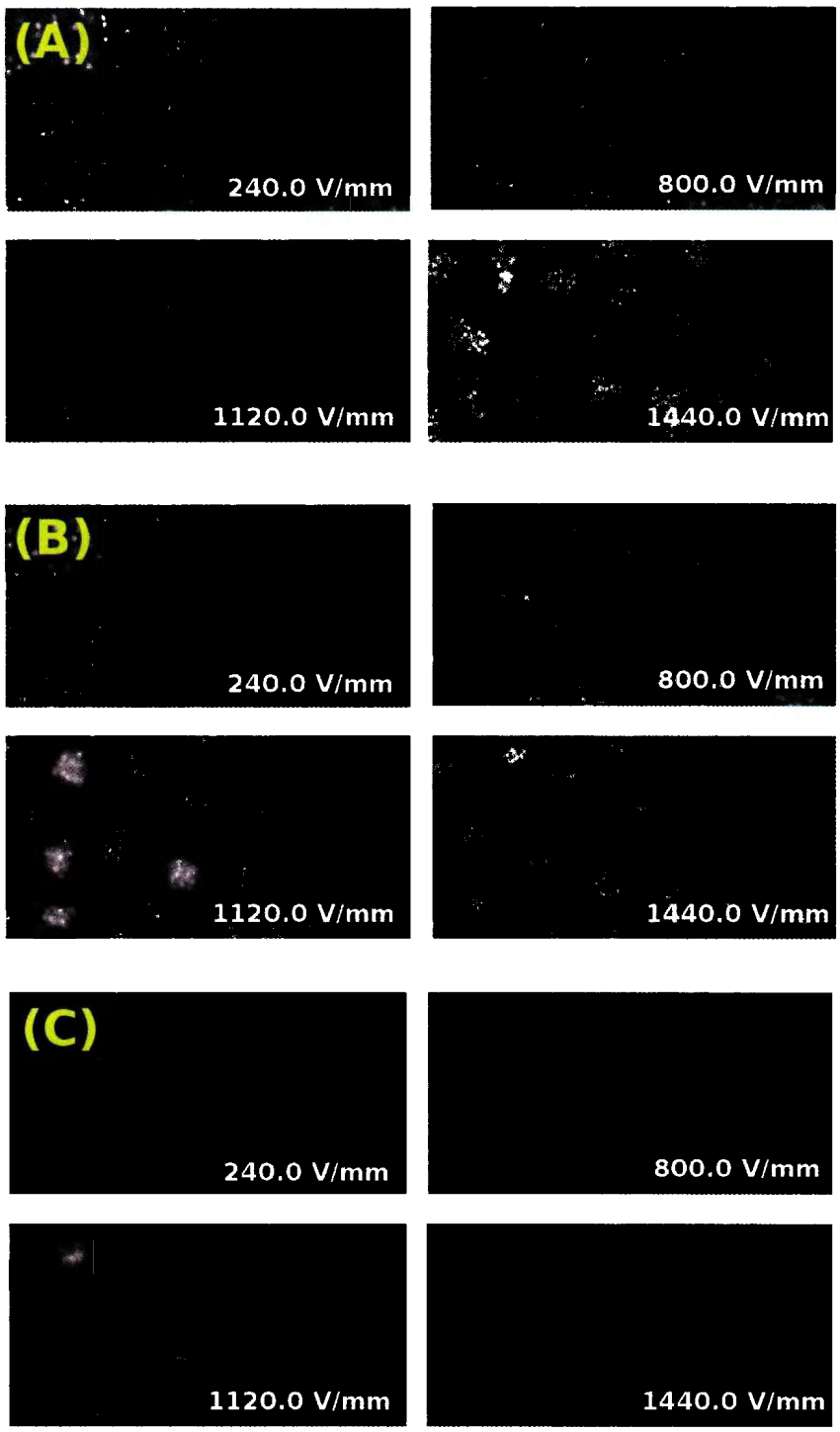

Figure 4.48: Image of $0.8\mu m$ PMMA in a binary suspension corresponding to the different field strengths at region A ($4\mu m$), B ($18\mu m$), and C ($40\mu m$) shown in Fig. 4.46.

field increases. Looking at the small particle diffusion coefficient as a function of the field strength for region A (figure 4.47) there is an initial increase due to a decrease in VF. At small z, the large particles effectively crowd out the small particles due to their smaller gravitational length. However, it decreases again once chains begin to form at $E = 1120V/mm$, with diffusion coefficients of $0.17 \pm 0.01\mu m^2/s$, $0.24 \pm 0.01\mu m^2/s$, and $0.16 \pm 0.01\mu m^2/s$ in order of increasing field strength.

For $E = 1440V/mm$, the highest field strength, something curious is observed: The local VF and diffusion coefficient have increased to 5.7% and $0.17 \pm 0.01\mu m^2/s$ respectively. This increase in VF likely occurs due to the strength of the dipolar interaction causing chains to form with the larger particles over the extent of the sample, reversing the depletion of small particles near the rigid boundary. The diffusion here is higher due to the large number of isolated particles contributing to the diffusion calculation, as seen in figure 4.48. Looking at the cluster analysis near this region ($z = 7\mu m$) in figure 4.49 we can see that the chains in the binary suspension form clusters with a peak at a size of 7 to 10 particles, while in the monodisperse cases (figures 4.23 and 4.32) they are lower. Remarkably, this is in spite of the fact that we are undercounting by roughly a factor of 2 because we only image the smaller spheres. As described in section 2.2.2 dipolar chains will form clusters in the plane perpendicular to the direction of the field if the chains are "staggered". We believe the larger clusters formed in this experiment are caused by the polydispersity of having two different particle diameters. Due to this, the probability of having staggered chains is much greater, causing larger clustering perpendicular to gravity.

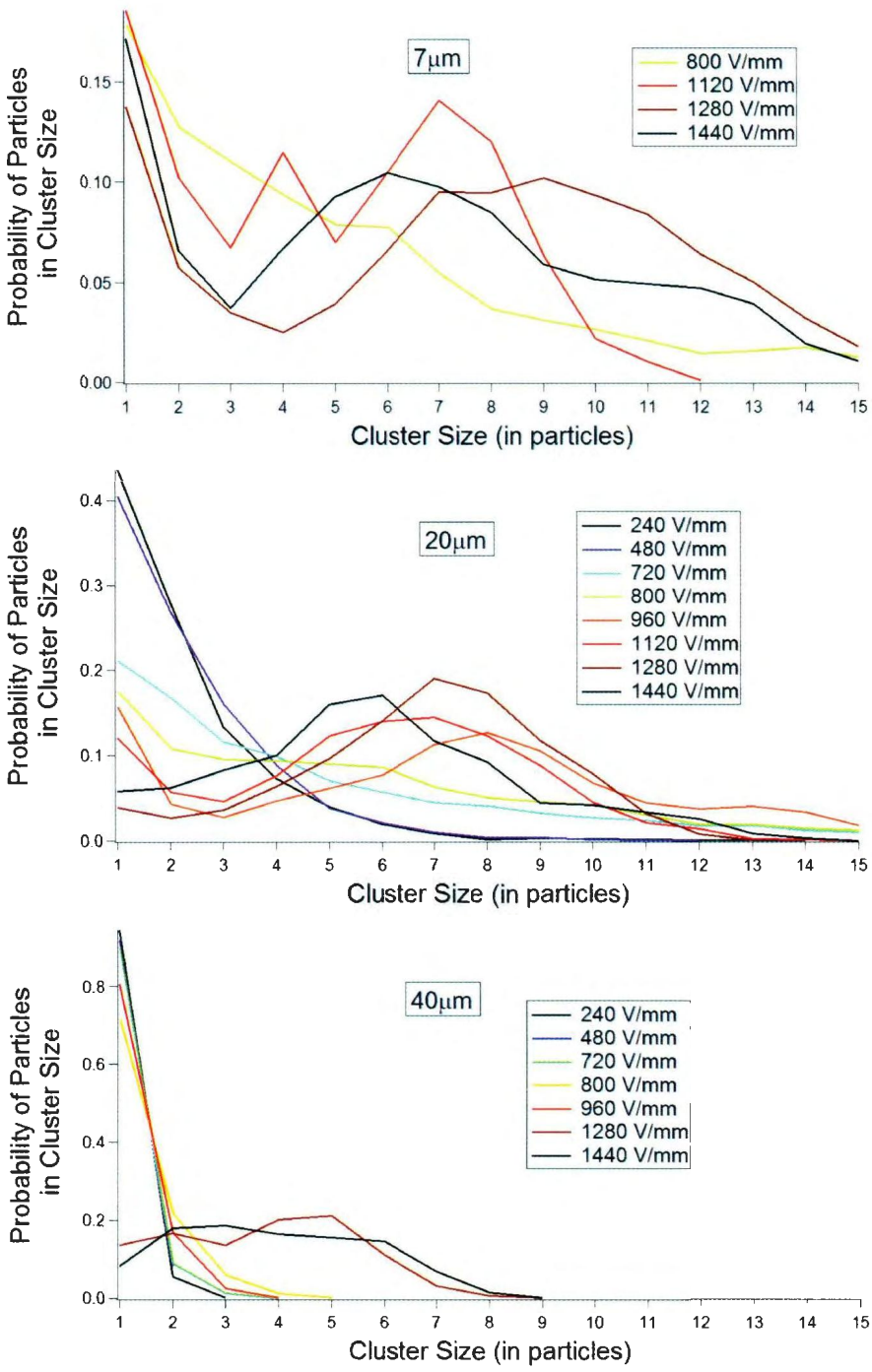

Figure 4.49: Cluster analysis of $0.8\mu m$ particles at $7\mu m$, $20\mu m$, and $40\mu m$ (near regions A, B, and C)into the sample for a bidisperse system

Next we look at region B, at $z = 18\mu m$. This is a transition region in the diffusion plots between a dense fluid and the dilute gas-like region. Here low field curves are increasing toward the bulk value, and the highest field strength, $E = 1440V/mm$ has plateaued at $D = 0.09 \pm 0.01\mu m^2/s$. The lower fields have diffusion coefficients of $0.39 \pm 0.01\mu m^2/s$, $0.36 \pm 0.01\mu m^2/s$, and $0.24 \pm 0.01\mu m^2/s$ in order of increasing field. The VF at this height in the sample is similar for all field strengths, $\phi \approx 4\%$.

In figure 4.48, we see that while strong clusters have not formed at $800V/mm$, some structure is beginning to occur. This coincides with a decrease in diffusion coefficient (figure 4.47). At higher fields chains and large clusters have formed. Comparing the $1120V/mm$ field strength, with region A, we see in figure 4.42 that the VF has actually increased from its lower value. This effect has not been seen in either of the single particle cases. The highest field strength ($E = 1440V/mm$) has a retarded diffusion coefficient due to the chain formation. The diffusion in region B at this field strength has decreased from its region A value of $D = 0.17 \pm 0.01\mu m^2/s$ (figure 4.47). This "bump" in the diffusion curves at high field is not observed in the monodisperse experiments. Large clusters are seen at this field strength for regions A and B (figure 4.48).

In region C, we see that for $E = 240V/mm$ and $E = 800V/mm$ have both reached the plateau value for the diffusion coefficient of $D_0 = 0.50 \pm 0.02\mu m^2/s$. The $E = 1120V/mm$ is approaching this value with $D = 0.45 \pm 0.01\mu m^2/s$. As expected both $E = 240V/mm$ and $E = 800V/mm$ appear to be in the dilute regime here, while

the $1120V/mm$ does still show some clustering and chain formation, as observed in figure 4.48. However there are many smaller clusters and individual particles. At the highest field strength of $E = 1440V/mm$, only strong chain clusters which extend the the entire sediment are seen. This can be confirmed by looking at the cluster analysis at this height in figure 4.49 as well as looking at the vertical slice of the sediment as before as seen in figure 4.44.

Chapter 5

Conclusions

5.1 Summary of Results

In this work we used laser scanning confocal microscopy to attempt to show agreement between a system of PMMA colloids in a decalin/TCE solvent and a system of hard-spheres. Similar work has been done in the past showing an agreement in the equation of state of a bulk suspension of colloids, to that of hard-spheres [3, 7, 24]. However deviation from this agreement has been shown in the past within a thin sediment of a microscopy sample [25,37]. We have been able to show that this system of PMMA in a decalin/TCE solvent shows excellent agreement with the Carnahan-Starling equation of state of hard-spheres for two different particle sizes, in a thin sediment. This suggests that this would be an appropriate system for studies of hard-sphere crystal nucleation. This is because this system is also density and refractive-index matchable.

AC electric fields were also applied to this system. The AC electric field alters

the inter-particle interaction and the corresponding equation of state changes. A typical approximation is the hard-sphere plus point dipolar approximation. Due to our spheres being shown to be hard-sphere-like, simulations can be carried out to compare the equations of state of our system, hard-sphere colloids in an external field, to a hard-sphere-plus-dipolar system. We can use experiment to explore the validity of the dipolar model. In principle, similar phenomena should be seen for different particle sizes provided that the dipolar strength, Λ, is the same. In the presence of gravity, the situation is more complicated. At zero and low fields, scaling the height with the gravitational height appears to collapse the data from the two particle sizes. Another remarkable observation is that the electric field effects become apparent at around $\Lambda = 1$. This is another indication that this system might be uniquely close to a true hard-sphere-plus-dipolar model system.

At higher dipolar strengths, the ratio of the dipolar to gravitational energy is larger for the smaller particles, so gravitational settling is less evident for small particles. It should be noted that the particle sizes used for these microscopy experiments are at the limit where particle tracking is feasible in concentrated suspensions. For larger particles (more typically used in colloidal confocal microscopy experiments) these gravitational effects would be even more pronounced.

Finally we studied the effects of a field on the structure of a bidisperse colloidal system. Here we find that the main result we see is the size of the chain clusters is much larger than both of the monodisperse experiments. The polydispersity of the

particle size increases the probability of neighbouring chains being staggered causing them to cluster. The relevance of this is that this can be used to create particle size mixtures in order to change the macro electrorheological properties of these suspensions. Further studies of the dependency of particle size ratios, as well as the volume fraction ratios of the different particles, is needed to determine the dependency of these on the cluster size and the electrorheological properties.

Bibliography

[1] R. A. L. Jones. *Soft Condensed Matter.* Oxford University Press, 2009.

[2] A. Yethiraj. Tunable colloids: control of colloidal phase transitions with tunable interactions. *Soft Matter*, 3:1099–1115, 2007.

[3] R. Piazza, T. Bellini, and V. Degiorgio. Equilibrium sedimentation prodiles of screened charged colloids: A test of the hard-sphere equation of state. *Physical Review Letters*, 71(25):4267-4270, 1993.

[4] D. Fennell Evans and H. Wennerström. *The Colloidal Doman.* Wiley-VCH, second edition, 1999.

[5] M. Takeo. *Disperse Systems.* Wiley-VCH, first edition, 1999.

[6] N. F. Carnahan and K. E. Starling. Equation of state for nonattracting rigid spheres. *Jounral of Chemical Physics*, 51(2):635–636, 1969.

[7] M. A. Rutgers, J. H. Dunsmuir, J.-Z. Xue, W. B. Russel, and P. M. Chaikin. Measurement of the hard-sphere equation of state using screened charged polystyrene colloids. *Physical Review B*, 53(9):5043–5046, 1996.

[8] M. D. Carbajal-Tinoco, R. Lopez-Fernandez, and J. L. Arauz-Lara. Asymmetry in colloisal dissusion near a rigid wall. *Physical Review Letters*, 99(138303):1–4, 2002.

[9] R. Tao, T. Woestman, and N. K. Jaggi. Electric field induced solidification. *Applied Physics Letters*, 55(18):1844 1846, 1989.

[10] J. E. Martin, J. Odinek, T. C. Halsey, and R. Kamien. Structure and dynamics of electrorheological fluids. *Physical Review E*, 57(1):756 775, 1998.

[11] A. Yethiraj and A. van Blaaderen. A colloidal model system with an interaction tunable from hard sphere to soft and dipolar. *Nature*, 421:513–517, 2003.

[12] A. K. Agarwal and A. Yethiraj. Low-density ordered phase in brownian dipolar colloidal suspensions. *Physical Review Letters*, 102(198301):1–4, 2009.

[13] A. Kumar, B. Khusid, Z. Qiu, and A. Acrivos. New electric-field-driven mesoscale phase transitions in polarized suspensions. *Physical Review Letters*, 95(258301):1–4, 2005.

[14] W. Poon. Colloids as big atoms. *Science*, 304(5672):830–831, 2004.

[15] N. Li, H. D. Newman, M. Valera, I. Saika-Voivod, and A. Yethiraj. Colloids with a tunable dipolar interaction: equations of state and order parameters via confocal microscopy. *Soft Matter*, 6(5):876–880, 2010.

[16] N. H. March and M. P. Tosi. *Introduction to Liquid State Physics*. World Scientific, first edition, 2002.

[17] T. C. Hales. A proof of the kepler conjecture. *Annals of Mathematics*, 162(3):1065–1185, 2005.

[18] W. G. Hoover and F. H. Ree. Melting transition and communal entropy for hard spheres. *Journal of Chemical Physics*, 49(8):3609, 1968.

[19] J.-B. Perrin. Mouvement brownien et réalité moléculaire. *Annales de chimie et de physique*, 8(15):5–114, 1909.

[20] A. Einstein. Über die von der molekularkinetischen theorie der wärme geforderte bewegung von in ruhenden flüssigkeiten suspendierten teilchen. *Annalen der Physik*, 17(8):549 560, 1905.

[21] W. B. Russel, D. A. Saville, and W. R. Schowalter. *Colloidal Dispersions*. Cambridge University Press, 2001.

[22] J. O'M. Bockris and A. K. N. Reddy. *Modern Electrochemistry 1: Ionics*. Kluwer Academic Publishers, second edition, 2002.

[23] T. Biben, J.-P. Hansen, and J.-L. Barrat. Density profiles of concentrated colloidal suspensions in sedimentation equilibrium. *Journal of Chemical Physics*, 98(9):7330 7344, 1993.

[24] S. Buzzaccaro, R. Rusconi, and R. Piazza. "sticky" hard spheres: Equation of state, phase diagram, and metastable gels. *Physical Review Letters*, 99(098301):1–4, 2007.

[25] N. Li. Colloidal ordering under external electric fields. M. Sc. Thesis, Memorial University of Newfoundland, March 2007.

[26] W. M. Winslow. Induced vibration of suspensions. *Journal of Aplied Physics*, 20:1137–1140, 1949.

[27] R. L. Price and W. G. Jerome. *Basic Confocal Microscopy*. Springer.

[28] L. Antl, J. W. Goodwin, R. D. Hill, R. H. Ottewill, S. M. Owens, S. Papworth, and J. A. Waters. The preparation of poly(methyl methacrylate) lattices in nonaqueous media. *Colloids and Surfaces*, 17(1):67–68, 1968.

[29] G. Bosma, C. Pathmamanoharan, E. H. A. de Hood, W. K. Kegel, A. van Blaaderen, and H. N. W. Lekkerkerker. Preparation of monodisperse, fluorescent pmma-latex colloids by dispersion polymerization. *Journal of Colloid and Interface Science*, 245(2):292–300, 2002.

[30] E. Weeks. `http://www.physics.emory.edu/ weeks/idl/`.

[31] J. C. Crocker and D. G. Grier. Methods of digital video microscopy for colloidal studies. *Journal of Colloid and Interface Science*, 179(0217):298 310, 1996.

[32] G. K. Batchelor. Sedimentation in a dilute dispersion of spheres. *Journal of Fluid Mechanics*, 52:245, 1972.

[33] M. Muthukumar and K.F. Freed. Cluster expansion for concentration dependence of cooperative friction coefficients for suspensions of interacting spheres. *Journal of Chemical Physics*, 78:511, 1983.

[34] R. E. Beckham and M. A. Bevan. Interfacial colloidal sedimentation equilibrium. i. intensity based confocal microscopy. *Journal of Chemical Physics*, 127(164708):1–13, 2007.

[35] R. Tao and J. M. Sun. Electric field induced solidification. *Physical Review A*, 44(10):6181–6184, 1991.

[36] A. Almudallal and I. Saika-Voivod. Simulation of a two-dimensional model for colloids in a uniaxial electric field. *Physical Review E*, 84(1):9, 2011.

[37] H. Newman III. Sedimentation profiles and dynamics of brownian colloidal suspensions. B.Sc. Honours Thesis, Memorial University of Newfoundland, December 2008.